

**ROOM-TEMPERATURE, CONTINUOUS-
WAVE QUANTUM CASCADE LASERS IN THE
FIRST AND SECOND ATMOSPHERIC
WINDOWS**

ZHIJUN LIU

**A DISSERTATION
PRESENTED TO THE FACULTY
OF PRINCETON UNIVERSITY
IN CANDIDACY FOR THE DEGREE
OF DOCTOR OF PHILOSOPHY**

**RECOMMENDED FOR ACCEPTANCE
BY THE DEPARTMENT OF ELECTRICAL
ENGINEERING**

ADVISOR: CLAIRE F GMACHL

JUNE 2008

© Copyright by Zhijun Liu, 2008. All rights reserved.

Abstract

Quantum Cascade (QC) lasers are mid-infrared semiconductor light sources which attract considerable interest for mid-infrared sensor systems, especially for high sensitivity and selectivity detection of chemical vapors in security, medical, and environmental applications. For some of these practical sensing applications, high temperature (room temperature and above), high power, continuous-wave (CW) operation is desirable for the purposes of simplifying the system and increasing the sensitivity. However, due to the thermal effects associated with the high threshold and low wall-plug efficiency, the performance of QC lasers is severely limited at high temperature. To overcome this problem, this dissertation shows how to optimize the QC laser performance through high gain active region and low loss waveguide designs, and advanced device processing and packaging for better thermal management.

First, a self-consistent thermal model of QC lasers has been developed, and combined with band-structure design and waveguide design to provide a comprehensive design tool which includes the consideration of thermal management. Using this model, room temperature, CW QC lasers at $\lambda \approx 8.2 \mu\text{m}$ have been designed, grown and demonstrated, which includes the first room temperature CW QC lasers grown by metal-organic chemical vapor deposition (MOCVD) without lateral regrowth. Next, by using similar design strategies, high performance, room temperature, CW operation has been extended to longer wavelengths of 9.6-10.3 μm within the second atmospheric window, which are useful for sensing important gases such as diisopropyl methylphosphonate (DIMP, an explosive stimulant), etc. Third, to better understand the laser performance and further improve the laser designs, a systematic study on temperature-dependent optical gain and

waveguide loss was conducted in those high performance QC lasers using Hakki-Paoli technique. Besides confirming the expected magnitude and temperature dependence of the gain coefficient, the results indicate a 2-3 times higher waveguide loss than the one calculated from free carrier absorption, which indicates the presence of other loss mechanisms inside the laser active core. Finally, using strain-compensated InGaAs/AlInAs material, a high performance, short wavelength $\lambda \approx 5.3 \mu\text{m}$ QC laser was demonstrated with very small heat dissipation of 1.2 - 1.7 W for room temperature, CW operation. These lasers may lead to the first uncooled, room temperature, CW laser packages.

Acknowledgements

I want to express my sincere thanks to my advisor Professor Claire F. Gmachl. Her guidance led me to a fascinating photonic world. Her deep insight of device physics pointed me to in-depth thinking behind observations. I want to thank her for her patience, kindness, encouragement and optimism during my nearly five years' Ph.D. study. Also her open-mind, cooperative working style enables me to gain a valuable team-working experience.

I would also like to thank Professors Craig B. Arnold and Gerard Wysocki for spending time to read this thesis and for their insightful comments and assistance.

I want to thank our collaborators, Ms. Deborah L. Sivco at Alcatel-Lucent, Mr. Liwei Chen and Prof. Fow-Sen Choa at University of Maryland Baltimore County, Dr. Rich Leavitt and Dr. Fred J. Towner at Maxion Technologies Inc., Dr. Xiaojun Wang and Dr. Jenyu Fan at Adtech Optics, Dr. Catherine G. Caneau and Dr. Chung-en Zah at Corning Inc.. Their wafer growth made it possible for this thesis work to be implemented.

Also here I wish to thank my group mates for their valuable assistance and discussion throughout the work. They are Prof. Dan Wasserman, Dr. Jian-Zhang Chen, Dr. Jian-xin Cheng, Dr. Anna Michel, Mr. Scott Howard, Ms. Afusat Dirisu, Mr. Anthony Hoffman, Mr. Kale Franz, Ms. Fatima Toor, Ms. Dongxia Qu, Ms. Yu Yao, Ms. Ekua Anane-Fenin, Mr. Matthew Escarra, Mr. Richard Cendejas and Mr. Qiang Liu.

Here I want to give my special thanks to my wife Ms. Yong Chang. She has been on my side sharing both my happy and hard times. Her limitless love, comfort and encouragement have been supporting me throughout my Ph. D study.

I wish to thank my parents and parents-in-law for their endless love, support, and encouragement. Also here, I want to thank my two elder sisters and their families, my sister-in-law and her family. Their unconditional care and love gave me warmth in this new country.

Table of Contents

Abstract	iii
Acknowledgements	v
Table of Contents	vii
List of Tables	ix
List of Figures	x
1 Introduction	1
1.1 Overview of Quantum Cascade Lasers	1
1.2 Operating Principle of Quantum Cascade Lasers	2
1.2.1 Active Region and Optical Gain	2
1.2.2 Waveguide and Loss	7
1.2.3 Laser Threshold	9
1.3 Thermal Effects in Quantum Cascade Lasers	10
1.4 State of the Art Quantum Cascade Lasers	12
1.5 Motivation and Organization of This Thesis	15
2 High Performance Quantum Cascade Lasers at $\lambda \approx 8.2 \mu\text{m}$	17
2.1 Introduction	17
2.2 Laser Design and Thermal Modeling	17
2.2.1 Active Region and Waveguide Designs	17
2.2.2 Thermal Modeling	25
2.3 Laser Fabrication	37
2.3.1 Ridge Waveguide Laser with Thin Metal Top Contact	37
2.3.2 Ridge Waveguide Laser with Thick Metal Top Contact	39
2.3.3 Buried Heterostructure Laser with Thick Metal Top Contact	41
2.4 Laser Characterization Setups	43
2.4.1 Spectrum Testing Setup	43
2.4.2 Light-current-voltage Testing Setups	43
2.5 Laser Testing	44
2.5.1 Ridge Waveguide Laser with Thin Metal Top Contact	46
2.5.2 Ridge Waveguide Laser with Thick Metal Top Contact	53
2.5.3 Buried Heterostructure Laser with Thick Metal Top Contact	57
2.6 Conclusion and Discussion	60
3 Long Wavelength High Performance $\lambda \approx 9.6 - 10.3 \mu\text{m}$ Quantum Cascade Lasers	63
3.1 Introduction	63
3.2 $\lambda \approx 9.6 \mu\text{m}$ “Vertical Transition” Quantum Cascade Lasers	65
3.2.1 Laser Design	65
3.2.2 Ridge Waveguide Laser with Thick Metal Top Contact	67
3.3 $\lambda \approx 10.3 \mu\text{m}$ “Vertical Transition” Quantum Cascade Lasers	68
3.3.1 Laser Design	68

3.3.2 Ridge Waveguide Laser with Thick Metal Top Contact	70
3.3.3 Buried Heterostructure Laser with Thick Metal Top Contact	74
3.4 $\lambda \approx 9.8 \mu\text{m}$ “Diagonal Transition” Quantum Cascade Lasers	76
3.4.1 Laser Design	76
3.4.2 Ridge Waveguide Laser with Thick Metal Top Contact	78
3.5 $\lambda \approx 10.1 \mu\text{m}$ “Diagonal transition” Quantum Cascade Lasers	81
3.5.1 Laser Design	81
3.5.2 Ridge Waveguide Laser with Thick Metal Top Contact	82
3.6 Conclusion and Discussion	84
4 Optical Gain and Loss Measurement in Quantum Cascade Lasers	88
4.1 Introduction	88
4.2 Methods	89
4.3 Optical Gain and Loss in “Vertical Transition” $\lambda \approx 8.2 \mu\text{m}$ QC Lasers	92
4.4 Optical Gain and Loss in “Vertical Transition” $\lambda \approx 9.6 \mu\text{m}$ QC Lasers	95
4.5 Optical Gain and Loss in “Vertical Transition” $\lambda \approx 10.3 \mu\text{m}$ QC Lasers	96
4.6 Optical Gain and Loss in “Diagonal Transition” $\lambda \approx 9.8 \mu\text{m}$ QC Lasers	101
4.7 Optical Gain and Loss in “Diagonal Transition” $\lambda \approx 10.1 \mu\text{m}$ QC lasers	104
4.8 Conclusion and Discussion	109
5 High Performance Quantum Cascade Lasers at $\lambda \approx 5.3 \mu\text{m}$	111
5.1 Introduction	111
5.2 Laser Design	112
5.3 Ridge Waveguide Laser with Thick Metal Top Contact	115
5.4 Very Small Heat Dissipation, Room Temperature, CW QC Laser	124
5.5 Conclusion and Discussion	126
6 Summary and Outlook	127
6.1 Summary of Current Work	127
6.2 Future Work	129
Bibliography	132
List of Publications	144

List of Tables

Table 2.1 Design parameters for three QC laser active regions at $\lambda \approx 8.2 \mu\text{m}$.

Table 2.2 QC laser samples at $\lambda \approx 8.2 \mu\text{m}$.

Table 2.3 Summary of experimental results for QC laser samples at $\lambda \approx 8.2 \mu\text{m}$.

Table 3.1 QC laser samples at $\lambda \approx 9.6\text{-}10.3 \mu\text{m}$.

Table 3.2 Summary of experimental results for QC laser samples at $\lambda \approx 9.6\text{-}10.3 \mu\text{m}$.

Table 4.1 QC laser samples studied in the optical gain and loss measurement.

Table 5.1 Summary of $\lambda \approx 5.3 \mu\text{m}$ QC lasers, relevant design parameters and experimental results.

List of Figures

Figure 1.1 Schematic timeline of major developments in QC lasers.

Figure 1.2 (a) Schematic of a deep-etched, ridge waveguide QC laser. The brown arrow indicates the laser emission. (b) A Transmission Electron Microscopy (TEM) image of the active core of a QC laser. The dark layers are the $\text{In}_{0.52}\text{Al}_{0.48}\text{As}$ barriers, and the bright layers are the $\text{In}_{0.53}\text{Ga}_{0.47}\text{As}$ wells. Length of one period in this example is ~ 55 nm. (c) Conduction band diagram of 1.5 periods of active regions and injectors of a QC laser and the moduli squared of relevant wavefunctions.

Figure 1.3 Schematic of the relevant electron states in the operation of QC lasers.

Figure 1.4 (a) Layer structure of a typical dielectric waveguide of a QC laser. (b) The corresponding intensity profile of the fundamental TM mode and profile of the real part of the refractive index.

Figure 1.5 Schematic illustration of thermal effects of electron thermal backfilling, thermionic emission, and injection leakage in QC lasers.

Figure 1.6 (a) Maximum CW operation temperature and (b) maximum CW power at room temperature of the high performing QC lasers reported in the literatures at the time of writing this thesis. These data are taken from Refs. [12, 13, 37-55].

Figure 2.1 Portion of the conduction band diagram and the moduli squared of the relevant wave functions of a $\lambda \approx 8 \mu\text{m}$ QC laser with a four quantum-well active region based on a two phonon resonance design. An electric field of 51 kV/cm is applied. The vertical arrow indicates the laser transition.

Figure 2.2 (a) Layer structure of a ternary cladding waveguide design for a $\lambda \approx 8 \mu\text{m}$ QC laser. (b) Intensity profile of the fundamental TM mode and profile of the real part of the refractive index of the dielectric waveguide.

Figure 2.3 Calculated pulsed threshold current density at 300 K for a 2 mm long QC laser as a function of the doping level in three waveguide layers, i.e. (a) injector region, (b) AlInAs top cladding layer, and (c) InGaAs plasmon layer in the waveguide structure shown in Figure 2.2.

Figure 2.4 (a) Layer structure of binary InP cladding waveguide design for a $\lambda \approx 8 \mu\text{m}$ QC laser. (b) Intensity profile of the fundamental TM mode and profile of the real part of the refractive index of the dielectric waveguide.

Figure 2.5 Schematic work-flow of the self-consistent method for the thermal modeling of QC lasers.

Figure 2.6 Experimental thermal conductivity of InP at different temperatures (after Ref. [57]).

Figure 2.7 Experimental thermal conductivity of $\text{In}_{0.53}\text{Ga}_{0.47}\text{As}$ at different temperatures (after Refs. [57] and [58])

Figure 2.8 Thermal conductivity of laser active core extracted from experimental data on QC lasers reported in Ref. [13].

Figure 2.9 Temperature distribution (a), and laser core temperatures T_{core} and T'_{core} (b) at different iterations of core temperature for an epitaxial-side-up mounted, ternary waveguide cladding, 2 mm long, 10 μm wide, back facet high reflectivity (HR) coated, ridge waveguide laser with thin metal top contact at $\lambda \approx 8 \mu\text{m}$.

Figure 2.10 Temperature distribution (a), and laser core temperatures T_{core} and T'_{core} (b) at different iterations of core temperature for an epitaxial-side-up mounted, ternary waveguide cladding, 2 mm long, 10 μm wide, back facet high reflectivity (HR) coated, ridge waveguide laser with thick metal top contact at $\lambda \approx 8 \mu\text{m}$.

Figure 2.11 Temperature distribution for an epitaxial-side-down mounted, ternary waveguide cladding, 2 mm long, 10 μm wide, back facet high reflectivity (HR) coated, ridge waveguide laser with thick metal top contact at $\lambda \approx 8 \mu\text{m}$.

Figure 2.12 Threshold current density (a), threshold voltage (b), heat dissipation power (c), and core temperature (d) as a function of Δ , the energy difference between the lower laser level of one active region and the ground state of the next down steam injector.

Figure 2.13 Temperature distribution of an epitaxial-side-up mounted, InP waveguide cladding, 2 mm long, 10 μm wide, back facet high reflectivity (HR) coated, ridge waveguide laser with thick metal top contact at $\lambda \approx 8 \mu\text{m}$.

Figure 2.14 Temperature distribution of an epitaxial-side-down mounted, InP waveguide cladding, 2 mm long, 10 μm wide, back facet high reflectivity (HR) coated, ridge waveguide laser with thick metal top contact at $\lambda \approx 8 \mu\text{m}$.

Figure 2.15 Temperature distribution of an epitaxial-side-up mounted, InP waveguide cladding, 2 mm long, 10 μm wide, back facet high reflectivity (HR) coated, buried heterostructure (BH) laser with thick metal top contact at $\lambda \approx 8 \mu\text{m}$.

Figure 2.16 Temperature distribution of an epitaxial-side-down mounted, InP waveguide cladding, 2 mm long, 10 μm wide, back facet high reflectivity (HR) coated, buried heterostructure (BH) laser with thick metal top contact at $\lambda \approx 8 \mu\text{m}$.

Figure 2.17 Processing steps of a ridge waveguide QC laser with thin metal top contact.

Figure 2.18 (a) Scanning Electron Microscope (SEM) image of a typical ridge waveguide QC laser with thin metal top contact; (b) Optical image of an epitaxial-side-up mounted ridge waveguide laser bar with thin metal top contact.

Figure 2.19 Processing steps of a ridge waveguide QC laser with thick metal top contact.

Figure 2.20 (a) Scanning Electron Microscope (SEM) image of a typical ridge waveguide QC laser with thick metal top contact; (b) Optical image of an epitaxial-side-up mounted, ridge waveguide QC laser with thick metal top contact.

Figure 2.21 Processing steps of a buried heterostructure QC laser with thick metal top contact.

Figure 2.22 (a) Optical image of the facet of a buried heterostructure QC laser with thick metal top contact; (b) Optical image of an epitaxial-side-up mounted buried heterostructure QC laser with thick metal top contact.

Figure 2.23 Schematic drawing of QC laser spectrum measurement setup.

Figure 2.24 Schematic drawing of L-I-V testing setups for QC lasers in pulsed mode (a) and CW (b).

Figure 2.25 (a) Emission spectrum of a 2.59 mm long, 18 μm wide, epitaxial-side-up mounted QC laser of wafer M354 operated in pulsed mode at 80 K and 0.48 A. (b) L-I-V curves of the device at different heat sink temperatures in pulsed mode.

Figure 2.26 Emission spectrum of a 2.59 mm long, 18 μm wide, epitaxial-side-up mounted QC laser of wafer M354 operated in CW mode at 80 K and 0.56 A.

Figure 2.27 Threshold current density versus heat sink temperature of a 2.59 mm long, 18 μm wide, epitaxial-side-up mounted QC laser from wafer M354 in both pulsed mode and CW. Exponential fits result in a characteristic temperature T_0 of 179 and 102 K for pulsed mode and CW, respectively.

Figure 2.28 Emission spectra of a 2.56 mm long, 12 μm wide, epitaxial-side-up mounted QC laser of wafer D3103 operated in pulsed mode above threshold at 80 and 300 K.

Figure 2.29 Threshold current density versus heat sink temperature of a 2.56 mm long, 12 μm wide, epitaxial-side-up mounted QC laser of wafer D3103 in both pulsed mode and CW. For comparison, the data of a 2.59 mm long, 18 μm wide, epitaxial-side-up mounted QC laser of wafer M354 is also given. Exponential fits result in a characteristic temperature T_0 of 172 and 108 K in pulsed mode and CW for D3103, and 179 and 102 K in pulsed mode and CW for M354, respectively.

Figure 2.30 Threshold current density versus heat sink temperature of a 3.1 mm long, 14 μm wide, epitaxial-side-up mounted QC laser of InP cladding wafer A887a and a 2.56

mm long, 12 μm wide, epitaxial-side-up mounted QC laser of AlInAs cladding wafer D3103 in both pulsed mode and CW. Exponential fits result in characteristic temperature T_0 of 159 and 69 K in pulsed mode and CW for A887a, and 164 and 83 K in pulsed mode and CW for D3103, respectively.

Figure 2.31 CW L-I-V curves for a 3.1 mm long, 14 μm wide, epitaxial-side-up mounted, ridge waveguide QC laser with thin metal top contact from wafer A887a.

Figure 2.32 Emission spectrum of a 3.1 mm long, 14 μm wide, epitaxial-side-up mounted, ridge waveguide QC laser with thin metal top contact from wafer A887a in CW mode at 80 K and 0.23 A.

Figure 2.33 (a) CW light-current curves of a HR coated 8 μm wide, 3.5 mm long, epitaxial-side-up mounted, QC laser (A887a) with thick metal top contact at different heat sink temperatures. The voltage-current curve at 300K is also given. The inset shows the laser spectrum at 300 K and 0.74 A. (b) Threshold current density as a function of the heat sink temperature in pulsed and CW operation (data points). The solid lines are the results of exponential fits $J_{\text{th}}=J_0 \exp(T/T_0)$. From 240 to 380 K, $T_0=217$ K for pulsed operation, and from 240 to 315 K, $T_0=107$ K for CW operation.

Figure 2.34 (a) CW light-current curves of a HR coated 6.5 μm wide, 3mm long, epitaxial-side-up mounted, QC laser (D3109) with thick metal top contact at different heat sink temperatures. The voltage-current curve at 280 K is also given. The inset shows the laser spectrum at 280 K and 0.69 A. (b) Threshold current density as a function of the heat sink temperature in pulsed and CW operation (data points). The solid lines are the results of exponential fits $J_{\text{th}}=J_0 \exp(T/T_0)$. From 160 to 390 K, $T_0=200$ K for pulsed operation, and from 160 to 280 K, $T_0=145$ K for CW operation.

Figure 2.35 SEM image of a facet of a buried heterostructure QC laser at $\lambda \approx 8 \mu\text{m}$ from wafer 111605_3. Voids are created on the two sides of the laser ridge due to a non-optimized lateral InP regrowth condition, where the laser ridge is aligned along [011] direction.

Figure 2.36 (a) CW light-current curves of a HR coated 8 μm wide, 3.5mm long buried heterostructure QC laser (111605_3) with thick metal top contact at different heat sink temperatures. The voltage-current curve at 300 K is also given. The inset shows the laser spectrum at 300 K and 0.65 A. (b) Threshold current density as a function of the heat sink temperature in pulsed and CW operation (data points). The solid lines are the results of exponential fits $J_{\text{th}}=J_0 \exp(T/T_0)$. From 240 to 400 K, $T_0=185$ K for pulsed operation, and from 240 to 330 K, $T_0=115$ K for CW operation.

Figure 3.1 Infrared absorption spectrum of DIMP and wavelengths of QC lasers developed in this work. The DIMP absorption spectrum is from Ref. [68].

Figure 3.2 Portion of the conduction band diagram and the moduli squared of the relevant wave functions of a 9.6 μm QC laser (“vertical transition” design) with a four quantum-

well active region based on a two phonon resonance. An electric field of 42 kV/cm is applied. The vertical arrow indicates the laser transition.

Figure 3.3 Intensity profile of the fundamental TM mode and profile of the real part of the refractive index of the dielectric waveguide calculated at 9.6 μm .

Figure 3.4 CW L-I-V curves of an HR coated, 17 μm wide, 3.5 mm long, ridge waveguide QC laser (M532) with thick metal top contact at different heat sink temperatures. The inset shows the laser spectrum at 240 K and 1.38 A.

Figure 3.5 Portion of the conduction band diagram and the moduli squared of the relevant wave functions of a 10.3 μm QC laser (“vertical transition” design) with a four quantum-well active region based on a two phonon resonance. An electric field of 37 kV/cm is applied. The arrow indicates the laser transition.

Figure 3.6 Intensity profile of the fundamental TM mode and profile of the real part of the refractive index of the dielectric waveguide calculated at $\lambda \approx 10.3 \mu\text{m}$.

Figure 3.7 Pulsed spectra of a Fabry-Perot, 3.5 mm long, 17.7 μm wide, epitaxial-side-up mounted, ridge waveguide QC laser with thick metal top contact at $\lambda \approx 10.3 \mu\text{m}$ (M475).

Figure 3.8 Pulsed L-I-V curves of a Fabry-Perot, 3.5 mm long, 17.7 μm wide, ridge waveguide QC laser with thick metal top contact (M475) at different heat sink temperatures.

Figure 3.9 CW spectra of a Fabry-Perot, 3.5 mm long, 17.7 μm wide, epitaxial-side-up mounted, ridge waveguide QC laser with thick metal top contact at $\lambda \approx 10.3 \mu\text{m}$ (M475).

Figure 3.10 CW L-I-V curves of a Fabry-Perot, 3.5 mm long, 17.7 μm wide, ridge waveguide QC laser with thick metal top contact (M475) at different heat sink temperatures.

Figure 3.11 Threshold current density versus heat sink temperature for a Fabry-Perot, 3.5 mm long, 17.7 μm wide, ridge waveguide QC laser with thick metal top contact (M475) in pulsed and CW operation (data points). The solid lines are the results of exponential fits $J_{\text{th}}=J_0 \exp(T/T_0)$. From 80 K to 320 K, $T_0=167$ K for pulsed operation, and from 80 K to 268 K, $T_0=114$ K for CW operation.

Figure 3.12 Threshold current density as a function of the heat sink temperature in pulsed and CW operation for three 3.5mm long lasers (M475) with different ridge width of 18, 15.6, 12.2 μm . The dotted lines are the results of exponential fits $J_{\text{th}}=J_0 \exp(T/T_0)$.

Figure 3.13 Calculated waveguide loss resulting from free carrier absorption versus laser ridge width for double-trench ridge waveguide QC lasers with thick metal top contact at $\lambda \approx 10.3 \mu\text{m}$ (M475).

Figure 3.14 Pulsed and CW threshold current densities versus heat sink temperature of a 3.5 mm long, 15.6 μm wide, ridge waveguide QC laser with thick metal top contact at $\lambda \approx 10.3 \mu\text{m}$, and of a 3.5 mm long, 15.4 μm wide, buried heterostructure QC laser from the same wafer (M475) before and after HR coating on its back facet.

Figure 3.15 CW L-I-V curves at different heat sink temperatures for a back facet HR coated, 3.5 mm long, 15.4 μm wide, epitaxial-side-up mounted , buried heterostructure QC laser (M475). The inset shows the typical laser spectrum at room temperature.

Figure 3.16 Portion of the conduction band diagram and the moduli squared of the relevant wave functions of a $\lambda \approx 9.8 \mu\text{m}$ QC laser designed with a “diagonal transition” and a two phonon resonance scheme. An electric field of 47 kV/cm is applied. The arrow indicates the laser transition.

Figure 3.17 Intensity profile of the fundamental TM mode and profile of the real part of the refractive index of the dielectric waveguide calculated at $\lambda \approx 9.8 \mu\text{m}$.

Figure 3.18 CW L-I-V curves for a 3.5 mm long, 10 μm wide, “diagonal transition” QC laser at $\lambda \approx 9.8 \mu\text{m}$ (M474). The inset shows a laser spectrum at 80 K and 0.55 A.

Figure 3.19 Threshold current density versus heat sink temperature of a 3.5 mm long, 12.5 μm wide, “diagonal transition” QC laser of M474 and a 3.5 mm long, 12.2 μm wide, “vertical transition” QC laser of M475 in both pulsed mode and CW.

Figure 3.20 Pulsed threshold current density measured at 200 K heat sink temperature for three 3.5 mm long QC lasers of M474 with different ridge width of 18.5, 16.5, 12.5 μm . Dashed line is guide to eye.

Figure 3.21 A portion of the conduction band diagram and the moduli squared of the relevant wave functions of a $\lambda \approx 10.1 \mu\text{m}$ QC laser designed as diagonal transition with a two phonon resonance scheme. An electric field of 41 kV/cm is applied. The arrow indicates the laser transition.

Figure 3.22 Intensity profile of the fundamental TM mode and profile of the real part of the refractive index of the dielectric waveguide calculated at $\lambda \approx 10.1 \mu\text{m}$.

Figure 3.23 Spectrum of a 3.5 mm long, 16 μm wide, ridge waveguide QC laser with thick metal top contact (M490) in CW mode at 80K.

Figure 3.24 CW L-I-V curves for a 3.5 mm long, 16 μm wide, ridge waveguide QC laser with thick metal top contact at $\lambda \approx 10.1 \mu\text{m}$ (M490).

Figure 3.25 Threshold current density versus heat sink temperature of a 3.5 mm long, 16 μm wide, ridge waveguide QC laser with thick metal top contact (M490) in both pulsed and CW modes.

Figure 3.26 Measured and calculated threshold current density at 300 K for the best QC lasers at wavelengths of 8.2, 9.6-10.3 μm , which were presented in Chapters 2 and 3.

Figure 4.1 (a) Representative subthreshold amplified spontaneous emission spectrum of a 1.5 mm long, 16 μm wide, epitaxial-side-up mounted, ridge waveguide QC laser with thick metal top contact at $\lambda \approx 10.3 \mu\text{m}$ (M475). The laser is operated in CW mode at 0.33 A current and 120 K heat sink temperature. The inset shows the central Fabry-Perot modes in greater detail. (b) Peak net modal gain as a function of the injection current density, where the linear least squares fit (solid line) gives the gain coefficient and waveguide loss from its slope and y-axis intercept, respectively.

Figure 4.2 (a) Conduction band diagram of a portion of the active regions and injectors and the moduli squared of the relevant wave functions of sample M475 under a bias of 4 V, i.e. an electrical field of 18.6 kV/cm. The bold curve represents the upper laser level; (b) CW L-I-V curves of a 3.5 mm long, 17.7 μm wide QC laser at $\lambda \approx 10.3 \mu\text{m}$ (M475) at different heat sink temperatures.

Figure 4.3 Measured gain coefficient (solid squares) and waveguide loss (open squares) versus core temperature for a 1.5 mm long, 9 μm wide ridge waveguide QC laser at $\lambda \approx 8.2 \mu\text{m}$ (A887a). The dashed line is the theoretical gain coefficient, and the circles are the calculated waveguide loss from free carrier absorption. Lines through data points are guides to the eye without fit parameters.

Figure 4.4 Full width half maximum (FWHM) linewidth of the electroluminescence of the laser transition at different heat sink temperatures for representative samples studied in this section. Solid and dashed lines are second order polynomial fit to the data points. Data are obtained from semi-circle mesas in pulsed mode under injection currents close to the laser threshold.

Figure 4.5 Measured gain coefficient (solid squares) and waveguide loss (open squares) versus core temperature for a 1.5 mm long, 16 μm wide ridge waveguide QC laser at $\lambda \approx 9.6 \mu\text{m}$ (M532). The dashed line is the theoretical gain coefficient, and the circles are the waveguide loss calculated from free carrier absorption. Lines through data points are guides to the eye.

Figure 4.6 Measured gain coefficient and waveguide loss versus core temperature for a 1.5 mm long, 16 μm wide, ridge waveguide QC laser (squares) and a buried heterostructure QC laser (triangles) at $\lambda \approx 10.3 \mu\text{m}$ (M475). The dashed line is the theoretical gain coefficient, and the solid and open circles are calculated waveguide loss from free carrier absorption for the ridge waveguide and buried heterostructure lasers, respectively. Lines through data points are guides to the eye.

Figure 4.7 Silicon concentration in M475 from Secondary Ion Mass Spectrometry (SIMS) measurement. [Data by Evans Analytical Group]

Figure 4.8 Carrier concentration in sample M475 from Capacitance-Voltage measurement. [Data by Maxion Technologies]

Figure 4.9 (a) Conduction band diagram of a portion of the active regions and injectors and the moduli squared of the relevant wave functions of a $\lambda \approx 10.3 \mu\text{m}$ QC laser (M475) with a 4 quantum well active region. An electric field of 39 kV/cm is applied. The dotted arrow indicates the laser transition. The solid arrow represents a pathway of resonant absorption. (b) Calculated absorption coefficient of the intersubband resonant transition indicated by the solid arrow in (a) and the thermally excited electron density on the state above the upper laser level.

Figure 4.10 Measured gain coefficient (solid squares) and waveguide loss (open squares) versus core temperature for a 1.5 mm long, 12 μm wide ridge waveguide diagonal transition QC laser at $\lambda \approx 9.8 \mu\text{m}$ (M474). The dashed line is the theoretical gain coefficient, and the circles are the waveguide loss calculated from free carrier absorption. Lines through data points are guides to the eye.

Figure 4.11 Conduction band diagram of a portion of the active regions and injectors and the moduli squared of the relevant wave functions of a $\lambda \approx 9.8 \mu\text{m}$ diagonal transition QC lasers (M474). An electric field of 45 kV/cm is applied. The dotted arrow indicates the laser transition. The downwards pointing solid arrows represent parasitic optical transitions, and the upwards pointing solid arrow indicates a pathway of resonant absorption.

Figure 4.12 Calculated absorption coefficient of an intersubband resonant transition from the injector ground state to a higher lying level for sample M474.

Figure 4.13 Measured electroluminescence of a 200 μm diameter, semi-circle mesa from $\lambda \approx 9.8 \mu\text{m}$ diagonal transition QC laser sample (M474) under pulsed operation at a current close to the laser threshold.

Figure 4.14 Measured gain coefficient (solid squares) and waveguide loss (open squares) versus core temperature for a 1.5 mm long, 15 μm wide ridge waveguide diagonal transition QC laser at $\lambda \approx 10.1 \mu\text{m}$ (M490). The dashed line is the theoretical gain coefficient. The circles show the calculated waveguide losses from free carrier absorption using the measured doping levels. Lines through data points are guides to the eye.

Figure 4.15 Calculated absorption coefficient of an intersubband resonant transition from the injector ground state to a higher lying level for sample M490, which is similar to the resonant absorption indicated by the upwards pointing solid arrow in Figure 4.11.

Figure 4.16 Measured room temperature electroluminescence of a 200 μm diameter, semi-circle mesa in pulsed mode at a current close to the laser threshold for (a) $\lambda \approx 9.6 \mu\text{m}$ vertical transition QC laser sample (M532) and (b) $\lambda \approx 10.1 \mu\text{m}$ diagonal transition QC laser sample (M490).

Figure 5.1 Calculated conduction band offset as a function of InAs mole fraction of the $\text{In}_x\text{Ga}_{1-x}\text{As}$ layer for an $\text{In}_x\text{Ga}_{1-x}\text{As}/\text{In}_y\text{Al}_{1-y}\text{As}$ strain-compensated bilayer grown on an InP substrate. The dotted line represents the lattice-matched composition, and the dashed line indicates the composition used in $\lambda \approx 5.3 \mu\text{m}$ QC laser design.

Figure 5.2 Conduction band diagram of a portion of the active regions and injectors and moduli squared of the relevant wave functions of a $\lambda \approx 5.3 \mu\text{m}$ QC laser with a 4 quantum well active region. An electric field of 63 kV/cm is applied. The red arrow indicates the laser transition.

Figure 5.3 Intensity profile of the fundamental TM mode and profile of the real part of the refractive index of the dielectric waveguide calculated at $\lambda \approx 5.3 \mu\text{m}$.

Figure 5.4 Pulsed L-I-V curves of a back facet HR coated, 3.5 mm long, 9.7 μm wide, ridge waveguide QC laser (E107253-1) with thick metal top contact at various heat sink temperatures.

Figure 5.5 (a) CW L-I-V curves of a back facet HR coated, 3.5 mm long, 9.7 μm wide, ridge waveguide QC laser (E107253-1) with thick metal top contact at various heat sink temperatures. (b) A typical Fabry-Perot laser spectrum at 1.2 A and 283 K heat sink temperature.

Figure 5.6 Threshold current density of a back facet HR coated, 3.5 mm long, 9.7 μm wide, ridge waveguide QC laser (E107253-1) with thick metal top contact in both pulsed and CW operations. The characteristic temperatures are 114 and 79 K for pulsed mode and CW, respectively.

Figure 5.7 Pulsed threshold current density at 296 K versus reciprocal cavity length for QC lasers from wafer E107253-1. A waveguide loss of 9.14 cm^{-1} and gain coefficient of 7.08 cm/kA are extracted from this measurement.

Figure 5.8 (a) CW L-I-V curves of a back facet HR coated, 3.5 mm long, 8.4 μm wide ridge waveguide QC laser (E107268B) with thick metal top contact at various heat sink temperatures. (b) A typical laser spectrum at 1.04 A and 300 K heat sink temperature.

Figure 5.9 Threshold current density versus heat sink temperature of a back facet HR coated, 3.5 mm long, 8.4 μm wide ridge waveguide QC laser (E107268B) with thick metal top contact in both pulsed and CW operations. The data of first wafer E107253-1 (see Figure 5.6) are also given for comparison. The lower doped wafer(E107268B) has ~5% lower threshold in pulsed mode at 300 K.

Figure 5.10 (a) CW L-I-V curves of a back facet HR coated, 3.5 mm long, 7.6 μm wide, ridge waveguide QC laser (E107276F) with thick metal top contact at various heat sink temperatures. (b) A typical laser spectrum at 0.55A and 300 K heat sink temperature.

Figure 5.11 Threshold current density versus temperature of a back facet HR coated, 3.5 mm long, 7.6 μm wide ridge waveguide QC laser (E107276F) with thick metal top contact in both pulsed and CW operations. The data for wafers E107253-1 and E107268B are also given for comparison. The lowest doped wafer E107276F has 16% and 20% lower threshold in pulsed mode at 300 K, compared to higher doped wafers E107268B and E107253-1, respectively.

Figure 5.12 Pulsed threshold current density at 296 K versus reciprocal cavity length for QC lasers from wafer E107276F.

Figure 5.13 Optical images for a 0.5 mm long, epitaxial-side-up mounted QC laser (E107276F) with both facets HR coated. For comparison, a conventional 3.5 mm long, epitaxial-side-up mounted QC laser with back facet HR coated is also given.

Figure 5.14 (a) Pulsed L-I-V curves for a 0.5 mm long, 9.35 μm wide QC laser (E107276F) with the back facet (dashed line) and both facets (solid line) HR coated at 295 K. (b) CW light-current curves of the laser with both facets HR coated at various heat sink temperatures. The voltage-current curve at 295 K is also given. The inset shows the laser spectrum at 295 K and 0.108 A.

Chapter 1

Introduction

1.1 Overview of Quantum Cascade Lasers

Quantum Cascade (QC) lasers are semiconductor injection lasers with emission wavelengths in the mid-infrared and far-infrared based on intersubband electron transitions. The original concept of QC lasers was proposed as early as 1971 by Kazarinov and Suris in a seminal paper [1], where light amplification by “photon-assisted” tunneling in quantum well superlattice was described. However, for the QC lasers to be realized in experiment, major advances were needed in the understanding of material properties, laser design and crystal synthesis. With breakthroughs in electron band structure engineering [2] and high quality heterostructure growth by molecular beam epitaxy (MBE) [3], QC lasers were first demonstrated at $\lambda \approx 4.3 \text{ } \mu\text{m}$ by J. Faist et al. in 1994 at Bell Labs using $\text{In}_{0.53}\text{Ga}_{0.47}\text{As}/\text{In}_{0.52}\text{Al}_{0.48}\text{As}$ alloys lattice matched to InP substrate [4], and since then significant and rapid developments have been achieved for QC lasers regarding to their performance and functionality. Figure 1.1 shows a timeline of major achievements in the development of QC lasers, which includes distributed feedback (DFB) QC lasers [5], “bow-tie” QC lasers [6], broad-band QC lasers [7], terahertz QC lasers [8,9], nonlinear QC lasers [10,11], high power room-temperature continuous-wave (CW) QC lasers [12,13], QC lasers grown by metal organic chemical vapor deposition (MOCVD) [14], QC lasers based on GaAs/AlGaAs material system [15], and very recently InAs/AlSb-based QC lasers for shorter wavelength generation [16], among of others.

Additionally, because of their designable wavelengths in the mid- and far-infrared spectral range as well as excellent laser properties including high optical power, wide wavelength tunability with external gratings, fast modulation capability, compactness and high reliability, QC lasers have become an increasingly important mid-infrared light sources, and have found important applications such as trace gas sensing, free-space telecommunications, remote sensing, and infrared countermeasures, etc. [17-21].

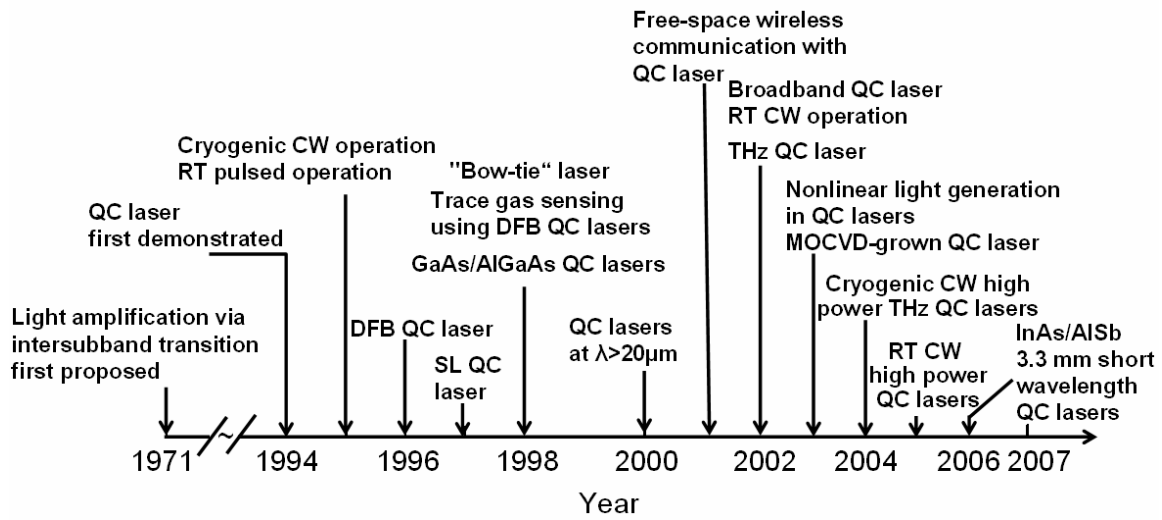


Figure 1.1 Schematic timeline of major developments in QC lasers.

1.2 Operating Principle of Quantum Cascade Lasers

1.2.1 Active Region and Optical Gain

QC lasers are unipolar semiconductor lasers based on electronic intersubband transitions in the conduction band of a coupled quantum well heterostructure. The optical gain in QC lasers is achieved via electron transport through scattering and tunneling between intersubband energy levels. Figure 1.2 (a) shows the cartoon picture of a typical QC laser. The laser is a deep-etched, ridge waveguide structure, and laser emission is from the as-cleaved facet. Figure 1.2 (b) is a Transmission Electron Microscope (TEM)

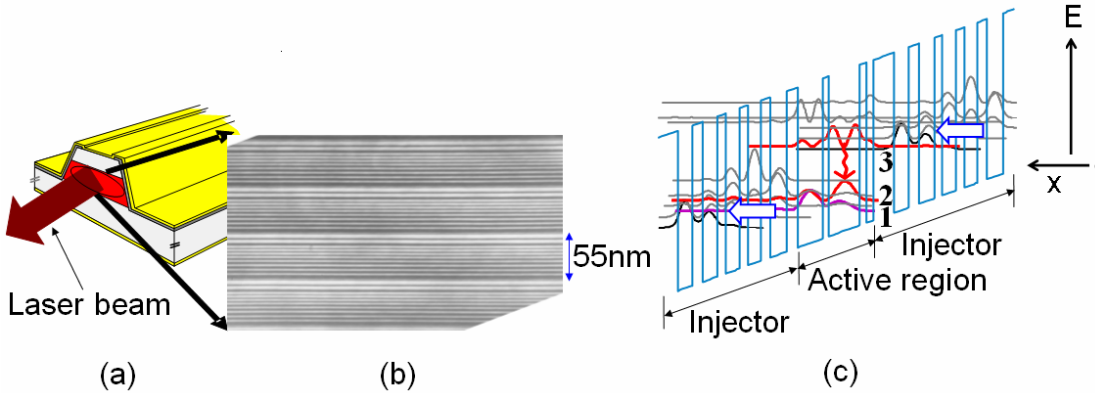


Figure 1.2 (a) Schematic of a deep-etched, ridge waveguide QC laser. The brown arrow indicates the laser emission. (b) A Transmission Electron Microscopy (TEM) image of the active core of a QC laser. The dark layers are the $\text{In}_{0.52}\text{Al}_{0.48}\text{As}$ barriers, and the bright layers are the $\text{In}_{0.53}\text{Ga}_{0.47}\text{As}$ wells. Length of one period in this example is ~ 55 nm. (c) Conduction band diagram of 1.5 periods of active regions and injectors of a QC laser and the moduli squared of relevant wavefunctions.

image showing the microscopic structure of the laser active core, which is composed of typically several tens of periods with totally ~ 500 alternating $\text{In}_{0.52}\text{Al}_{0.48}\text{As}$ barriers (dark regions) and $\text{In}_{0.53}\text{Ga}_{0.47}\text{As}$ wells (bright regions). By solving Schrödinger's equation for the potential of the heterostructure superlattice, the electron energy conduction band diagram is calculated as shown in Figure 1.2 (c) under an applied bias according to the laser operation. The “active region” refers to where the laser transition occurs. The “injector” refers to the electron transition region between active regions, and part of it is doped with Si atoms to form an electron reservoir and supplies electrons to the laser states. The laser transition occurs between levels 3 and 2 in the active region. The population inversion is achieved by both injecting electrons into the upper laser level 3 through tunneling and fast electron depopulation from the lower laser level 2 into level 1 through resonant optical phonon emission as levels 2 and 1 are designed to be spaced by

approximated an energy of longitudinal optical (LO) phonon energy (~ 34 meV). The extrinsic electrons are supplied through Si dopants in the injector regions, which are set away from the laser transition energy levels so as to avoid impurity scattering effects.

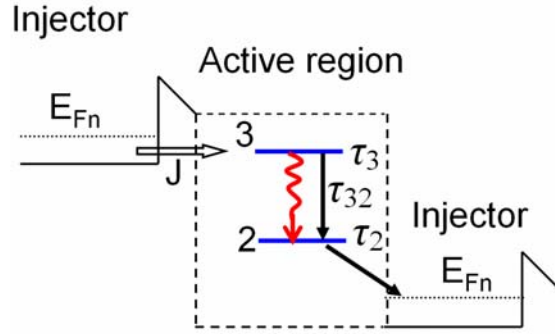


Figure 1.3 Schematic of the relevant electron states in the operation of QC lasers.

The optical gain in QC lasers can be described using a conventional rate equation model. A schematic drawing of the electron states relevant to the laser transition in QC lasers is shown in Figure 1.3, where states 3 and 2 represent the upper and lower laser levels, respectively. The rates equations for these electron energy levels are:

$$\frac{dn_3}{dt} = \frac{J}{e} - \frac{n_3}{\tau_3} - Sg_c(n_3 - n_2) \quad (1.1)$$

$$\frac{dn_2}{dt} = \frac{n_3}{\tau_{32}} + Sg_c(n_3 - n_2) - \frac{n_2}{\tau_2} \quad (1.2)$$

$$\frac{dS}{dt} = \frac{c}{n} [g_c(n_3 - n_2)S - \alpha S] \quad (1.3)$$

where n_3 and n_2 are the number of electrons occupying states 3 and 2, J is the pumping current, e is the electron charge, τ_3 and τ_2 are the lifetimes of states 3 and 2, τ_{32} is the non-radiative relaxation time from state 3 to state 2, S is the photon flux density, α is the total optical loss, n is the refractive index of the medium, c is the light velocity in vacuum, and

g_c is the peak gain cross section. Based on Fermi's golden rule and using a Lorentzian lineshape, the peak gain cross section takes the form of [22]

$$g_c = \frac{4\pi e^2 z_{32}^2}{\lambda_0 \epsilon_0 n L_p} \frac{1}{2\gamma_{32}} \quad (1.4)$$

where z_{32} is the dipole matrix element, λ_0 is the photon wavelength in vacuum, ϵ_0 is the vacuum electric permeability, L_p is the length of one period of active region and injector, $2\gamma_{32}$ is the full width at half maximum (FWHM) of the laser transition.

For steady state below laser threshold, the derivatives and S in Equations 1.1-1.3 are set to be zero, and the population inversion is obtained as

$$\Delta n = n_3 - n_2 = \frac{J\tau_3}{e} \left(1 - \frac{\tau_2}{\tau_{32}} \right) \quad (1.5)$$

The peak gain can be written as

$$G = g_c \Delta n = J\tau_3 \left(1 - \frac{\tau_2}{\tau_{32}} \right) \frac{4\pi e z_{32}^2}{\lambda_0 \epsilon_0 n L_p} \frac{1}{2\gamma_{32}} \quad (1.6)$$

Including the optical mode confinement factor Γ , defined as the fraction of the optical mode confined in the laser active core, the modal peak gain is given by

$$G_M = G\Gamma = J\tau_3 \left(1 - \frac{\tau_2}{\tau_{32}} \right) \frac{4\pi e z_{32}^2 \Gamma}{\lambda_0 \epsilon_0 n L_p (2\gamma_{32})} \quad (1.7)$$

The modal gain coefficient by the definition of $G_M = Jg_M$ is then expressed as

$$g_M = \tau_3 \left(1 - \frac{\tau_2}{\tau_{32}} \right) \frac{4\pi e z_{32}^2 \Gamma}{\lambda_0 \epsilon_0 n L_p (2\gamma_{32})} \quad (1.8)$$

In above gain coefficient expression, the lifetimes of laser levels τ_3 and τ_2 are mainly determined by nonradiative LO phonon scattering [23]. By special choices of the well and barrier thicknesses, the lifetime of upper laser level τ_3 can be designed to be much

larger than that of lower laser level τ_2 , through which the population reversion is achieved. In addition, the dipole matrix element z_{32} can be maximized by designing the wavefunctions of the upper and lower laser states. We numerically solve the Schrödinger's equation based on the one-band envelope function approximation to obtain the electron energy levels in the heterostructure. With the information of electron energy levels, the optical dipole matrix element z_{32} and LO phonon scattering lifetime τ_i are calculated to design the active region of QC lasers.

The active region design exemplified in Figure 1.2 (c) is a so-called “three well” vertical transition design [24], where the two lasing states 3 and 2 overlap in space, and carrier depopulation is implemented through a resonant LO phonon scattering into level 1. With better understanding of electron transport and the aim to achieve higher gain, more advanced designs were invented. The superlattice design is an example where the laser transition occurs between two extended states of the superlattice minibands [25]. In addition, if the laser transition is from a localized upper state to a lower extended superlattice state, the design is named “bound-to-continuum” design [26]. If two consecutive phonon resonant scatterings are used for electron depopulation from lower laser level, then the design is referred as “two-phonon-resonance” design [27]. Since the two-phonon-resonance design consists of four quantum wells, sometimes it is also termed as “four well” vertical transition design in this thesis. Moreover, besides the “vertical” laser transition, the laser transition can be designed as “diagonal” transition [28], where the wavefunctions of upper and lower laser levels are separated in space.

1.2.2 Waveguide and Loss

The laser emission requires that the optical mode is overlapping with the gain medium so that the gain overcomes the loss. For QC lasers, the loss is generally considered to originate from two major sources [29]. The first one is mirror loss. Typically the QC laser resonator is formed by two parallel, as-cleaved semiconductor facets with a reflectivity R of

$$R = ((n - 1)/(n + 1))^2 \quad (1.9)$$

This results in a mirror loss α_M of

$$\alpha_M = (1/L) \cdot (\ln R) \quad (1.10)$$

where L is the laser cavity length.

The second source of loss is non-resonant free carrier absorption in the waveguide denoted as α_W , which can be typically calculated from a Drude model with the dielectric constant given by [30]

$$\varepsilon = \varepsilon_\infty - \omega_p^2 / (\omega^2 + i\omega/(2\pi c\tau)) \quad (1.11)$$

where ε_∞ is the high frequency dielectric constant, ω is the frequency, and τ is the electron scattering lifetime, which we assume to be 0.1 ps in typical waveguide designs. ω_p is the plasmon frequency given by

$$\omega_p = \frac{1}{2\pi c} \left(\frac{4\pi Ne^2}{m^* \varepsilon_\infty} \right)^{1/2} \quad (1.12)$$

where N is the free electron density, m^* is the effective mass of the electrons.

Using Equations 1.11 and 1.12, the refractive index for each waveguide layer can be calculated, and next we numerically solve the Maxwell's equation using the thin-film matrix method [31] to obtain the laser mode distributions, waveguide loss α_W ,

and confinement factor Γ . Because of the selection rule of optical transition in QC lasers, the optical field is transverse magnetic (TM) polarized. Therefore only TM modes are calculated.

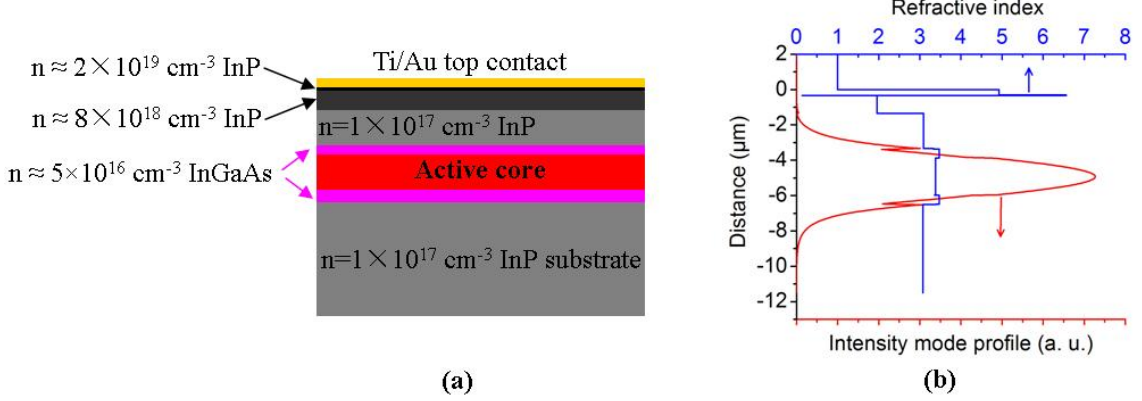


Figure 1.4 (a) Layer structure of a typical dielectric waveguide of a QC laser. (b) The corresponding intensity profile of the fundamental TM mode and profile of the real part of the refractive index.

The so-called “plasmon-enhanced” dielectric waveguide is widely used for QC lasers [32]. An example is shown in Figure 1.4. The laser active core is sandwiched between two low doped ($n \approx 5 \times 10^{16} \text{ cm}^{-3}$) $\text{In}_{0.53}\text{Ga}_{0.47}\text{As}$ layers. These two $\text{In}_{0.53}\text{Ga}_{0.47}\text{As}$ layers are used to pull the optical mode towards the laser active core so as to enhance the optical mode confinement. The bottom cladding is the low-doped InP substrate. The upper cladding layer consists of a low doped ($n \approx 1 \times 10^{17} \text{ cm}^{-3}$) InP, followed by a highly doped ($n \approx 8 \times 10^{18} \text{ cm}^{-3}$) InP plasmon layer, and a thin heavily doped ($n \approx 2 \times 10^{19} \text{ cm}^{-3}$) InP contact layer. The plasmon layer plays a crucial role in this waveguide structure, as it is highly doped such that it has a low refractive index, which helps to suppress the coupling of optical mode to the metal contact, thus resulting in a low waveguide loss. The refractive index profile and the corresponding intensity profile of the fundamental TM mode are

shown in Figure 1.4 (b). The waveguide loss α_w is calculated as 6.2 cm^{-1} , and the confinement factor Γ is 0.67.

Besides the above mentioned dielectric waveguide, researchers also designed surface-plasmon waveguides [33], where the optical mode is confined by surface plasmon at metal-semiconductor interface. This surface-plasmon waveguide design has the advantage of a high optical confinement, but suffers from a higher waveguide loss. It is useful especially for long wavelength QC lasers, where the dielectric waveguide suffers from unrealistic thick crystal growth.

1.2.3 Laser Threshold

The laser threshold is reached when the modal gain (Equation 1.7) equals to the total optical loss, i.e.,

$$J_{th}\tau_3\left(1 - \frac{\tau_2}{\tau_{32}}\right)\frac{4\pi e z_{32}^2 \Gamma}{\lambda_0 \epsilon_0 n L_p (2\gamma_{32})} = \alpha_M + \alpha_w \quad (1.13)$$

From Equation 1.13, the laser threshold current density is derived as

$$J_{th} = \frac{1}{\tau_3\left(1 - \frac{\tau_2}{\tau_{32}}\right)} \cdot \frac{\lambda_0 \epsilon_0 n L_p (2\gamma_{32})}{4\pi e z_{32}^2} \cdot \frac{\alpha_w + \alpha_M}{\Gamma} \quad (1.14)$$

The above equation gives the threshold current density at cryogenic temperatures. For high temperatures, thermal effects have to be taken into account, which are described in the next section.

1.3 Thermal Effects in Quantum Cascade Lasers

When the temperature increases, several effects take place. First, the electron LO phonon scattering lifetime decreases by the Bose factor through a larger phonon population at higher temperatures. This temperature-dependent LO phonon scattering lifetime is described by [34]

$$\tau_i(T) = \tau_{i0} \frac{1}{1 + \frac{2}{\exp\left(\frac{E_{LO}}{kT}\right) - 1}} \quad (1.15)$$

where τ_{i0} is the low temperature lifetime, E_{LO} is the energy of LO phonon, k is the Boltzmann constant, and T is the temperature. The reduction of LO phonon scattering lifetime at high temperature results in less gain as seen from the gain coefficient expression in Equation 1.8.

Second, the linewidth of the gain spectrum $2\gamma_{32}$ broadens at high temperatures, which again decreases the gain coefficient. In experiment, the gain spectrum linewidth usually increases by a factor of 2 when temperature increases from liquid nitrogen temperature to room temperature. This linewidth broadening is likely caused by the thermally enhanced electron scattering (roughness scattering, impurity scattering, etc.) and/or non-parabolicity effect. It is difficult to quantitatively describe these effects, and the temperature-dependent linewidth is usually measured from electroluminescence in experiment.

Third, with increasing temperature, electrons can be excited from an injector back to the lower laser level of the preceding active region, which is referred as “thermal backfilling” and indicated by the brown arrow in Figure 1.5. The thermal population on the lower laser level is given by [34]

$$n_2^{therm} = n_g \exp(-\Delta/kT) \quad (1.16)$$

where n_g is the doping sheet density of the injector, and Δ is the energy separation between the lower laser level and the quasi-Fermi level of the next down stream injector. For QC lasers, normally the injector is doped so that the quasi-Fermi level of the injector is slightly above the injector ground state. Therefore, in most cases, Δ can be taken as the energy separation between the lower laser level and the ground state of the next down stream injector. To suppress this thermal back filling effect, a large Δ needs to be designed.

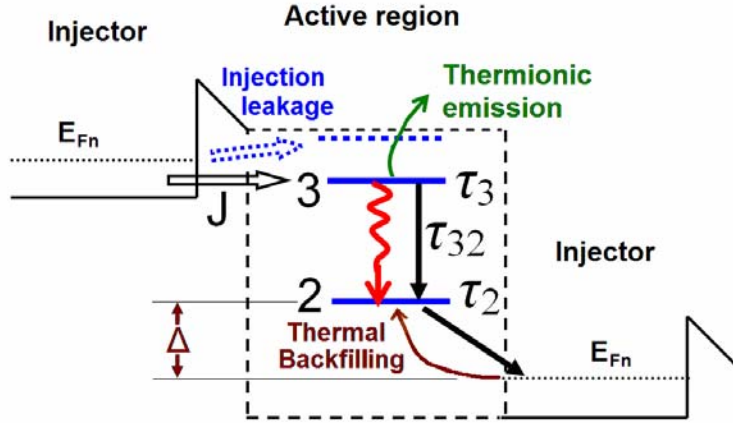


Figure 1.5 Schematic illustration of thermal effects of electron thermal backfilling, thermionic emission, and injection leakage in QC lasers.

Including the above three factors, i.e. temperature-dependent LO scattering lifetime, gain spectrum linewidth, and thermal backfilling into the rate equation model, a modified temperature-dependent threshold current density can be derived as [34]

$$J_{th} = \frac{1}{\tau_3(T) \left(1 - \frac{\tau_2(T)}{\tau_{32}(T)} \right)} \left[\frac{\varepsilon_0 n L_p \lambda_0 (2\gamma_{32}(T))}{4\pi e z_{32}^2} \cdot \frac{\alpha_w + \alpha_M}{\Gamma} + e n_2^{therm} \right] \quad (1.17)$$

where $\tau_i(T)$ and n_2^{therm} are given by Equations 1.15 and 1.16, and temperature-dependent linewidth $2\gamma_{32}$ is usually determined in experiment.

Aside from the above discussed three temperature effects, some other thermal effects can also happen such as electron injection leakage into other parasitic states (indicated by blue arrow in Figure 1.5), and thermionic emission (indicated by green arrow in Figure 1.5), i.e. electrons are thermally excited into the continuum. These effects reduce the carrier population on the upper laser state, thus resulting in less gain. We recently developed a comprehensive thermal model which includes thermionic emission [35].

Besides the usual description of temperature-dependent threshold current density as given by Equations 1.15-1.17, a simple empirical relation is often used to describe the threshold of a QC laser, i.e., [36]

$$J_{th} = J_0 \exp\left(\frac{T}{T_0}\right) \quad (1.18)$$

where T_0 is called the “characteristic temperature”, and this exponential relation fits well with the experimental data with typical T_0 values between 100 and 200 K.

1.4 State of the Art Quantum Cascade Lasers

Since their invention in 1994 [4], the performance of QC lasers has been increasing rapidly. As a milestone, the first room temperature, CW QC laser was realized at $\lambda \approx 9.1$ μm in 2002 by M. Beck et al. at University of Neuchâtel [12]. They used a high gain, two phonon resonance, vertical transition active region design, buried heterostructure processing and epitaxial-side-down mounting, and high reflectivity (HR) coating on both laser facets.

In 2003, J. S. Yu et al. at Northwestern University demonstrated a high power (106 mW), room temperature, CW QC laser at a shorter wavelength of $\lambda \approx 6 \mu\text{m}$ [13]. This high performance was achieved using a double-trench, ridge waveguide processing with a thick electroplated top gold contact and epitaxial-side-up mounting, which avoids the complex wafer regrowth. Using the similar design and technology, the Northwestern University group developed high power (> 100 mW), room temperature, CW QC lasers at other wavelengths of 3.8, 4, 4.3, 4.8, 5.25, 7.8, 9.5, and 10.6 μm , respectively [37-44].

Aside from high performance QC lasers with active core grown by MBE, breakthroughs were also achieved for high performance QC lasers grown by MOCVD, which is an industry-preferred growth technique [14]. In 2005, M. Troccoli et al. at Harvard University demonstrated a first MOCVD-grown room temperature, CW QC laser at $\lambda \approx 7.25 \mu\text{m}$ using a simple three-well design and buried heterostructure with a narrow laser ridge [45], and later on, using similar packaging technique but a two-phonon-resonance design they demonstrated MOCVD-grown high-power, room temperature, CW QC lasers at $\lambda \approx 5.3, 8.4, 9.5 \mu\text{m}$ [46-48], which are comparable to the best MBE-grown QC lasers. In early 2006, we demonstrated an MOCVD-grown room temperature, CW QC laser at $\lambda \approx 8.2 \mu\text{m}$ without the lateral regrowth using a two-phonon-resonance active region design and straightforward double-trench ridge waveguide processing [49]. Using the same active region design, but a modified waveguide design, O. Malis et al. at Bell labs, Lucent Technologies demonstrated a $\lambda \approx 8 \mu\text{m}$ QC laser with CW operation up to 320 K [50]. In 2007, X. Wang et al. at Adtech Optics reported a high performance MOCVD-grown QC laser with very low threshold at $\lambda \approx 5 \mu\text{m}$ by using a buried heterostructure [51]. Additionally, K. Fujita et al. at

Hamamatsu Photonics demonstrated a room temperature, CW QC laser at $\lambda \approx 8 \mu\text{m}$ using a modified single phonon resonance-continuum depopulation design [52], and S. Blaser et al. at Alpes Lasers reported a high performance QC laser with less than 2 W power consumption using a low threshold laser material, a shorter 1.5 mm long cavity with back facet HR coated [53]. We currently demonstrated a $\lambda \approx 5.3 \mu\text{m}$, room temperature, CW, QC laser with heat dissipation of 1.2-1.7 W using an even shorter, 0.5 mm laser long cavity with HR coating on both facets [54].

These state of the art QC lasers reported in Refs. [12,13, 37-55] at the time of writing this thesis is summarized in Figure 1.6 in terms of maximum CW operation temperature and maximum CW power at room temperature.

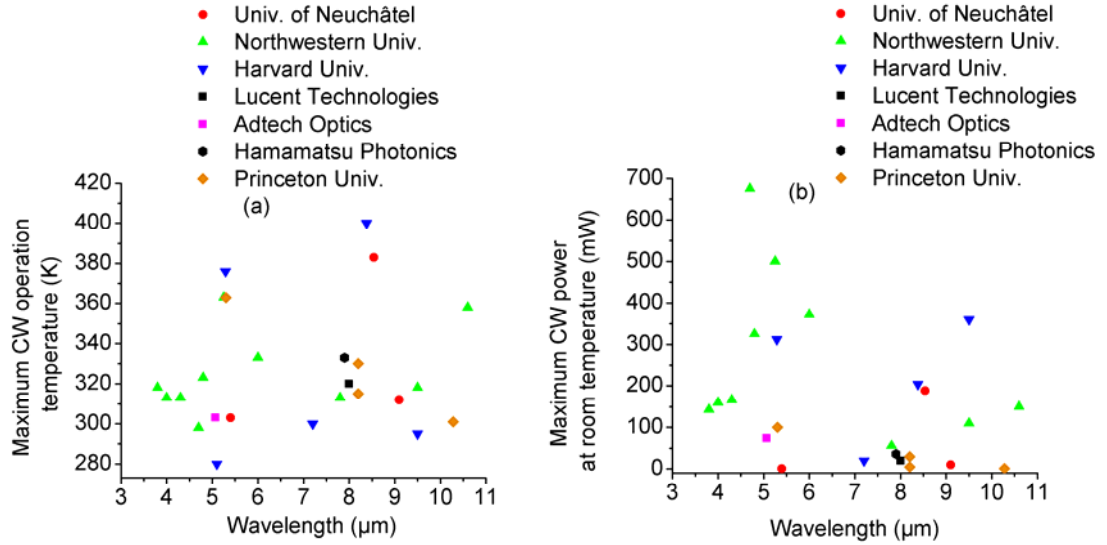


Figure 1.6 (a) Maximum CW operation temperature and (b) maximum CW power at room temperature of the high performing QC lasers reported in the literatures at the time of writing this thesis. These data are taken from Refs. [12, 13, 37-55].

1.5 Motivation and Organization of This Thesis

This dissertation aims to increase the performance of QC lasers for high operating temperature and high optical power in CW mode. For many practical applications of QC lasers, high temperature (room temperature and above), high power, CW operation is desirable in order to simplify the system and allow for more sensitive detection techniques such as wavelength modulation, Cavity Ring Down Spectroscopy (CRDS), and Integrated Cavity Output Spectroscopy (ICOS). A challenge to achieve the high temperature operation is to minimize device self-heating, which results from a high laser threshold and a low wall-plug efficiency. In order to overcome this device self-heating problem so as to increase the operating temperature of QC lasers, this dissertation is devoted to improving the QC laser performance through high gain active region and low loss waveguide designs, and advanced device processing and packaging for better thermal management. Prior to this thesis work, our best performing QC lasers had been limited with a maximum CW operating temperature of \sim 160 K at wavelength of 8 μm . The work conducted in this thesis has increased the CW operating temperature to room temperature at wavelengths of 5.3 and 8.2-10.3 μm .

This thesis is organized as follows. Following this introduction, Chapter 2 describes the optimization of high performance QC lasers at $\lambda \approx$ 8.2 μm for achieving CW operation above room temperature, which includes laser design and simulation, laser fabrication and the corresponding laser testing results. The extension of high performance operation to longer wavelengths between 9.6 and 10.3 μm within the second atmospheric window is given in Chapter 3. Next, a systematic study on the temperature-dependence of the optical gain and loss in these high performance QC lasers at $\lambda \approx$ 8.2-10.3 μm is described

in Chapter 4, In Chapter 5, high performance QC lasers at shorter wavelength, 5.3 μm within the first atmospheric window are presented. Finally a summary of the present work and a discussion of future research directions are given in Chapter 6.

Chapter 2

High Performance Quantum Cascade Lasers at $\lambda \approx 8.2 \mu\text{m}$

2.1 Introduction

This chapter describes the design, fabrication and testing of high performance QC lasers at $\lambda \approx 8.2 \mu\text{m}$.

In order to fabricate high temperature, CW QC lasers, a first key step is the design of a high-gain active region and a low-loss waveguide that have a low threshold current density at all temperatures, as a lower laser threshold current density leads to less power consumption, and thus smaller heat dissipation. Beside the low threshold laser design for minimizing the thermal load, external device packaging is also critical for efficient heat dissipation. Here, by improving these two aspects, the performance optimization of $\lambda \approx 8.2 \mu\text{m}$ QC lasers is presented in the following sections.

2.2 Laser Design and Thermal Modeling

2.2.1 Active Region and Waveguide Designs

The goal of active region design is to obtain a high gain coefficient via optimizing the well/barrier thicknesses. For a specified laser wavelength, the designable terms in the gain coefficient (Equation 1.8 in section 1.2.1) are the lifetimes of the laser levels and the optical dipole matrix element. We take these designable terms as a figure of merit (FOM) to guide the active region design, i.e.

$$\text{FOM} = \tau_4 (1 - \tau_3 / \tau_{43}) z_{43}^2 \quad (2.1)$$

where τ_4 and τ_3 are the lifetimes of the upper and lower laser levels, respectively, τ_{43} is the non-radiative lifetime between the upper and lower laser levels, and z_{43} is the optical dipole matrix element.

Table 2.1 lists three different active region designs for $\lambda \approx 8.2 \mu\text{m}$ QC lasers. They are designed as either “three-well” vertical transition laser with a one phonon resonance extractor, or “four-well” vertical transition laser with a two phonon resonance extractor. As indicated by the design parameters given in Table 2.1, by employing a four-well, vertical transition, two phonon resonance design with the optimized layer thicknesses, the FOM increases from $519 \text{ ps } \text{\AA}^2$ in design I to $653 \text{ ps } \text{\AA}^2$ in design III. Design III was extensively used in our wafer growth and has been used for realizing our first room temperature, CW operation, thus here it is described in more details as below.

Table 2.1 Design parameters for three QC laser active regions at $\lambda \approx 8.2 \mu\text{m}$.

Wafer label	Design feature	τ_4 (ps)	τ_3 (ps)	z_{43} (\AA)	FOM ($\text{ps } \text{\AA}^2$)	
Design I	M329	Three well, vertical transition, one phonon resonance	1.76	0.35	18	519
Design II	D3028	Four well, vertical transition, two phonon resonance	2.18	0.39	17	605
Design III	D3097, D3101, D3103, D3106, D3109, D3110, D3125, M354, M356, M379, A887a, 111605_3	Four well, vertical transition, two phonon resonance	2.11	0.22	18	653

In design III, the laser active region is based on the concept of “two phonon resonance design”, which was first introduced by D. Hofstetter et al. [27] and was successfully used in the demonstration of the first room temperature CW QC laser [12]. This two phonon resonance design has the advantages of high injection efficiency into the upper laser level and fast depopulation of electrons from the lower laser level. By optimizing the well/barrier thicknesses for achieving a high gain coefficient for the laser transition at $\lambda \approx 8 \mu\text{m}$, the layer sequence (in Å) of one period of active region and injector is designed as **44/18/9/57/11/54/12/45/**25**/34/14/33/13/32/**15**/31/19/29/23/27/25/27** in direction of electron flow, where $\text{In}_{0.52}\text{Al}_{0.48}\text{As}$ barrier layers are in bold, $\text{In}_{0.53}\text{Ga}_{0.47}\text{As}$ well layers are in roman, and the n-doped layers are underlined. The electron energy band diagram is shown in Figure 2.1. The energy of the laser transition between levels 4 and 3 is designed as 154 meV ($\lambda = 8 \mu\text{m}$), and levels 1, 2 and 3 are each separated by about one LO phonon energy, through which electrons are depopulated via consecutive two LO phonon resonant emissions and tunneling out into the injector. The lifetime of the upper laser level is designed as $\tau_4=2.11 \text{ ps}$, and that of lower laser level is $\tau_3=0.22 \text{ ps}$. The dipole matrix element z_{43} is 1.8 nm. The energy separation between level 3 and the ground state of the next down stream injector is optimized as 147 meV to suppress the thermal backfilling effect and at the same time to avoid too high threshold voltage, as is later described in section 2.2.2.

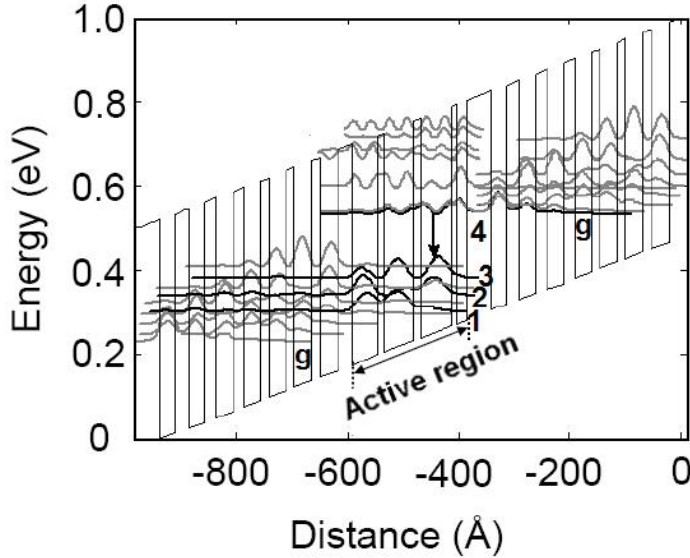


Figure 2.1 Portion of the conduction band diagram and the moduli squared of the relevant wave functions of a $\lambda \approx 8 \mu\text{m}$ QC laser with a four quantum-well active region based on a two phonon resonance design. An electric field of 51 kV/cm is applied. The vertical arrow indicates the laser transition.

The waveguide design of the first laser is shown in Figure 2.2. It is a ternary cladding, plasmon-enhanced dielectric waveguide. Thirty-five periods of active regions and injectors are used as active laser core, and sandwiched between two low-doped ($n = 5 \times 10^{16} \text{ cm}^{-3}$) $\text{In}_{0.53}\text{Ga}_{0.47}\text{As}$ layers, which have the role of enhancing optical mode confinement. The bottom cladding of the waveguide is the low-doped ($n = 2 \times 10^{17} \text{ cm}^{-3}$) InP substrate, and the top cladding consists of two low-doped ($n = 1 \times 10^{17}$ and $2 \times 10^{17} \text{ cm}^{-3}$) $\text{In}_{0.52}\text{Al}_{0.48}\text{As}$ layers, followed by a highly doped ($n = 8 \times 10^{18} \text{ cm}^{-3}$) $\text{In}_{0.53}\text{Ga}_{0.47}\text{As}$ plasmon layer, and a thin heavily doped ($n = 1 \times 10^{20} \text{ cm}^{-3}$) $\text{In}_{0.53}\text{Ga}_{0.47}\text{As}$ cap layer. The highly doped ($n = 8 \times 10^{18} \text{ cm}^{-3}$) $\text{In}_{0.53}\text{Ga}_{0.47}\text{As}$ layer serves as “plasmon” layer with a low refractive index, which reduces the coupling between the optical mode and top metal contact, thus helping to reduce the loss [32]. The calculated fundamental TM mode

profile is shown in Figure 2.2 (b). Its mode confinement factor Γ is 0.65, and the calculated free carrier absorption loss α_w is 7.4 cm^{-1} .

(a) Structure of M354, D3103				
n++	GaInAs	$1 \times 10^{20} \text{ cm}^{-3}$	100 Å	
n	GaInAs	$8 \times 10^{18} \text{ cm}^{-3}$	3500 Å	
n	$\text{Ga}_{0.5x}\text{Al}_{0.5(1-x)}\text{InAs}$ grading V	$2 \times 10^{17} \text{ cm}^{-3}$	250 Å	
n	AlInAs	$2 \times 10^{17} \text{ cm}^{-3}$	8000 Å	
n	AlInAs	$1 \times 10^{17} \text{ cm}^{-3}$	15000 Å	
n	$\text{Ga}_{0.5x}\text{Al}_{0.5(1-x)}\text{InAs}$ grading IV	$1 \times 10^{17} \text{ cm}^{-3}$	250 Å	
n	GaInAs	$5 \times 10^{16} \text{ cm}^{-3}$	3000 Å	
n	$\text{Ga}_{0.5x}\text{Al}_{0.5(1-x)}\text{InAs}$ grading VI	$1 \times 10^{17} \text{ cm}^{-3}$	139 Å	
				Repeat
n	$\text{Ga}_{0.5x}\text{Al}_{0.5(1-x)}\text{InAs}$ grading II	$2 \times 10^{17} \text{ cm}^{-3}$	322 Å	35×
Undoped	Active region		275 Å	
n	$\text{Ga}_{0.5x}\text{Al}_{0.5(1-x)}\text{InAs}$ grading III	$1 \times 10^{17} \text{ cm}^{-3}$	137 Å	
n	GaInAs	$5 \times 10^{16} \text{ cm}^{-3}$	5000 Å	
n	$\text{Ga}_{0.5x}\text{Al}_{0.5(1-x)}\text{InAs}$ grading I	$1 \times 10^{17} \text{ cm}^{-3}$	250 Å	
n	InP	$2 \times 10^{17} \text{ cm}^{-3}$		

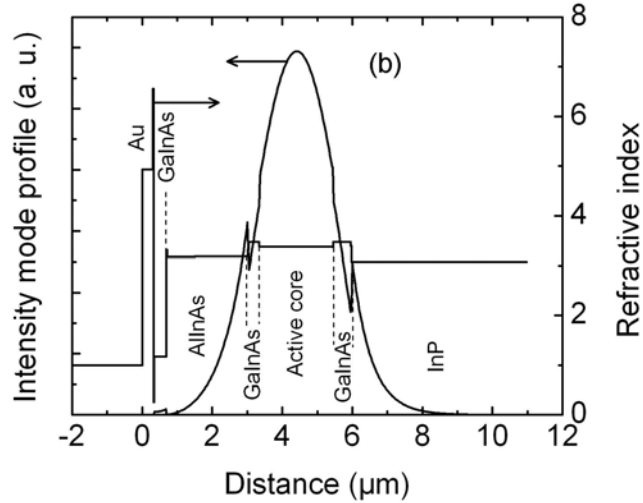


Figure 2.2 (a) Layer structure of a ternary cladding waveguide design for a $\lambda \approx 8 \mu\text{m}$ QC laser. (b) Intensity profile of the fundamental TM mode and profile of the real part of the refractive index of the dielectric waveguide.

In the above waveguide structure, the doping level in each waveguide layer was carefully optimized in order to obtain a low waveguide loss and thus a low laser threshold. Figure 2.3 (a) shows the calculated threshold current density in pulsed mode at 300 K for a 2 mm long QC laser as a function of the doping level in the injector region. When the doping level increases from 5×10^{16} to $1 \times 10^{18} \text{ cm}^{-3}$, the threshold current density monotonously increases due to higher free carrier absorption. Therefore the doping level should be chosen as low as possible. However, as the maximum tunneling current in QC laser is proportional to the doping sheet density, a certain amount of doping level is needed to be able to reach the laser threshold. Based on these considerations, we used a convenient low doping level of $2 \times 10^{17} \text{ cm}^{-3}$ for the design in Figure 2.2. Additionally, considering the fact that the actual doping level depends on the background doping of each growth machine, we used three other higher or lower doping levels at 5×10^{16} , 4×10^{17} and $7 \times 10^{17} \text{ cm}^{-3}$ for several wafers (listed in Table 2.2 of section 2.5).

Fig 2.3 (b) shows the calculated threshold current density in pulsed mode at 300 K as a function of doping level in the 15000 Å thick AlInAs top cladding layer. Again, the threshold increases with the doping level. Therefore the doping level in this cladding layer should also be as low as possible. However, this layer needs to be doped at certain level to avoid resistance heating. For the design in Figure 2.2, we used a low doping level of $1 \times 10^{17} \text{ cm}^{-3}$.

Figure 2.3 (c) shows the calculated threshold current density in pulsed mode at 300 K as a function of the doping level in the 3500 Å thick InGaAs plasmon layer. As mentioned in section 1.2.2, this plasmon layer needs to be doped enough so that the coupling between the optical mode and the metal contact is suppressed. However, a too

high doping level induces larger free carrier absorption. As shown in Figure 2.3 (c), the optimum value exists at $\sim 8 \times 10^{18} \text{ cm}^{-3}$, which is used in the design given in Figure 2.2.

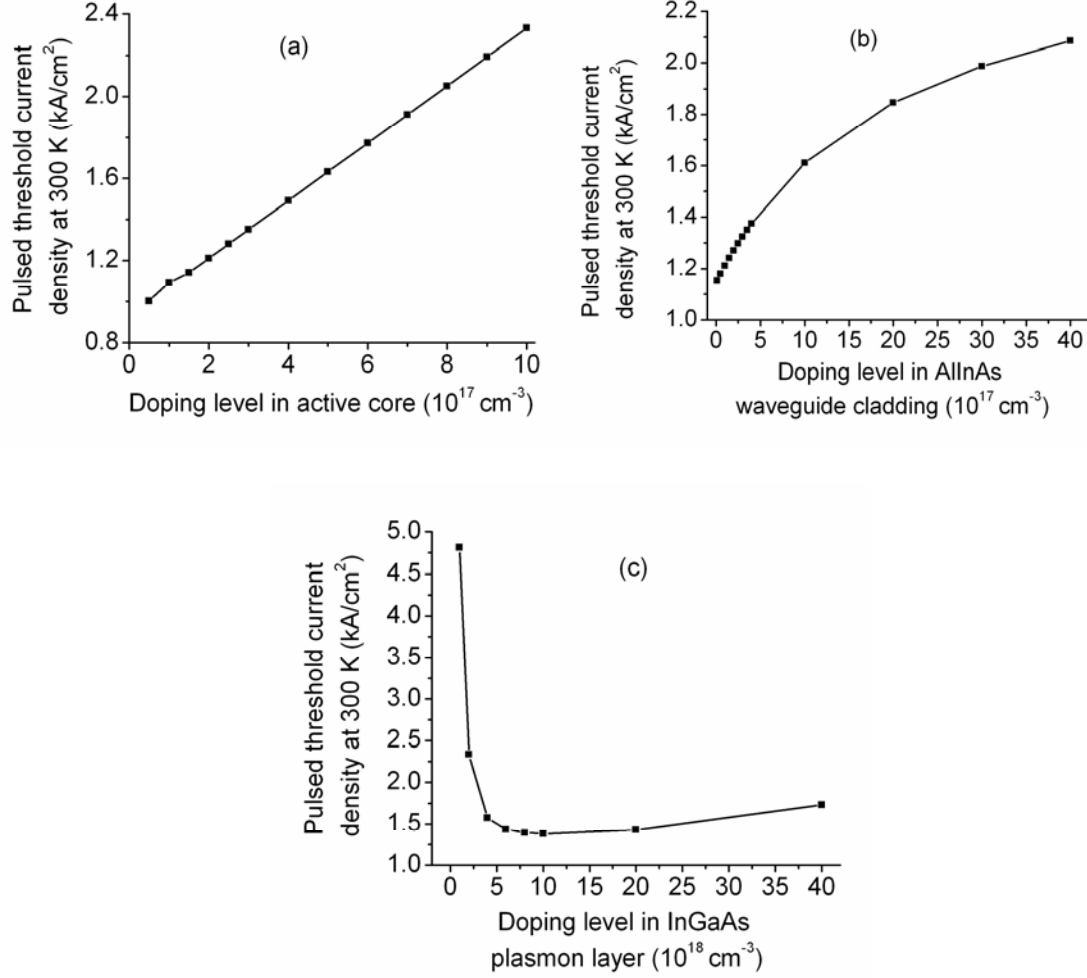


Figure 2.3 Calculated pulsed threshold current density at 300 K for a 2 mm long QC laser as a function of the doping level in three waveguide layers, i.e. (a) injector region, (b) AlInAs top cladding layer, and (c) InGaAs plasmon layer in the waveguide structure shown in Figure 2.2.

Aside from using $\text{In}_{0.52}\text{Al}_{0.48}\text{As}$ as top waveguide claddings, InP is a better material choice, which has a lower refractive index, a lower loss and a higher thermal conductivity thus providing larger optical mode confinement, lower laser threshold and more efficient heat transfer [34]. An InP-cladding waveguide design is shown in Figure 2.4. Thirty-five

(a) Structure of A887a, D3109				
n++	InP		$2 \times 10^{19} \text{ cm}^{-3}$	100 Å
n	InP		$8 \times 10^{18} \text{ cm}^{-3}$	10000 Å
n	InP		$1 \times 10^{17} \text{ cm}^{-3}$	20000 Å
n	$\text{Ga}_{0.5x}\text{Al}_{0.5(1-x)}\text{InAs}$ grading InP		$1 \times 10^{17} \text{ cm}^{-3}$	250 Å
n	GaInAs		$5 \times 10^{16} \text{ cm}^{-3}$	5000 Å
n	$\text{Ga}_{0.5x}\text{Al}_{0.5(1-x)}\text{InAs}$ grading VI		$1 \times 10^{17} \text{ cm}^{-3}$	139 Å
n	$\text{Ga}_{0.5x}\text{Al}_{0.5(1-x)}\text{InAs}$ grading II		$2 \times 10^{17} \text{ cm}^{-3}$	322 Å
Undoped	Active region			275 Å
				Repeat 35x
n	$\text{Ga}_{0.5x}\text{Al}_{0.5(1-x)}\text{InAs}$ grading III		$1 \times 10^{17} \text{ cm}^{-3}$	137 Å
n	GaInAs		$5 \times 10^{16} \text{ cm}^{-3}$	5000 Å
n	$\text{Ga}_{0.5x}\text{Al}_{0.5(1-x)}\text{InAs}$ grading I		$1 \times 10^{17} \text{ cm}^{-3}$	250 Å
n	InP		$2 \times 10^{17} \text{ cm}^{-3}$	

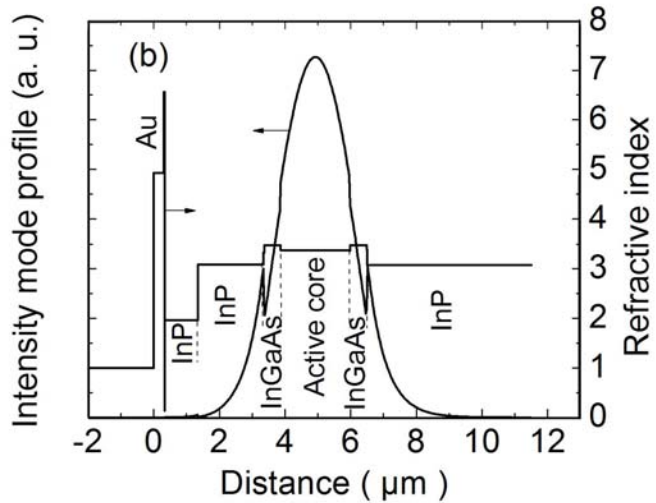


Figure 2.4 (a) Layer structure of binary InP cladding waveguide design for a $\lambda \approx 8 \mu\text{m}$ QC laser. (b) Intensity profile of the fundamental TM mode and profile of the real part of the refractive index of the dielectric waveguide.

periods of active regions and injectors are used as the active laser core and sandwiched between two 0.5 μm -thick n-doped ($5 \times 10^{16} \text{ cm}^{-3}$) $\text{In}_{0.53}\text{Ga}_{0.47}\text{As}$ layers. The upper cladding layers consists of 2 μm -thick n-doped ($1 \times 10^{17} \text{ cm}^{-3}$) InP, followed by a 1 μm -thick n-doped ($8 \times 10^{18} \text{ cm}^{-3}$) InP plasmon layer and a 0.01 μm -thick heavily doped ($2 \times 10^{19} \text{ cm}^{-3}$) InP cap layer. The calculated intensity profile of the fundamental TM mode is shown in Figure 2.4 (b). The waveguide loss α_w is calculated as 6.6 cm^{-1} , and the confinement factor Γ is 0.67.

2.2.2 Thermal Modeling

Aside from designing a high gain active region and a low loss waveguide, external device packaging for thermal management is also crucial for improving the operating temperature of QC lasers in CW mode. A thermal model helps to choose a suitable device packaging and layout and to optimize some laser design parameters.

To calculate the temperature profile of the device, one basically needs to solve the following thermal conduction equation:

$$\nabla \bullet (-\kappa \nabla T) = Q = \frac{J_{th} S V_{th}}{Sh} = \frac{J_{th} V_{th}}{h} \quad (2.2)$$

where κ is the thermal conductivity, Q is the dissipated power density, V_{th} is the laser threshold voltage, h is the thickness of the laser active core, and S is the area of the laser ridge. Equation 2.2 is a steady-state equation, suitable for the thermal modeling of CW operated QC lasers.

At laser threshold, the dissipated power density term contains the laser threshold current density J_{th} , which increases with laser core temperature for the reasons previously mentioned. On the other hand the laser core temperature is determined by the thermal

conduction itself. Therefore, the thermal conduction equation needs to be solved self-consistently. The algorithm for solving the thermal conduction equation and calculating the temperature in the core of a QC laser is described in Figure 2.5.

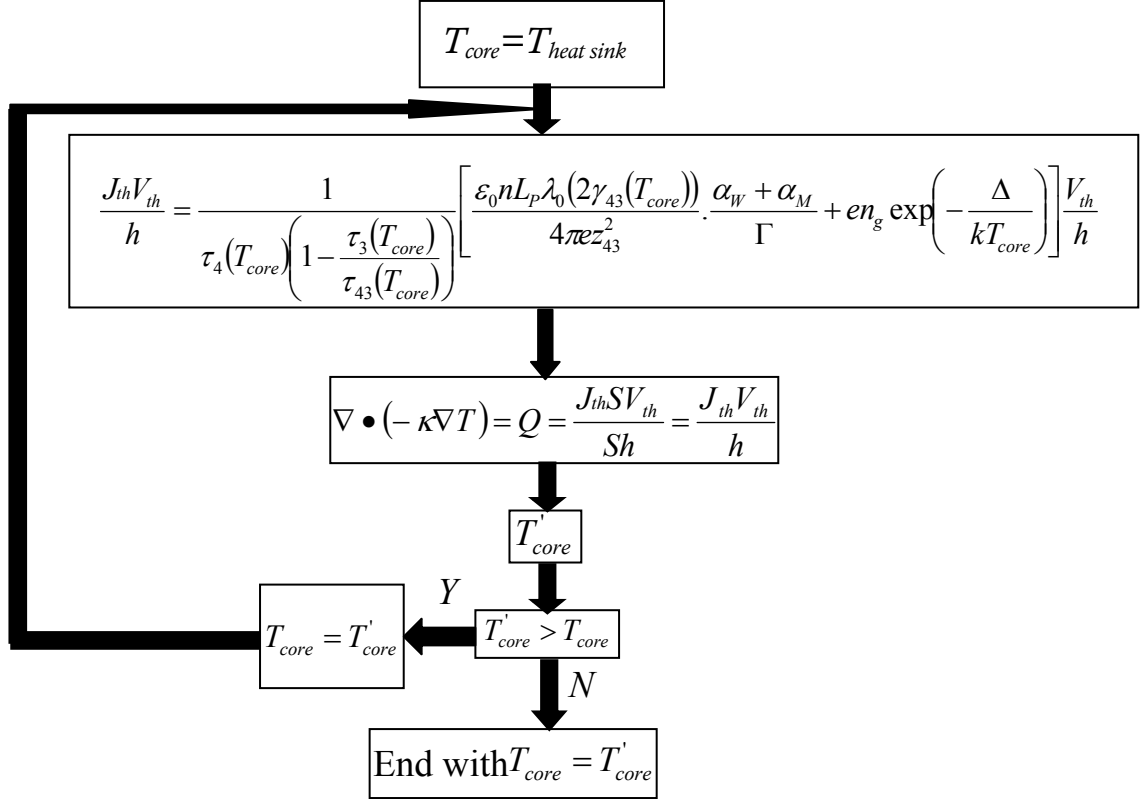


Figure 2.5 Schematic work-flow of the self-consistent method for the thermal modeling of QC lasers.

First the laser core temperature T_{core} is set to be at the heat sink temperature $T_{heat\ sink}$, and then the thermal conduction equation is solved using commercial software COMSOL [56] based on finite element analysis to obtain the new laser core temperature T'^{core} , which will be higher than its initial value. With the higher new core temperature, one calculates the new higher dissipated power density and solves the thermal conduction equation again. This process is repeated until the laser core temperature converges to a certain value, which is the solution of the problem. If the calculation of the laser core temperature does not converge, then there is no solution for the thermal conduction

equation and the laser will not function in CW mode at this heat sink temperature. It is noted that this iteration method is sensitive to the initial choice of laser core temperature T_{core} . Different choices of the first T_{core} , either equal to, or less/larger than $T_{heat\ sink}$, have been tested. The convergence is confirmed to be robust if a solution exists for the thermal conduction equation for particular device geometry. However, the speed of the convergence depends on how close the first T_{core} to the final solution.

The thermal conductivities of InP and $In_{0.53}Ga_{0.47}As$ can be found in Refs. [57] and [58], and are plotted in Figures 2.6 and 2.7, respectively. However, for $In_{0.52}Al_{0.48}As$, experimental data of the thermal conductivity were not found. So here we use linear interpolation from its corresponding binary materials, and find that its thermal conductivity is 1.23 times of that of $In_{0.53}Ga_{0.47}As$. This scale factor is close to the value used in Ref. [59].

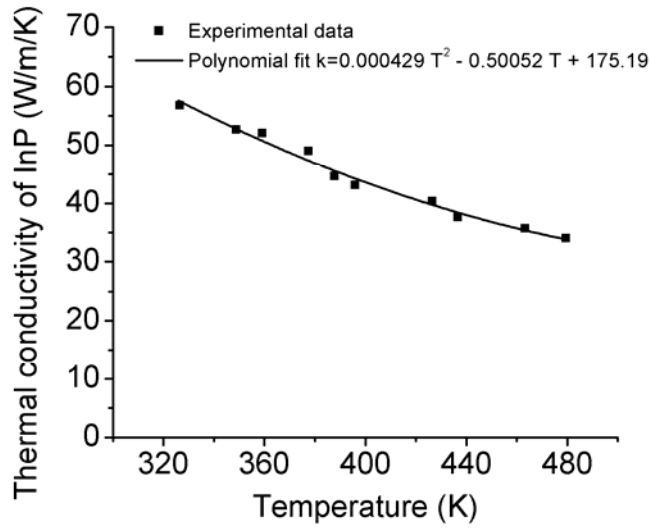


Figure 2.6 Experimental thermal conductivity of InP at different temperatures (after Ref. [57]).

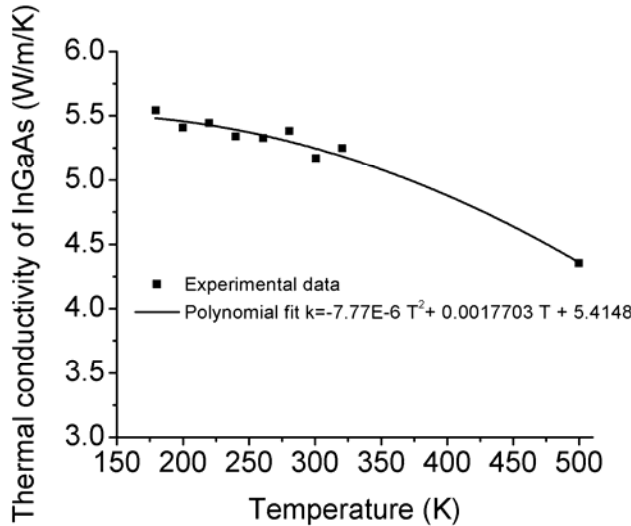


Figure 2.7 Experimental thermal conductivity of $\text{In}_{0.53}\text{Ga}_{0.47}\text{As}$ at different temperatures (after Refs. [57] and [58])

For the thermal conductivity of laser active core, since it is composed of an $\text{In}_{0.53}\text{Ga}_{0.47}\text{As}/\text{In}_{0.52}\text{Al}_{0.48}\text{As}$ superlattice, its thermal conductivity is different from that of bulk material because of interface effects and its highly layered structure [60]. Here we extract the thermal conductivity of the laser active core from an exemplary room temperature CW QC laser in Ref. [13]. From the reported laser threshold current density in both pulsed and CW modes, the laser core temperature in CW can be determined by the temperature that gives the same threshold current density in pulsed mode. Following that and using the thermal model described above, the unknown laser core thermal conductivity (as a fitting parameter) can be obtained. During this process, we neglect the anisotropic nature of the laser core, and assume a constant thermal conductivity of the laser active core. In fact, as the cross-plane thermal conductivity is one order of magnitude smaller than the in-plane thermal conductivity [61], the laser core temperature is mainly determined by the cross-plane thermal conductivity, and a change in in-plane thermal conductivity gives negligible temperature variation. Therefore it is reasonable to

assume a constant thermal conductivity in the model. The results are given in Figure 2.8. As expected for a layered structure, the thermal conductivity of the laser active core is nearly half of that of its bulk counterparts, and decreases with temperature.

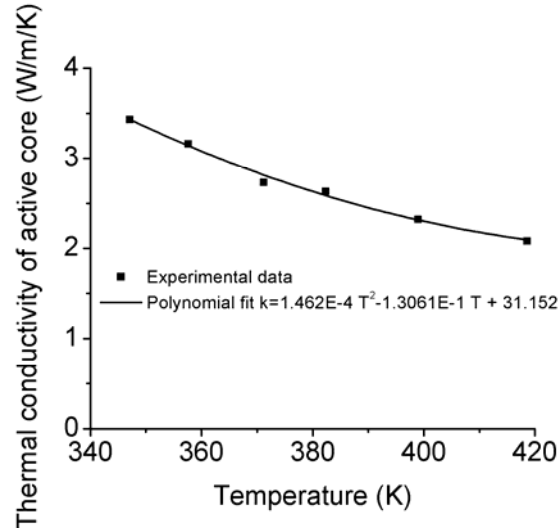


Figure 2.8 Thermal conductivity of laser active core extracted from experimental data on QC lasers reported in Ref. [13].

Using the above material parameters, thermal modeling has been performed for several lasers and here we show results for a 2 mm long, 10 μm wide, back facet HR coated laser with different device packagings and layouts. Figure 2.9 is the result for an epitaxial-side-up mounted, ternary waveguide cladding, ridge waveguide laser with thin metal top contact. After five iterations, the calculation of the laser core temperature shows no sign of converging, starts diverging, and there is no solution for the thermal conduction equation, and hence the device does not work in CW at room temperature in this packaging configuration. Figure 2.10 is the result for an epitaxial-side-up mounted, ternary waveguide cladding, ridge waveguide laser with thick metal top contact. The

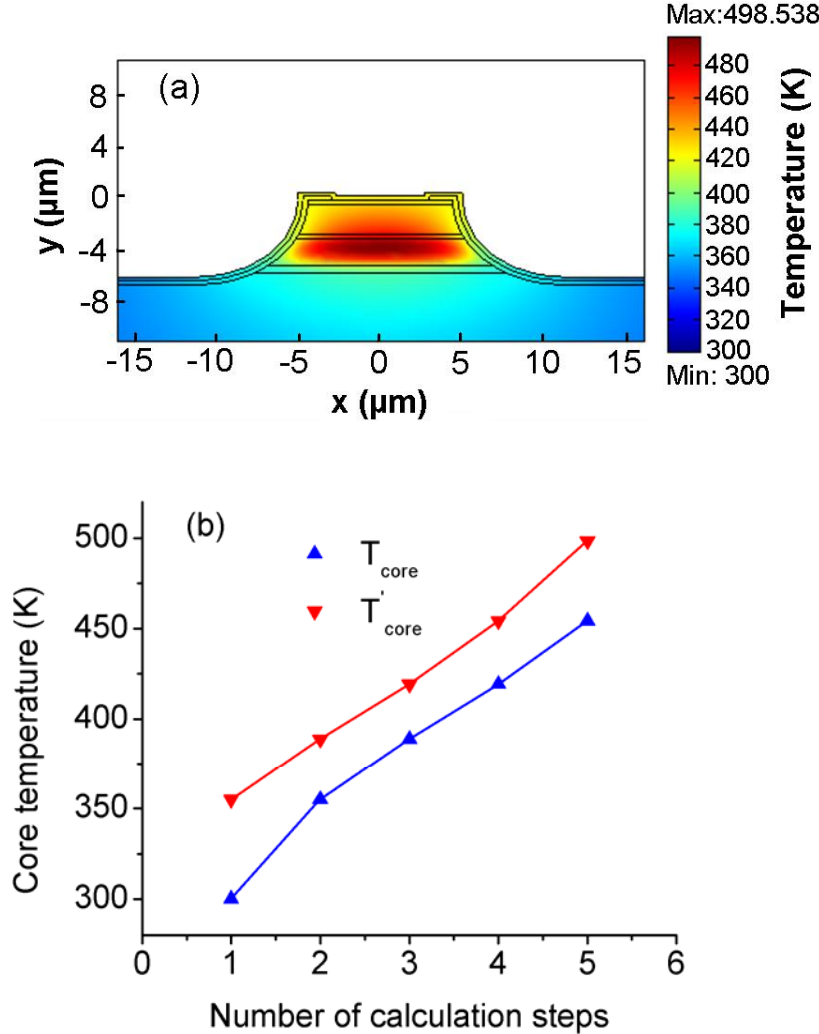


Figure 2.9 Temperature distribution (a), and laser core temperatures T_{core} and T'_{core} (b) at different iterations of core temperature for an epitaxial-side-up mounted, ternary waveguide cladding, 2 mm long, 10 μm wide, back facet high reflectivity (HR) coated, ridge waveguide laser with thin metal top contact at $\lambda \approx 8 \mu\text{m}$.

thick gold contact enhances lateral heat transfer from the laser active core into the surrounding InP substrate, thus allowing more efficient heat dissipation [13]. After ten iterations, the active core temperature approaches 371 K, and the device is predicted to function in CW mode at room temperature with the aid of thick gold contact. Moreover, the more advanced epitaxial-side-down mounting [62] brings the laser active core closer

to the heat sink temperature, thus allowing more efficient heat removal. This result is shown in Figure 2.11. The laser core temperature is lowered to 336 K, which is an about 35 K improvement compared to the epitaxial-side-up mounted device in Figure 2.10.

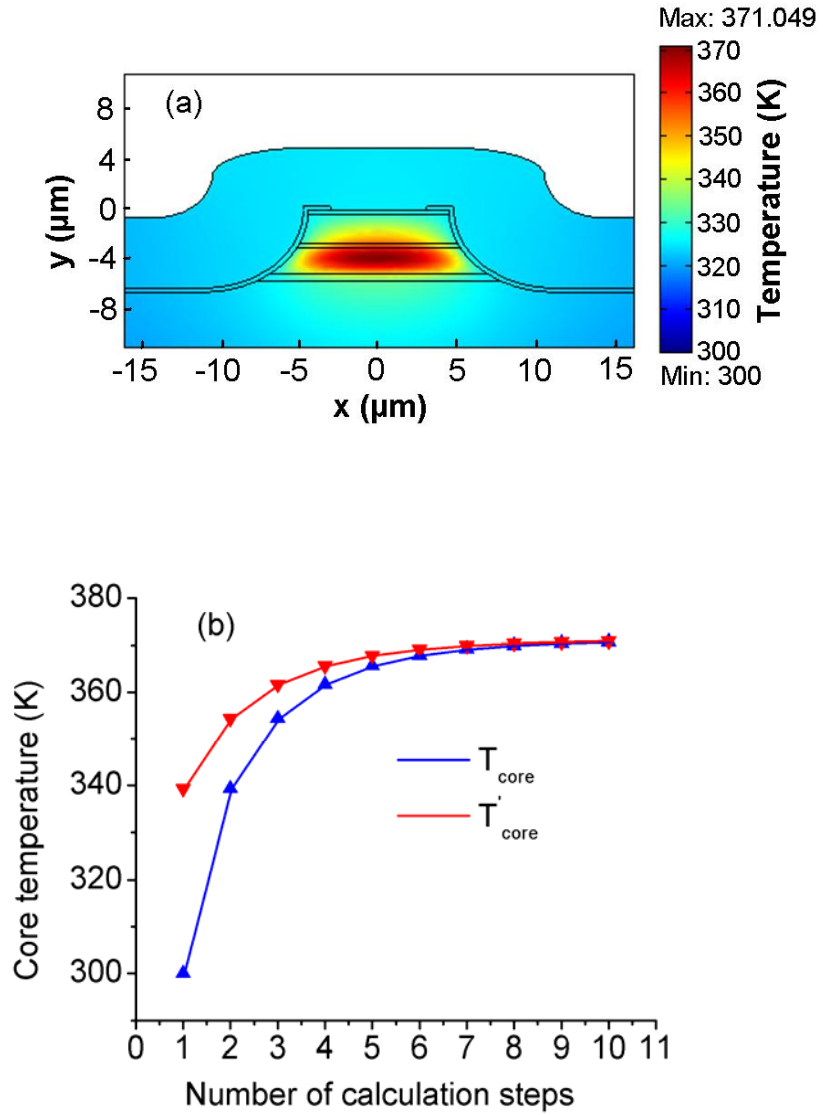


Figure 2.10 Temperature distribution (a), and laser core temperatures T_{core} and T'_{core} (b) at different iterations of core temperature for an epitaxial-side-up mounted, ternary waveguide cladding, 2 mm long, 10 μm wide, back facet high reflectivity (HR) coated, ridge waveguide laser with thick metal top contact at $\lambda \approx 8 \mu\text{m}$.

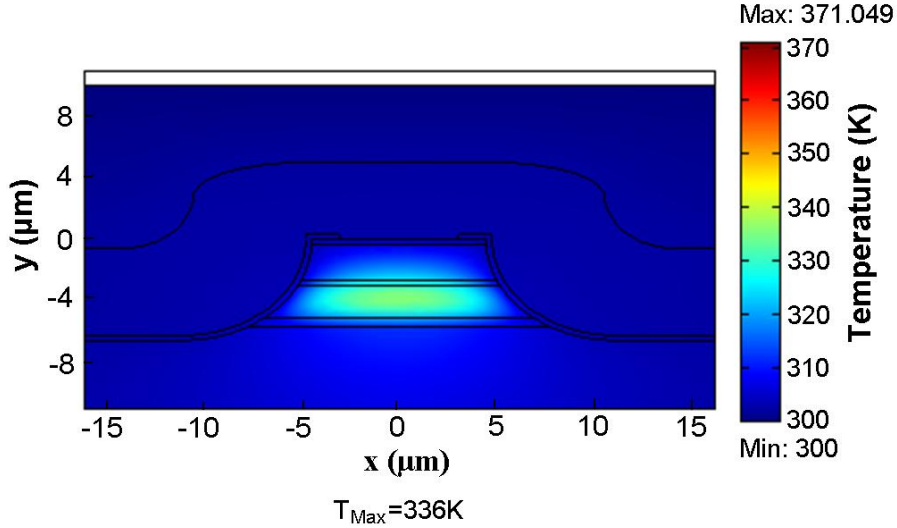


Figure 2.11 Temperature distribution for an epitaxial-side-down mounted, ternary waveguide cladding, 2 mm long, 10 μm wide, back facet high reflectivity (HR) coated, ridge waveguide laser with thick metal top contact at $\lambda \approx 8 \mu\text{m}$.

As mentioned in section 2.2.1, from the point of view of thermal management, there is a trade-off in the design of Δ , which is the energy spacing between the lower laser level of one active region and the ground state of the next down steam injector. As shown in Figure 2.12 (a), when the backfill energy Δ increases, there is less thermal backfilling (less thermal population as indicated by Equation 1.16 in section 1.3), and the laser threshold becomes smaller. However, the threshold voltage, given by $V_{th}=N(\Delta+h\omega)$, increases linearly with Δ as shown in Figure 2.12 (b). Therefore for the minimal heat dissipation power $I_{th} \times V_{th}$, there is an optimum value for Δ . As shown in Figure 2.12 (c), the heat dissipation power decreases sharply with Δ first, and then it reaches a minimum at $\Delta \sim 160\text{meV}$, and after that, it increases slowly with Δ . The corresponding active core temperature follows the same trend of heat dissipation power as shown in Figure 2.12 (d). Therefore the optimum value of Δ for low laser core temperature and room temperature,

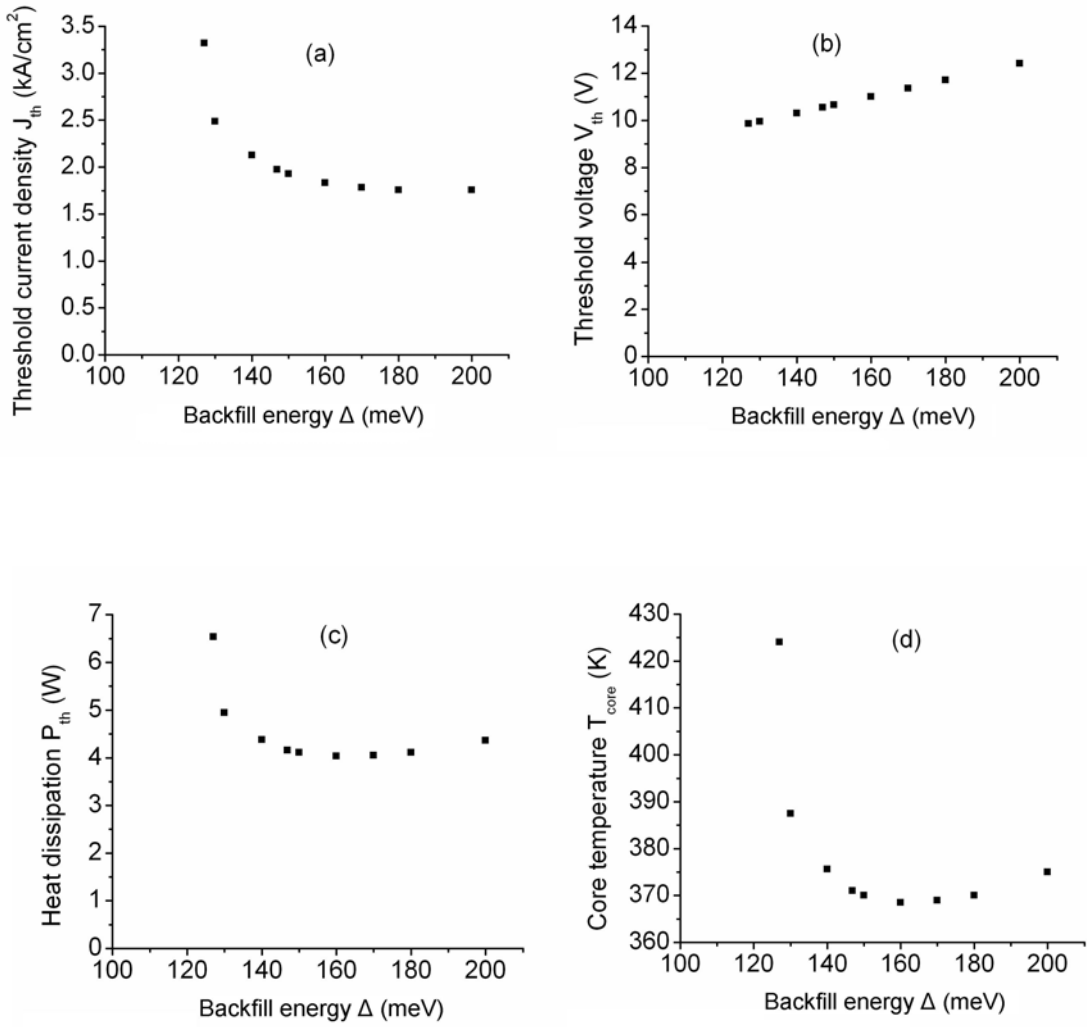


Figure 2.12 Threshold current density (a), threshold voltage (b), heat dissipation power (c), and core temperature (d) as a function of Δ , the energy difference between the lower laser level of one active region and the ground state of the next down steam injector.

CW operation is ~ 160 meV, and in the active region design in section 2.2.1, we designed Δ to be 147 meV, close to this optimum value.

Aside from the above laser with ternary waveguide cladding, the InP waveguide cladding has better capability of heat conduction because of a larger thermal conductivity, as well as a lower refractive index and a lower loss leading to lower threshold current

density J_{th} . The temperature map for an epitaxial-side-up mounted, InP waveguide cladding, ridge waveguide laser with thick metal top contact is shown in Figure 2.13. The core temperature is 340 K, which is 31 K lower than that of a ternary waveguide cladding device in a similar packaging configuration. The result for an epitaxial-side-down mounted device is given in Figure 2.14, and there is an additional 17 K improvement in the laser core temperature. Besides the ridge waveguide lasers with thick metal top contact, the buried heterostructure (BH) QC laser with thick metal top contact is an even better layout for heat dissipation owing to two advantages [63]. First, the lateral regrown InP avoids the overlap between the optical mode and side-wall metallization, thus resulting in a lower waveguide loss. Second, the insulating lateral InP replaces the Si_xN_y or SiO_2 layers for current injection, thus it has a higher thermal conductivity. The result for an epitaxial-side-up mounted BH QC laser with thick metal top contact is shown in Figure 2.15. Its core temperature is 328 K, which is lower by 12 K compared to the ridge waveguide structure with thick metal contact. The epitaxial-side-down mounting for a BH QC laser gives another 10 K improvement in core temperature as shown in Figure 2.16.

In summary, from the thermal calculation for different packaging layouts, CW room temperature operation can be achieved for ridge waveguide lasers with thick metal top contact and BH lasers with thick metal top contact. The epitaxial-side-down mounted BH laser with thick metal top contact represents the best layout for heat dissipation, and hence room temperature, CW operation. While shown here is for $\lambda \approx 8 \mu\text{m}$ QC lasers, this is a general result that can be broadly used.

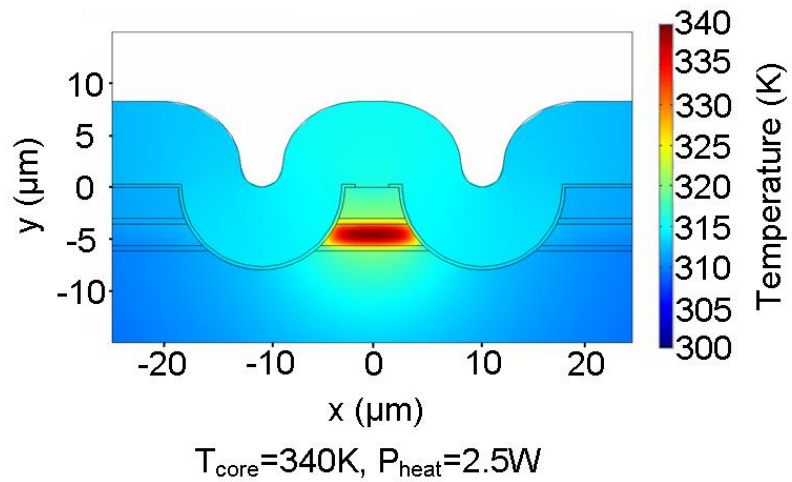


Figure 2.13 Temperature distribution of an epitaxial-side-up mounted, InP waveguide cladding, 2 mm long, 10 μm wide, back facet high reflectivity (HR) coated, ridge waveguide laser with thick metal top contact at $\lambda \approx 8 \mu\text{m}$.

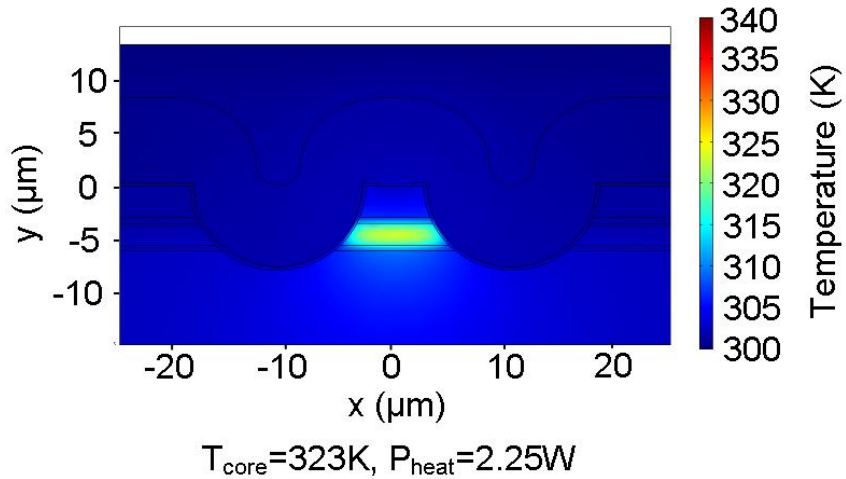


Figure 2.14 Temperature distribution of an epitaxial-side-down mounted, InP waveguide cladding, 2 mm long, 10 μm wide, back facet high reflectivity (HR) coated, ridge waveguide laser with thick metal top contact at $\lambda \approx 8 \mu\text{m}$.

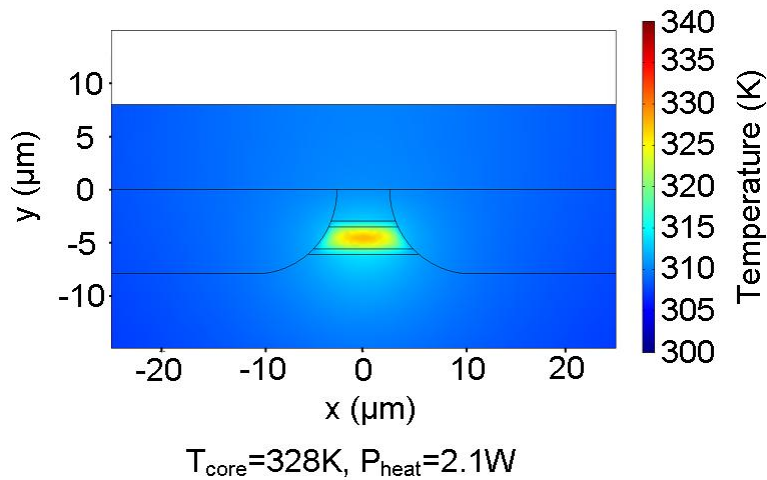


Figure 2.15 Temperature distribution of an epitaxial-side-up mounted, InP waveguide cladding, 2 mm long, 10 μm wide, back facet high reflectivity (HR) coated, buried heterostructure (BH) laser with thick metal top contact at $\lambda \approx 8 \mu\text{m}$.

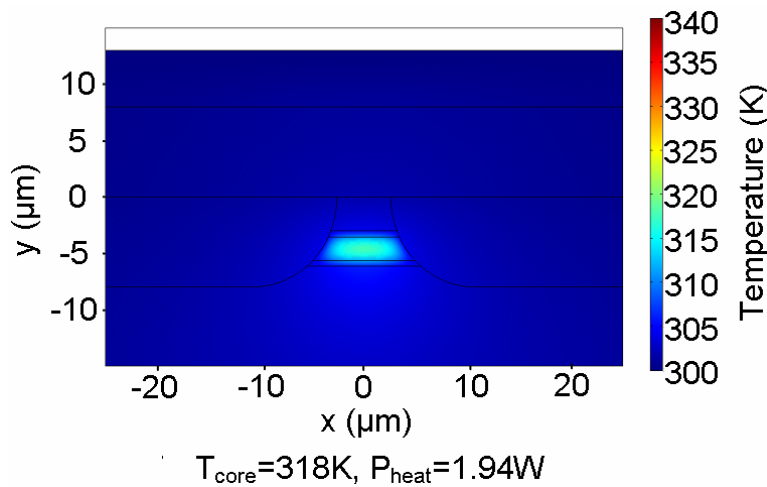


Figure 2.16 Temperature distribution of an epitaxial-side-down mounted, InP waveguide cladding, 2 mm long, 10 μm wide, back facet high reflectivity (HR) coated, buried heterostructure (BH) laser with thick metal top contact at $\lambda \approx 8 \mu\text{m}$.

2.3 Laser Fabrication

2.3.1 Ridge Waveguide Laser with Thin Metal Top Contact

Conventional QC lasers are processed into ridge waveguides with thin metal top contact [64], with detailed processing steps shown in Figure 2.17. First, the laser ridge is defined by conventional photolithography and wet-chemical-etching in HBr/HNO₃/H₂O (1:1:10), and then 0.3 μm Si_xN_y or SiO₂ is deposited on the sample for current confinement by Plasma Enhanced Chemical Vapor Deposition (PECVD). A window is opened on top of the ridge by photolithography and Reactive Ion Etching (RIE). Next, 30 nm Ti and 300 nm Au are evaporated on the sample for top contact and side-wall optical mode confinement using Electron Beam Evaporator. After that, the wafer substrate is thinned to 200 μm for easier cleaving, and 15 nm Ge and 300 nm Au are evaporated for back contact. Finally the sample is cleaved into laser bars with two facets (perpendicular to the laser ridges) defining a Fabry-Perot cavity. A typical laser bar is ~ 2-4 mm long and ~ 1-4 mm wide, and each individual laser ridge is ~ 8-16 μm wide. The laser bar is mounted on a copper mount and wire-bonded for characterization. A typical QC laser cross section after the processing is seen from the Scanning Electron Microscope (SEM) picture in Figure 2.18 (a). Figure 2.18 (b) shows an epitaxial-side-up mounted laser bar with two laser ridges wire-bonded.

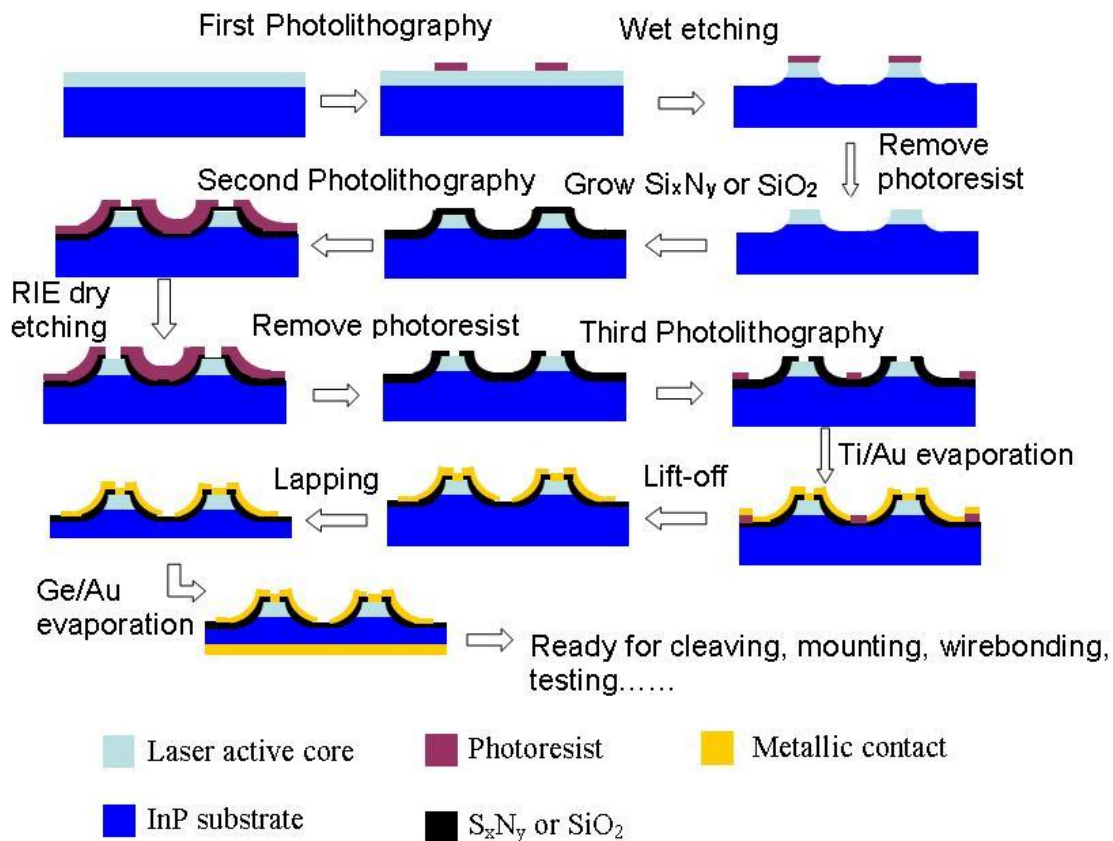


Figure 2.17 Processing steps of a ridge waveguide QC laser with thin metal top contact.

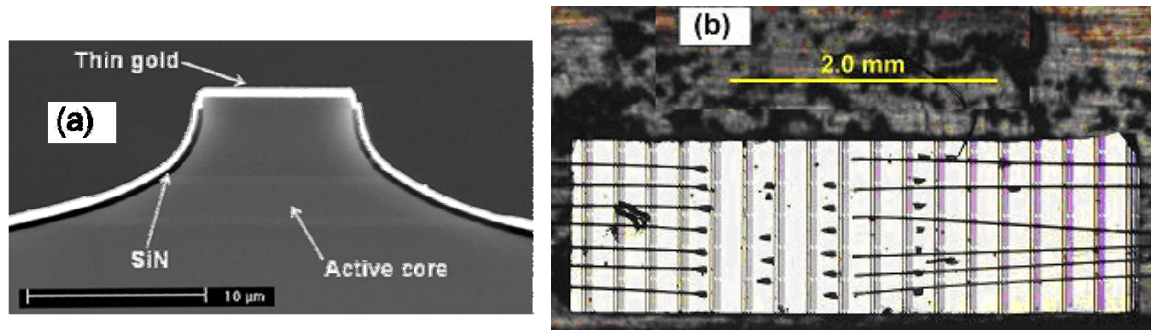


Figure 2.18 (a) Scanning Electron Microscope (SEM) image of a typical ridge waveguide QC laser with thin metal top contact; (b) Optical image of an epitaxial-side-up mounted ridge waveguide laser bar with thin metal top contact.

2.3.2 Ridge Waveguide Laser with Thick Metal Top Contact

As shown in section 2.2.2, one way to improve the heat dissipation is to use a thick gold top contact [13], which enhances heat transfer in both vertical and lateral directions. The processing steps for a ridge waveguide laser with thick metal top contact are shown in Figure 2.19. A double-trench ridge waveguide structure is used because of its relatively flat surface, which facilitates the epitaxial-side-down laser mounting. The double-trench ridge waveguides are fabricated by conventional photolithography and wet-chemical-etching. A 0.3- μm -thick Si_xN_y or SiO_2 layer is deposited for side-wall insulation. After evaporation of Ti/Au (30 nm/300 nm) for the top contact, a 10- μm -thick gold layer is electroplated around the laser ridge in a solution of gold cyanide (Pur-A-Gold 401, Enthone, Inc.) at 65°C for 80 minutes at a constant current of 2.5 mA/cm². To facilitate cleaving, small gaps are left in the thick electroplated gold layer using a photoresist mask. Next, the wafer is thinned to $\sim 150 \mu\text{m}$, which is thinner than that in the processing of ridge waveguide laser with thin metal top contact for more efficient heat dissipation. Finally the back Ge/Au (15 nm/300 nm) contact is evaporated. The laser is mounted epitaxial-side-up to a copper submount with Indium solder, and wire-bonded. A typical QC laser cross section after the processing is seen from the SEM picture in Figure 2.20 (a), and an epitaxial-side-up mounted laser ridge is shown in Figure 2.20 (b).

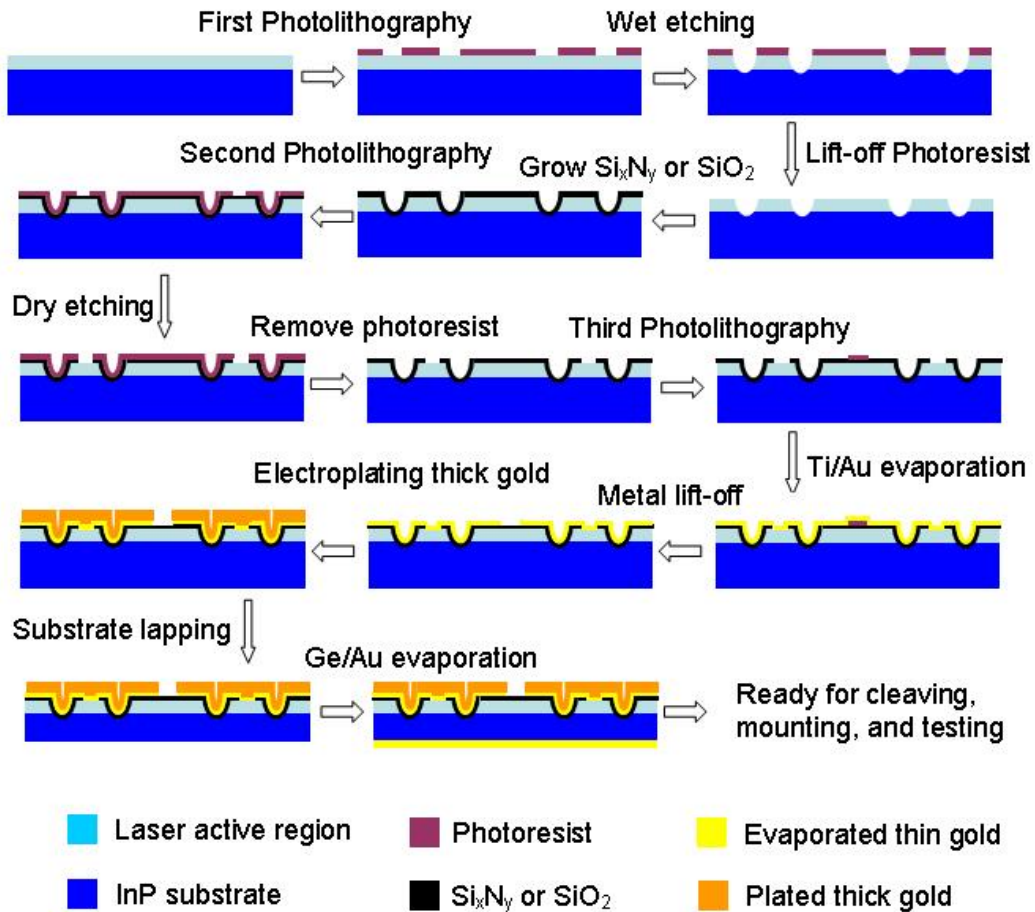


Figure 2.19 Processing steps of a ridge waveguide QC laser with thick metal top contact.

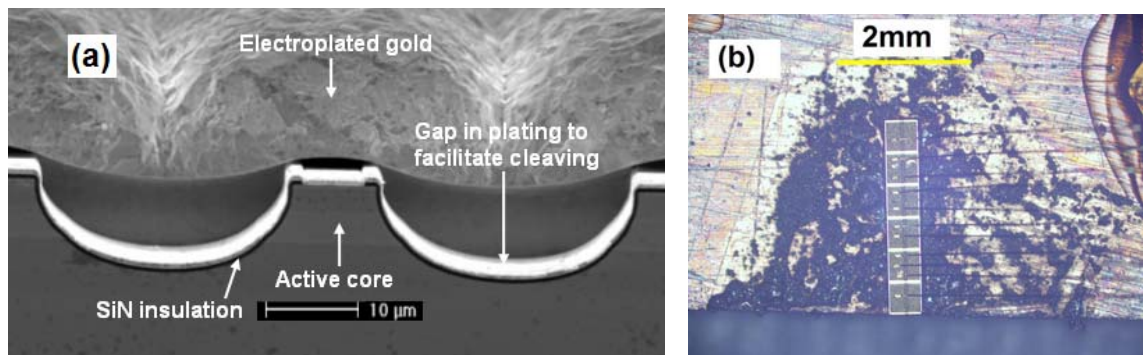


Figure 2.20 (a) Scanning Electron Microscope (SEM) image of a typical ridge waveguide QC laser with thick metal top contact; (b) Optical image of an epitaxial-side-up mounted, ridge waveguide QC laser with thick metal top contact.

2.3.3 Buried Heterostructure Laser with Thick Metal Top Contact

Aside from the ridge waveguide laser with thick metal top contact, the buried heterostructure laser with thick metal top contact provides even better heat transfer capability especially for narrow laser ridge owing to the lateral regrown InP and lateral heat conduction [45]. The processing steps are shown in Figure 2.21. First SiO_2 stripes are deposited on the wafer to define the laser ridges and for selective area InP regrowth later. The stripe direction is chosen as $[01\bar{1}]$ instead of $[011]$ (which is used for the $\lambda \approx 8.2 \text{ }\mu\text{m}$ QC lasers in section 2.5.3) to obtain a better quality InP regrowth. Conventional chemical-wet-etching is used to define the laser ridge, and then the sample is loaded into an MOCVD system for regrowing $\sim 10 \text{ }\mu\text{m}$ thick insulating InP. Next, the SiO_2 layer is removed, a thin top contact is deposited, and thick gold-plating follows. After that, the wafer is thinned to $150 \text{ }\mu\text{m}$, and Ge/Au ($15 \text{ nm}/300 \text{ nm}$) are evaporated for back contact. Finally, the sample is cleaved into single laser bars for mounting and testing. An optical image of the facet of a finished device is shown in Figure 2.22 (a), and an epitaxial-side-up mounted buried herterostructure QC laser with thick metal top contact is shown in Figure 2.22 (b).

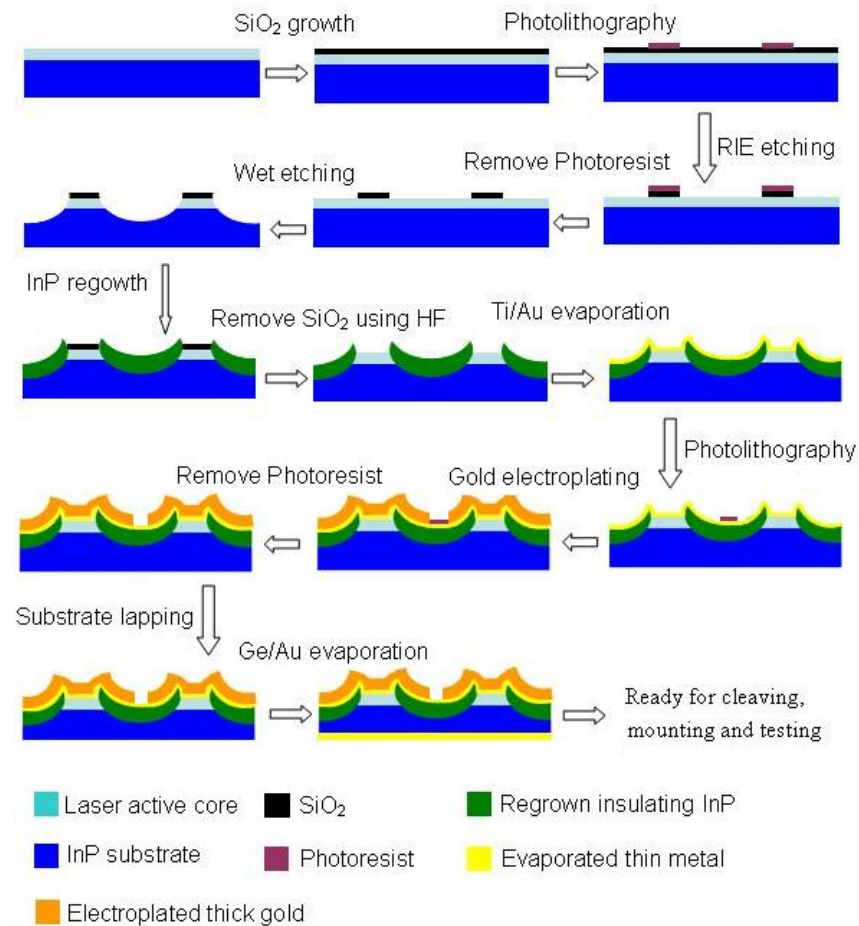


Figure 2.21 Processing steps of a buried heterostructure QC laser with thick metal top contact.

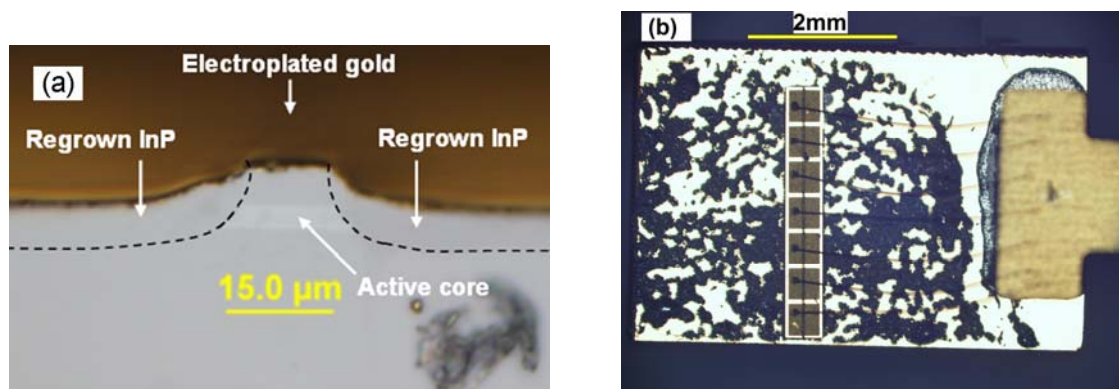


Figure 2.22 (a) Optical image of the facet of a buried heterostructure QC laser with thick metal top contact;
 (b) Optical image of an epitaxial-side-up mounted buried heterostructure QC laser with thick metal top contact.

2.4 Laser Characterization Setups

2.4.1 Spectrum Testing Setup

We use commercial Nicolet Fourier Transform Infrared Spectrometer (FTIR) to measure the laser emission spectrum below or above threshold. The system is based on the principle of Michelson Interferometer. A schematic drawing of the setup is shown in Figure 2.23. The QC laser is loaded into a cryostat with a temperature-controllable cold-finger. The laser is operated in either pulsed mode, with 100 ns pulse width at repetition rate of 80 kHz, or CW mode, and its light emission is collimated with a large aperture ZnSe or Ge lens, and coupled into the FTIR spectrometer for recording the spectrum.

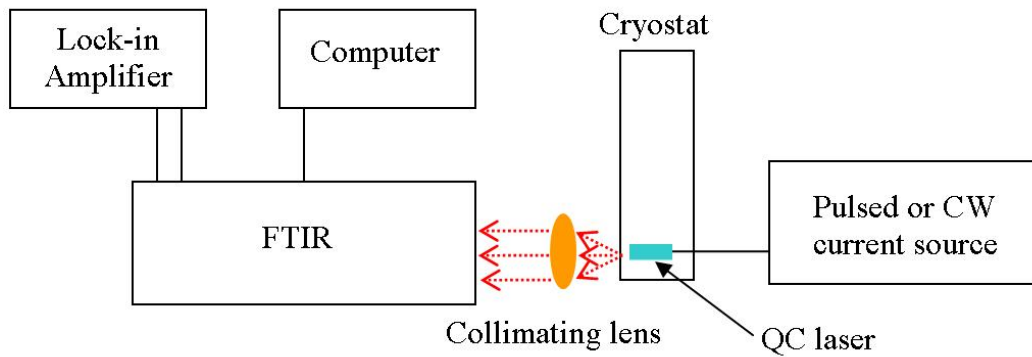


Figure 2.23 Schematic drawing of QC laser spectrum measurement setup.

2.4.2 Light-current-voltage Testing Setups

Figure 2.24 (a) shows the setup for measuring the light-current-voltage (L-I-V) relations of QC lasers in pulsed mode. The laser light is collected via two parallel lenses, and focused to a calibrated fast HgCdTe (MCT) photovoltaic detector. The light, current and voltage are measured using three gated boxcar averagers. A HP analyzer is used to collect the data. The CW L-I-V testing setup is shown in Figure 2.24 (b). The laser output

power is measured using a calibrated power meter. A GPIB control is used to collect the data of laser power, input current and voltage.

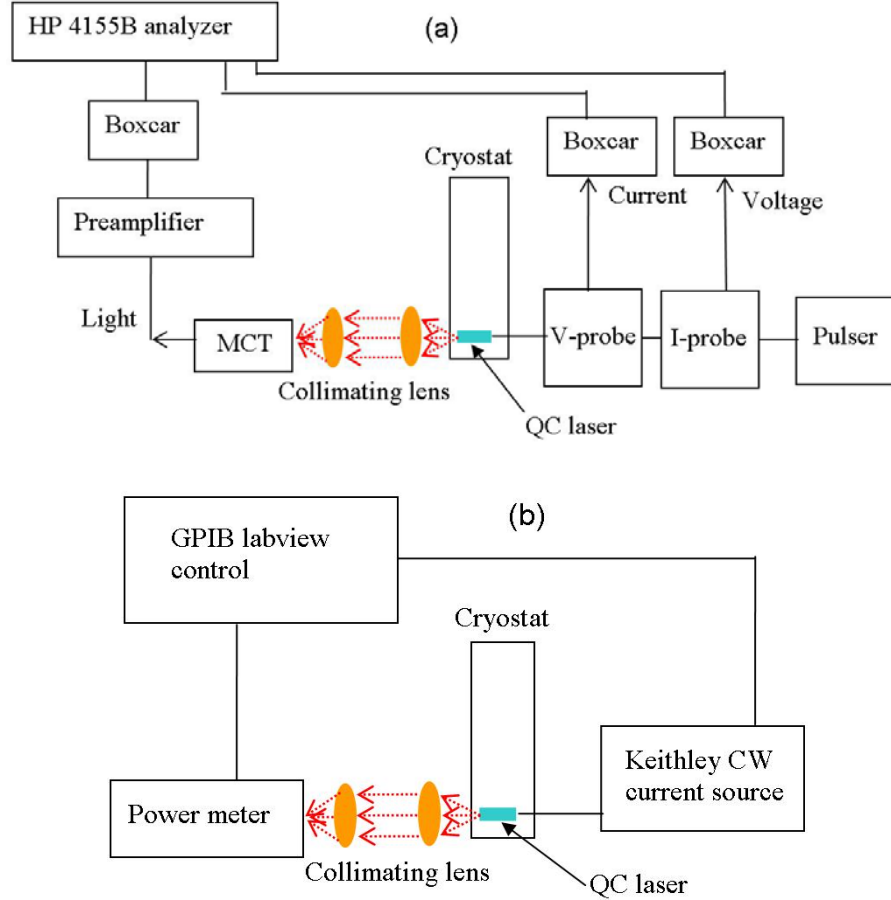


Figure 2.24 Schematic drawing of L-I-V testing setups for QC lasers in pulsed mode (a) and CW (b).

2.5 Laser Testing

We fabricated and tested seventeen $\lambda \approx 8 \mu\text{m}$ QC laser wafers, which are listed in Table 2.2. These samples are based on “three-well” or “four-well” active region designs (listed as Designs I, II, III in Table 2.1 in section 2.2.1) with different doping levels, and ternary AlInAs or binary InP waveguide cladding. They were processed into ridge waveguide QC lasers with thin (“thin gold”) or thick metal top contact (“thick gold”), and

buried heterostructure QC lasers with thick metal top contact. In the following sections 2.5.1-2.5.3, we focus on the most representative and interesting samples.

Table 2.2 QC laser samples at $\lambda \approx 8.2 \mu\text{m}$.

Sample label	Active region design	Waveguide cladding	Doping level (10^{17} cm^{-3})	Fabrication
M329	Design I	InAlAs	2	Thin gold
D2983	Design I	InAlAs	2	Thin gold
D2984	Design I	InAlAs	2	Thin gold
D3028	Design II	InAlAs	2.5	Thin gold
D3029	Design II	InAlAs	2.5	Thin gold
D3097	Design III	InAlAs	7	Thin gold
D3101	Design III	InAlAs	4	Thin gold
D3103	Design III	InAlAs	2	Thin gold
D3106	Design III	InAlAs	0.5	Thin gold
D3109	Design III	InP	2	Thick gold
D3110	Design III	InAlAs	2	Thin gold
				Thick gold
D3125	Design III	InP	2	Thin gold
M354	Design III	InAlAs	2	Thin gold
M356	Design III	InP	2	Thin gold
				Thick gold
M379	Design III	InAlAs	0.5	Thin gold
A887a	Design III	InP	2	Thin gold
				Thick gold
111605_3	Design III	InP	2	Thick gold
				Buried heterostructure

2.5.1 Ridge Waveguide Laser with Thin Metal Top Contact

The $\lambda \approx 8 \mu\text{m}$ design with a ternary waveguide cladding was grown by solid source MBE. The wafer (M354) was processed into a conventional ridge waveguide structure with thin metal top contact. A 2.59 mm long, 18 μm wide laser is mounted epitaxial-side-up on copper submount and wire-bonded for testing. Figure 2.25 (a) is a typical laser spectrum in pulsed mode at 80 K slightly above threshold. The lasing wavelength is $\sim 8.26 \mu\text{m}$, which is slightly larger than the designed value at $\sim 8 \mu\text{m}$. This discrepancy is likely caused by the small deviation of layer thicknesses from the design. Its pulsed L-I-V relations at various temperatures are given in Figure 2.25 (b). The laser emits a peak power of 270 mW at 80 K, and operates up to room temperature with a peak power of 75 mW. This laser also functions in CW mode. A typical CW spectrum is shown in Figure 2.26, which indicates a single longitudinal mode operation. Due to the heating, the CW operation is limited to below heat sink temperature of 150 K.

By comparing the pulsed laser spectrum in Figure 2.25 (a) and CW spectrum in Figure 2.26, it is interesting to see that, for the same heat sink temperature, the laser wavelength in CW is shifted to lower wavenumber compared to the laser wavelength in pulsed mode. This results from a raised laser core temperature in CW mode due to the heating. Additionally, the CW spectrum is single mode, while the pulsed spectrum is multimode. This cleaner spectrum in CW is attributed to mode competition in steady state.

A key parameter to judge the laser performance is the laser threshold. Figure 2.27 shows the laser threshold current density at different heat sink temperatures. For pulsed operation, the threshold increases from 0.85 kA/cm^2 at 80 K to 2.8 kA/cm^2 at 300 K. For

CW operation, it increases from 1.0 kA/cm^2 at 80 K to 2 kA/cm^2 at 150 K . The characteristic temperature T_0 is 179 and 102 K for pulsed mode and CW, respectively.

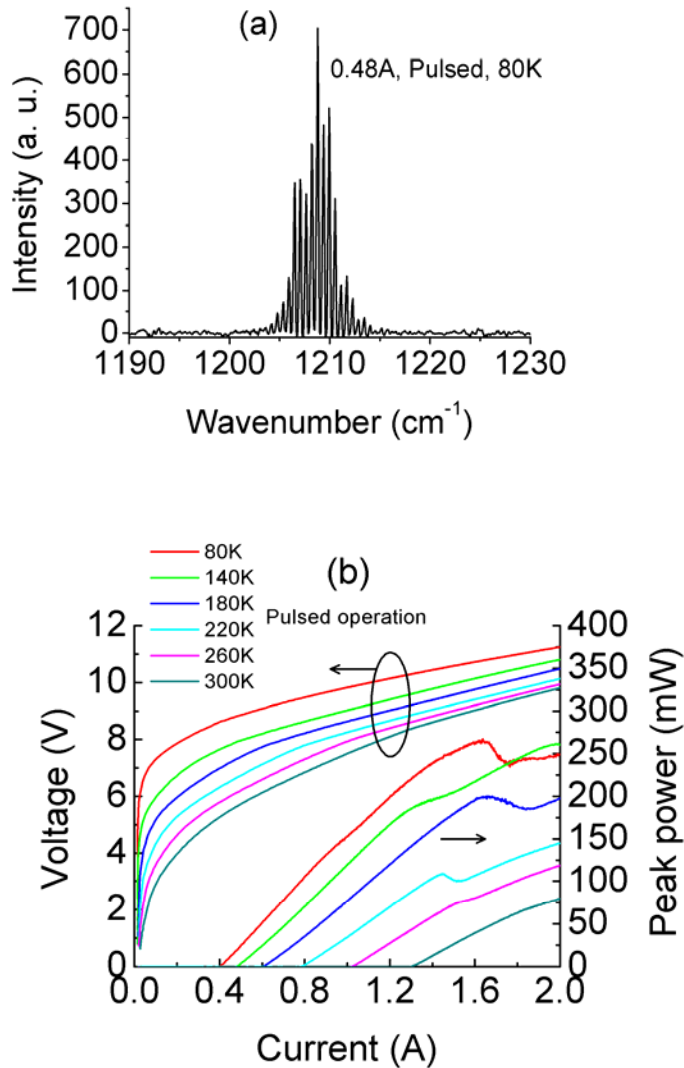


Figure 2.25 (a) Emission spectrum of a 2.59 mm long, $18 \mu\text{m}$ wide, epitaxial-side-up mounted QC laser of wafer M354 operated in pulsed mode at 80 K and 0.48 A . (b) L-I-V curves of the device at different heat sink temperatures in pulsed mode.

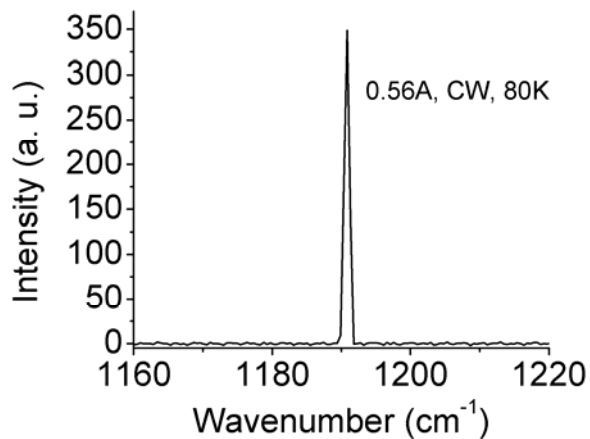


Figure 2.26 Emission spectrum of a 2.59 mm long, 18 μm wide, epitaxial-side-up mounted QC laser of wafer M354 operated in CW mode at 80 K and 0.56 A.

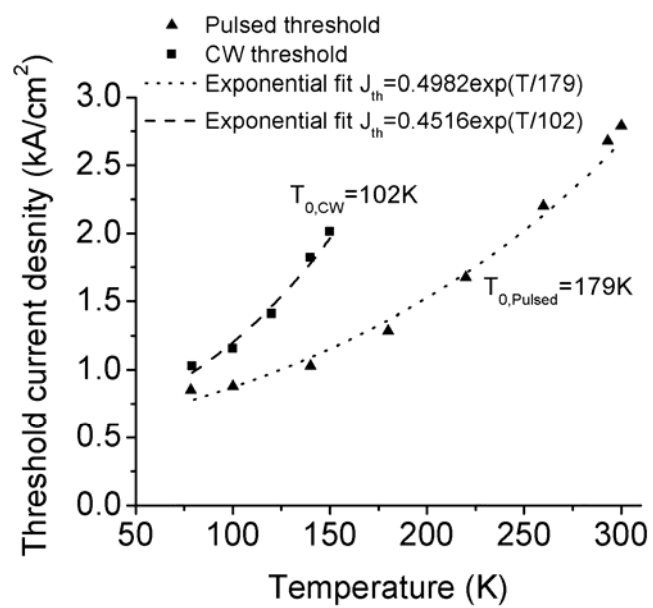


Figure 2.27 Threshold current density versus heat sink temperature of a 2.59 mm long, 18 μm wide, epitaxial-side-up mounted QC laser from wafer M354 in both pulsed mode and CW. Exponential fits result in a characteristic temperature T_0 of 179 and 102 K for pulsed mode and CW, respectively.

A second wafer (D3103) was grown based on the same design using a different solid-source MBE machine. It is lasing at a smaller wavelength of 7.53 μm , as seen from Figure 2.28. The laser threshold for a 2.56 mm long, 12 μm wide device is shown in Figure 2.29. It can be seen that, as compared to M354, D3103 has a lower threshold current density by $\sim 28\%$, and the maximum CW operating temperature increases from the previous 150 K to 200 K. This performance improvement is mainly attributed to a change in the growth condition, as the calibration in layer thickness and doping may vary for different machines. Additionally, the narrower laser ridge width of D3103 (12 μm vs. 18 μm) is a partial reason for the increase in maximum CW operating temperature.

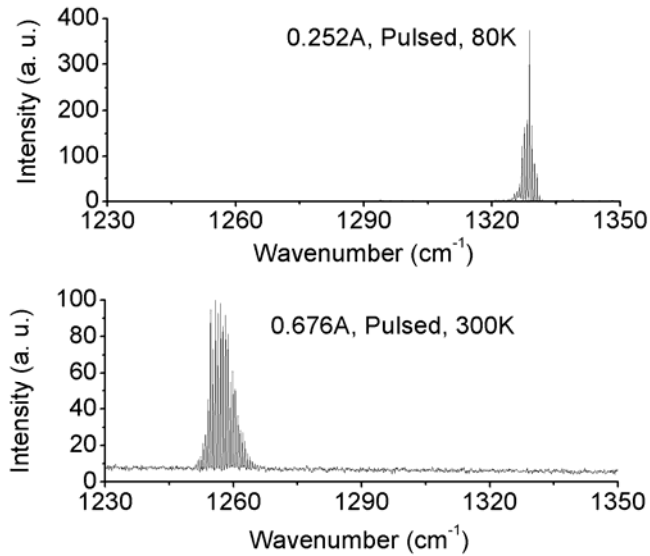


Figure 2.28 Emission spectra of a 2.56 mm long, 12 μm wide, epitaxial-side-up mounted QC laser of wafer D3103 operated in pulsed mode above threshold at 80 and 300 K.

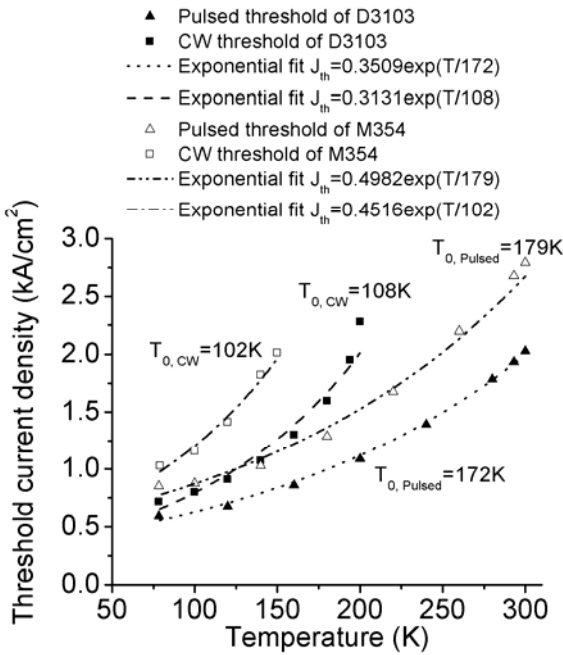


Figure 2.29 Threshold current density versus heat sink temperature of a 2.56 mm long, 12 μm wide, epitaxial-side-up mounted QC laser of wafer D3103 in both pulsed mode and CW. For comparison, the data of a 2.59 mm long, 18 μm wide, epitaxial-side-up mounted QC laser of wafer M354 is also given. Exponential fits result in a characteristic temperature T_0 of 172 and 108 K in pulsed mode and CW for D3103, and 179 and 102 K in pulsed mode and CW for M354, respectively.

For the above described ternary waveguide cladding, ridge waveguide lasers with thin metal top contact, the maximum CW operating temperature is limited at around 200K. To further reduce the laser threshold so as to improve the performance, we use the InP as the waveguide cladding. As mentioned in section 2.2.1, InP is a better material for the waveguide cladding than the ternary $\text{In}_{0.52}\text{Al}_{0.48}\text{As}$ because of a lower refractive index, a lower loss and a higher thermal conductivity. The design using InP as waveguide cladding (wafer labeled as A887a) was grown by MOCVD, which is an industry-preferred growth technique and is promising for mass-production of QC lasers.

A 3.1 mm long, 14 μm wide, epitaxial-side-up mounted, ridge waveguide QC laser with thin metal top contact has been tested, and its threshold current density is shown in Figure 2.30, where the threshold of the ternary waveguide cladding laser D3103 is also given for comparison. The InP waveguide cladding sample A887a has a lower threshold by 10% than that for ternary waveguide cladding sample D3103. Its CW L-I-V curves are shown in Figure 2.31, it functions in CW up to 226 K, which is 26 K improvement as compared to previous ternary waveguide cladding sample D3103 owing to the material advantages of InP. Figure 2.32 shows its emission spectrum in CW mode at 80 K, and the wavelength agrees well with the designed value at 8 μm .

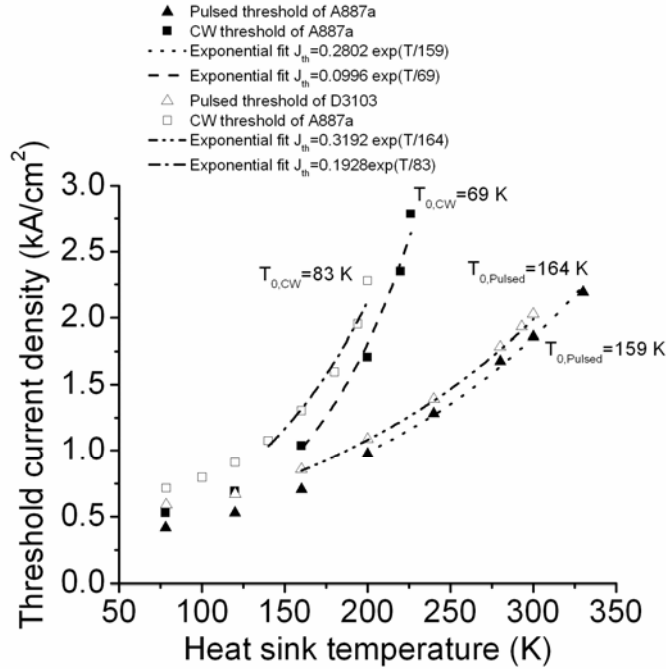


Figure 2.30 Threshold current density versus heat sink temperature of a 3.1 mm long, 14 μm wide, epitaxial-side-up mounted QC laser of InP cladding wafer A887a and a 2.56 mm long, 12 μm wide, epitaxial-side-up mounted QC laser of AlInAs cladding wafer D3103 in both pulsed mode and CW. Exponential fits result in characteristic temperature T_0 of 159 and 69 K in pulsed mode and CW for A887a, and 164 and 83 K in pulsed mode and CW for D3103, respectively.

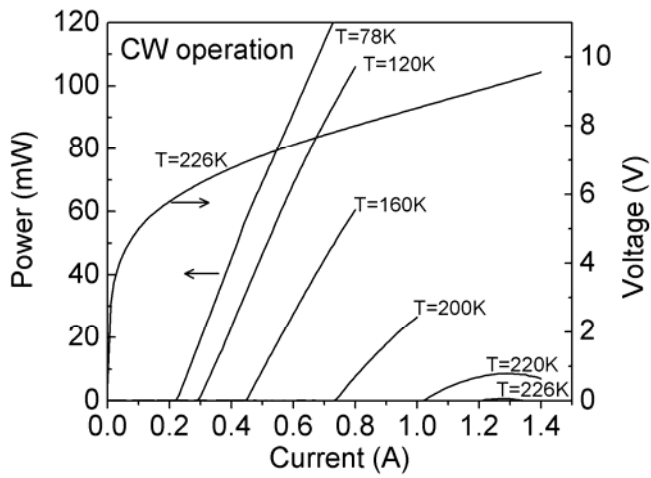


Figure 2.31 CW L-I-V curves for a 3.1 mm long, 14 μm wide, epitaxial-side-up mounted, ridge waveguide QC laser with thin metal top contact from wafer A887a.

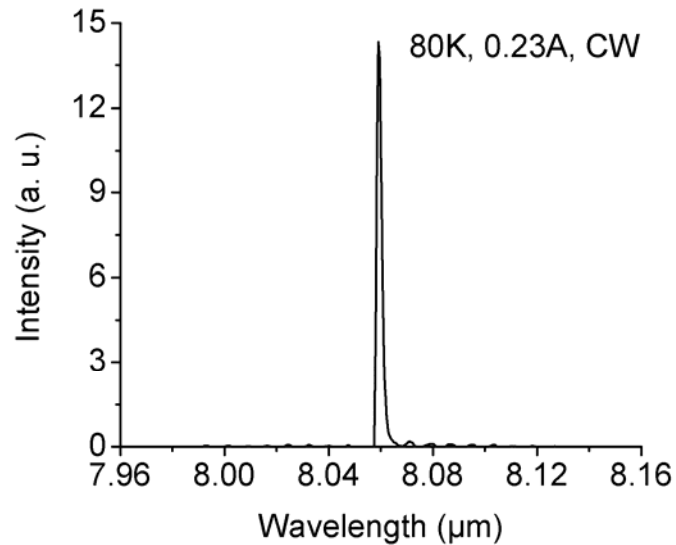


Figure 2.32 Emission spectrum of a 3.1 mm long, 14 μm wide, epitaxial-side-up mounted, ridge waveguide QC laser with thin metal top contact from wafer A887a in CW mode at 80 K and 0.23 A.

This laser represents the best result we obtained for ridge waveguide QC lasers with thin metal top contact. To further improve its performance, an advanced external device packaging and layout is needed, and will be described in the next two sections.

2.5.2 Ridge Waveguide Laser with Thick Metal Top Contact

By using the electroplating technique, a thick gold top contact was first applied to QC lasers to improve the heat dissipation in Ref. [13]. As seen from thermal modeling in section 2.2.2, the thick top metal contact enhances lateral heat transfer through the gold and into the InP surrounding substrate, therefore it is more efficient for heat transfer.

Here, the above $\lambda \approx 8 \mu\text{m}$ QC laser wafer A887a is processed into double-trench, ridge waveguides with $\sim 10 \mu\text{m}$ thick electroplated gold top contact. In addition, a HR coating composed of $\text{SiO}_2/\text{Ti}/\text{Au}/\text{SiO}_2$ (400/15/100/100nm) has been developed and deposited on the laser back facet using e-beam evaporation. This reduction in mirror loss further lowers the laser threshold. Figure 2.33 (a) shows the CW light-current curves of an HR coated, 8 μm wide, 3.5 mm long QC laser at different heat sink temperatures. The voltage-current curve at 300 K is also given. A CW optical output power of 5.3 mW is obtained with a threshold current of 0.73 A (corresponding to $J_{\text{th}} = 2.63 \text{ kA/cm}^2$) at heat sink temperature of 300 K. The typical emission spectrum at 300 K is given by the inset of Figure 2.33 (a). The lasing wavelength is $\sim 8.2 \mu\text{m}$. Figure 2.33 (b) shows the threshold current density of the laser as a function of the heat sink temperature for both pulsed and CW operation. For pulsed operation, the threshold current density increased from 1.21 kA/cm^2 at 240 K to 2.26 kA/cm^2 at 380 K. The CW threshold current density increased from 1.56 kA/cm^2 at 240 K to 3.2 kA/cm^2 at 315 K. The solid lines are the result of exponential fits $J_{\text{th}}=J_0\exp(T/T_0)$. The extracted characteristic temperature T_0 is 217 K and 107 K for pulsed and CW operation, respectively. By comparing the two curves in Figure 2.33 (b), the temperature difference between laser active region and the heat sink can be deduced, and thus the thermal resistance can be calculated by using the

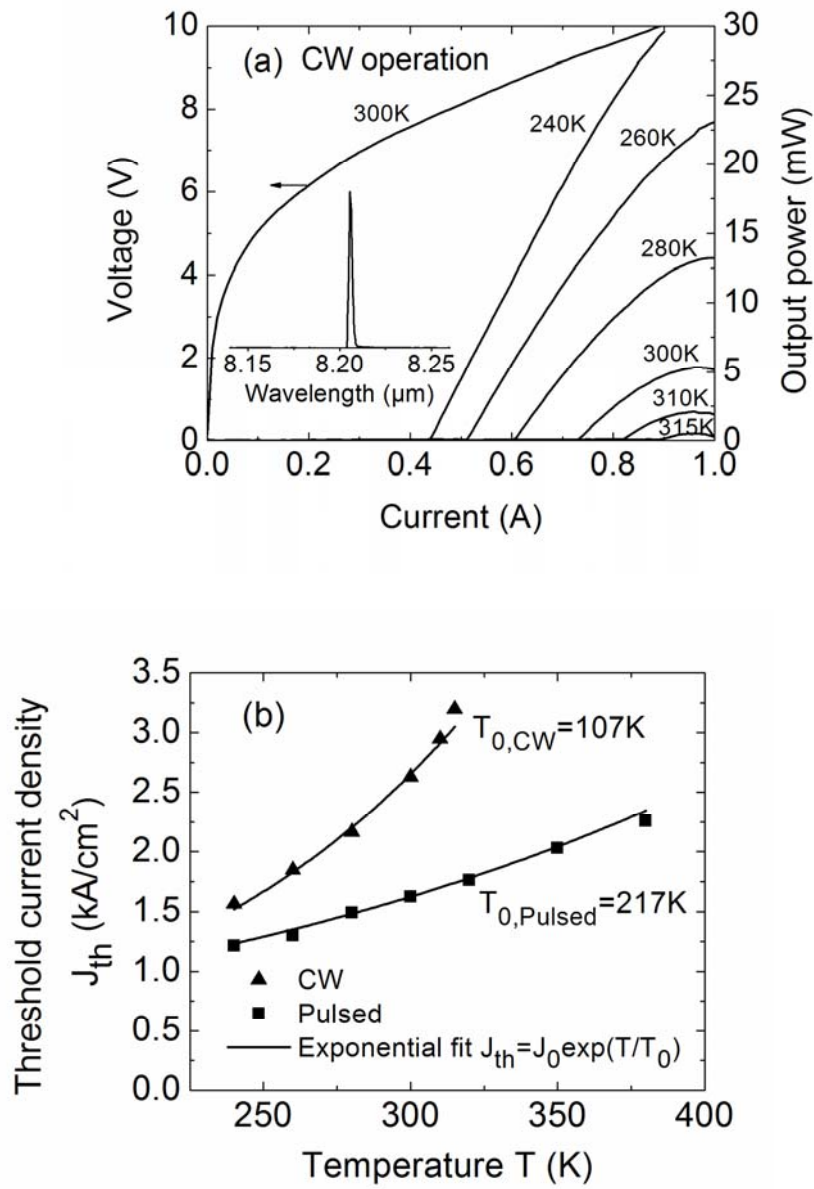


Figure 2.33 (a) CW light-current curves of a HR coated 8 μm wide, 3.5 mm long, epitaxial-side-up mounted, QC laser (A887a) with thick metal top contact at different heat sink temperatures. The voltage-current curve at 300 K is also given. The inset shows the laser spectrum at 300 K and 0.74 A. (b) Threshold current density as a function of the heat sink temperature in pulsed and CW operation (data points). The solid lines are the results of exponential fits $J_{th}=J_0 \exp(T/T_0)$. From 240 to 380 K, $T_0=217$ K for pulsed operation, and from 240 to 315 K, $T_0=107$ K for CW operation.

relation $R_{th} = (T_{act} - T_{sink}) / (I_{th}V_{th})$, where T_{act} is the temperature of active region in CW operation, T_{sink} is the CW heat sink temperature, I_{th} is the threshold current, and V_{th} is the threshold voltage in CW operation. At 300 K, $\Delta T = T_{act} - T_{sink} = 95$ K, $I_{th} = 0.73$ A, $V_{th} = 9.33$ V, the R_{th} is calculated as 13.9 K/W, which is close to the value reported for comparable QC lasers grown by MBE [13].

Here we can see that the thick gold plating and HR coating result in about 90 K improvement in maximum CW operating temperature. This laser represents the first MOCVD-grown room temperature, CW QC laser that does not require lateral InP regrowth [49].

Aside from the MOCVD-grown QC lasers, a second wafer D3109 grown by solid-source MBE with the same design is also fabricated and tested. The CW L-I-V curves are shown in Figure 2.34 (a) for a back facet HR coated, 3 mm long, 6.5 μ m wide, epitaxial-side-up mounted, ridge waveguide QC laser with thick metal top contact. It emits CW optical power of 32 mW at 160 K, and operates up to 280 K. The threshold of this device is given in Figure 2.34 (b). The pulsed threshold current density increased from 1.07 kA/cm² at 160 K to 3.39 kA/cm² at 390 K. The CW threshold current density increased from 1.49 kA/cm² at 160 K to 3.43 kA/cm² at 280 K. The thermal resistance at 280 K is extracted as 15 K/W, which is close to the value for the above discussed MOCVD-grown QC laser. Though this device has a slightly by 35 K lower maximum CW operating temperature, which results from the difference in growth calibration, its overall performance is comparable to the above MOCVD-grown QC laser.

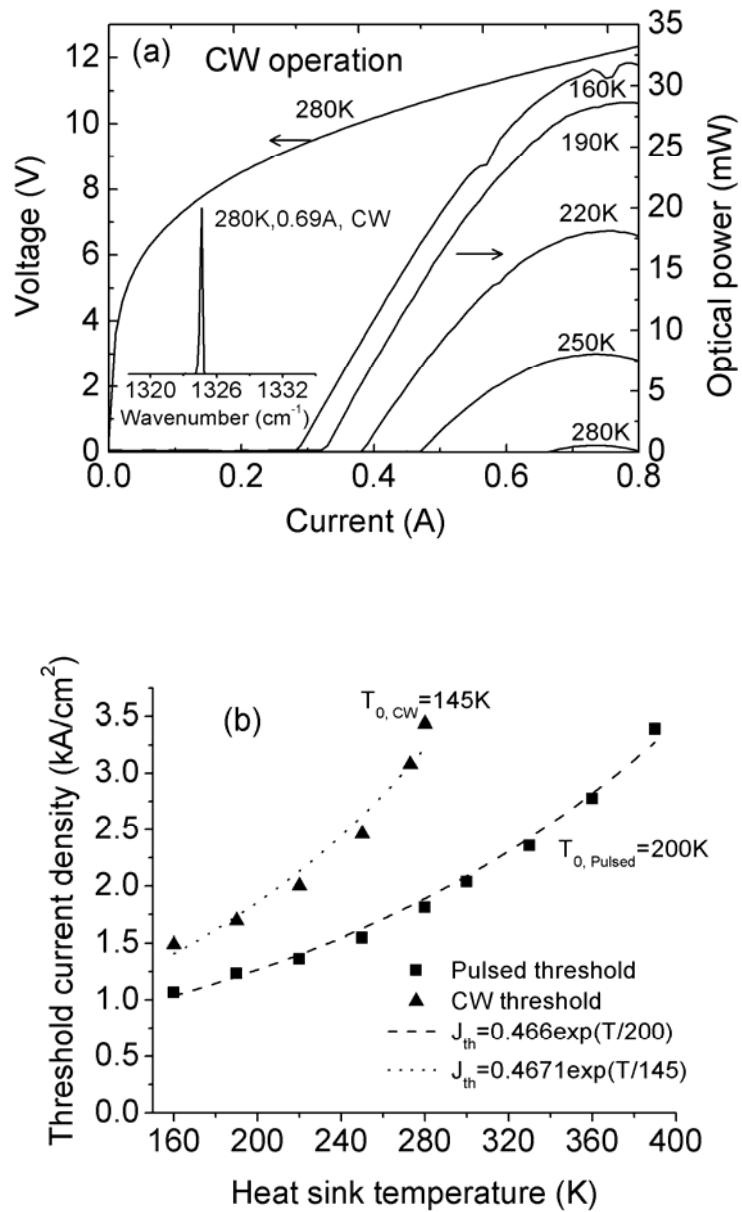
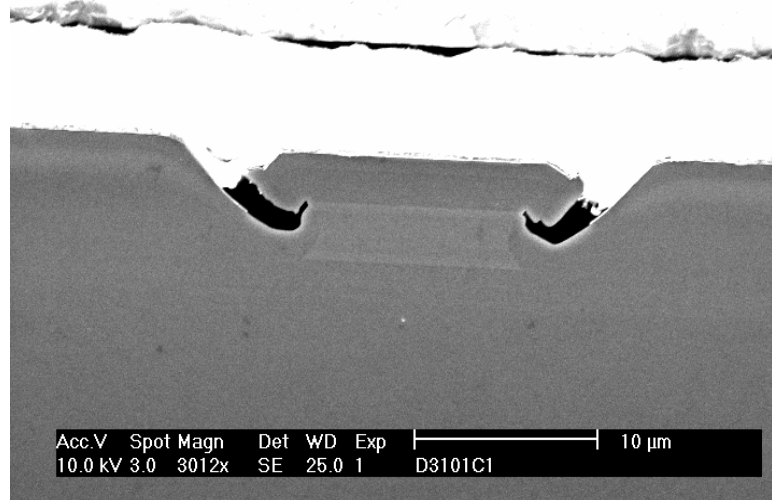


Figure 2.34 (a) CW light-current curves of a HR coated 6.5 μ m wide, 3mm long, epitaxial-side-up mounted, QC laser (D3109) with thick metal top contact at different heat sink temperatures. The voltage-current curve at 280 K is also given. The inset shows the laser spectrum at 280 K and 0.69 A. (b) Threshold current density as a function of the heat sink temperature in pulsed and CW operation (data points). The solid lines are the results of exponential fits $J_{th}=J_0 \exp(T/T_0)$. From 160 to 390 K, $T_0=200$ K for pulsed operation, and from 160 to 280 K, $T_0=145$ K for CW operation.

2.5.3 Buried Heterostructure Laser with Thick Metal Top Contact

An MOCVD-grown wafer 111605_3 (the same design as A887a) has been processed into buried heterostructure lasers with thick metal top contact. Figure 2.35 shows a typical laser facet. There are voids on the two sides of the laser ridge due to a non-optimized lateral InP regrowth condition, where the laser ridge is along [011] direction. These growth voids are due to the different growth directions from the bottom and from the side wall [65]. Actually if the laser ridge is aligned to [011] direction instead of [011], a smooth lateral regrowth can be accomplished.

Nevertheless, an 8 μm wide, 3.5 mm long buried heterostructure laser with growth voids has been tested, and its performance is given in Figure 2.36. A CW optical power of 30 mW is measured at 300 K, which is a significant improvement compared to the previous double-trench ridge waveguide lasers, whose room temperature CW power is only 5.3 mW. In pulsed operation, the threshold current density increases from 1.36 kA/cm² at 240 K to 3.08 kA/cm² at 400 K. The CW threshold current density increased from 1.39 kA/cm² at 240 K to 3.14 kA/cm² at 330 K and characteristic temperatures T_0 of 185 K and 115 K are measured for pulsed and CW operation, respectively. A thermal resistance of R_{th} of 7.1 K/W can be deduced from comparison of the pulsed and CW data, which is nearly half of that for the previous double trench ridge waveguide lasers despite the presence of growth voids. This reduction in thermal resistance is attributed to the enhanced heat transfer of buried heterostructure with thick metal top contact.



AccV Spot Magn Det WD Exp | 10 μm
10.0 kV 3.0 3012x SE 25.0 1 D3101C1

Figure 2.35 SEM image of a facet of a buried heterostructure QC laser at $\lambda \approx 8 \mu\text{m}$ from wafer 111605_3. Voids are created on the two sides of the laser ridge due to a non-optimized lateral InP regrowth condition, where the laser ridge is aligned along [011] direction.

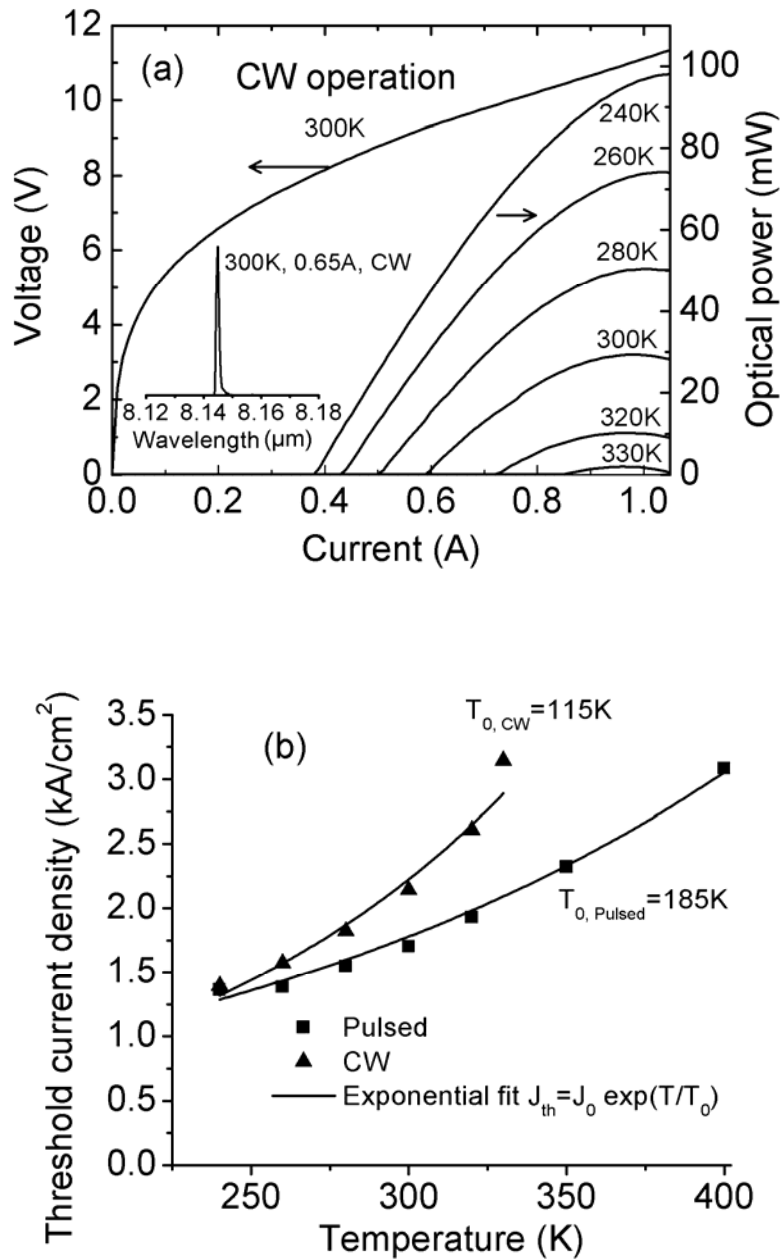


Figure 2.36 (a) CW light-current curves of a HR coated 8 μm wide, 3.5mm long buried heterostructure QC laser (111605_3) with thick metal top contact at different heat sink temperatures. The voltage-current curve at 300 K is also given. The inset shows the laser spectrum at 300 K and 0.65 A. (b) Threshold current density as a function of the heat sink temperature in pulsed and CW operation (data points). The solid lines are the results of exponential fits $J_{\text{th}}=J_0 \exp(T/T_0)$. From 240 to 400 K, $T_0=185$ K for pulsed operation, and from 240 to 330 K, $T_0=115$ K for CW operation.

2.6 Conclusion and Discussion

Table 2.3 Summary of experimental results for QC laser samples at $\lambda \approx 8.2 \mu\text{m}$.

Sample label	Fabrication	J_{th} (300K, pulsed) (kA/cm ²)	$T_{0, \text{Pulsed}}$ (K)	$T_{0, \text{CW}}$ (K)	R_{th} (K/W)	$T_{\text{max,CW}}$ (K)
M329	Thin gold	3.8	118			
D2983	Thin gold	12.16	131			
D2984	Thin gold	9.67	175			
D3028	Thin gold	5.2	172			
D3029	Thin gold	5.8	189			
D3097	Thin gold	2.76	149			156
D3101	Thin gold	2.71	133			150
D3103	Thin gold	2.03	172	108	19.2	200
D3106	Thin gold	no lasing				
D3109	Thick gold	2.03	200	145	15	283
D3110	Thin gold		190	106		179
	Thick gold					220
D3125	Thin gold		188	128		170
M354	Thin gold	2.79	179	102	12.7	150
M356	Thin gold	1.9	204	122	15.7	205
	Thick gold	2.17	200	152		258
M379	Thin gold	1.97	244	139	22.3	193
A887a	Thin gold	1.85	159	69	14.7	226
	Thick gold	1.62	217	107	13.9	315
111605_3	Thick gold					310
	Buried heterostructure	1.7	185	115	7.1	330

The testing results for all $\lambda \approx 8.2 \mu\text{m}$ QC laser samples studied in this Chapter are summarized in Table 2.3. For the samples based on three-well design (D2983, D2984, M329) and those based on non-optimized two phonon resonance design (D3028, D3029), their room temperature pulsed threshold is $\geq 3.8 \text{ kA/cm}^2$. By using an optimized two phonon resonance design, a low loss waveguide design, and thorough thermal modeling, the pulsed threshold is reduced to $\leq 2 \text{ kA/cm}^2$ for samples D3103, D3109, M356, M379, A887a, and 111605_3.

For the lasers with similar dimensions, the conventional ridge waveguide lasers with thin metal top contact (D3103, M379) have a thermal resistance R_{th} of $\sim 20 \text{ K/W}$. By using advanced laser processing, R_{th} is reduced to ~ 14 (A887a) and 7 K/W (111605_3) for double-trench ridge waveguide structure and buried heterostructure with thick metal top contact, respectively.

For the best performing samples A887a and 111605_3, a conventional ridge waveguide laser with thin metal top contact functions with a maximum CW operation temperature of 226 K. Using an improved double-trench ridge waveguide structure with thick metal top contact, the laser functions in CW mode at room temperature with an optical power of 5.3 mW, which represents the first MOCVD-grown room temperature, CW QC laser without lateral regrowth. For a buried heterostructure laser with thick metal top contact, its maximum CW optical power increases to 30 mW at room temperature, and maximum CW operating temperature increases to 330 K. These lasers meet the need for our target trace-gas sensing applications, as a few mW optical power is satisfactory for most of the trace-gas sensing applications based on optical detection schemes, e.g., the technique of quartz-enhanced photoacoustic spectroscopy [66, 67]. With further

improvements such as waveguide design with lower doping levels, smooth InP regrowth without voids and more advanced epitaxial-side-down mounting etc., even higher performance of these lasers is expected.

Finally, it is worthy to note that the thermal model developed in section 2.2 over-predicts the maximum CW operating temperature $T_{\max,CW}$ by approximately 25-50 K for these lasers. This is because the lasers have higher threshold current densities in experiments than those calculated from the design. Actually if the experimental threshold current density J_{th} is used to calculate dissipated heat Q by including the experimental waveguide loss value, then there is a reasonable agreement (~ 10 K difference) between the thermal model and experiments [35].

Chapter 3

Long Wavelength High Performance $\lambda \approx 9.6 - 10.3 \mu\text{m}$ Quantum Cascade Lasers

3.1 Introduction

After achieving room temperature, CW operation at $\lambda \approx 8.2 \mu\text{m}$ as described in previous chapter, here we extend high performance room temperature CW operation of QC lasers to longer wavelength between 9.6 and 10.3 μm within the second atmospheric window for a diisopropyl methyl phosphonate (DIMP) sensor system based on Laser Photoacoustic Spectroscopy (L-PAS). In order to match the absorption peaks of DIMP, QC lasers at several wavelengths between 9.6 and 10.3 μm have been developed. Figure 3.1 shows the absorption spectrum of DIMP in the mid-infrared range, and the red arrows represent the wavelengths of the QC lasers developed in this work.

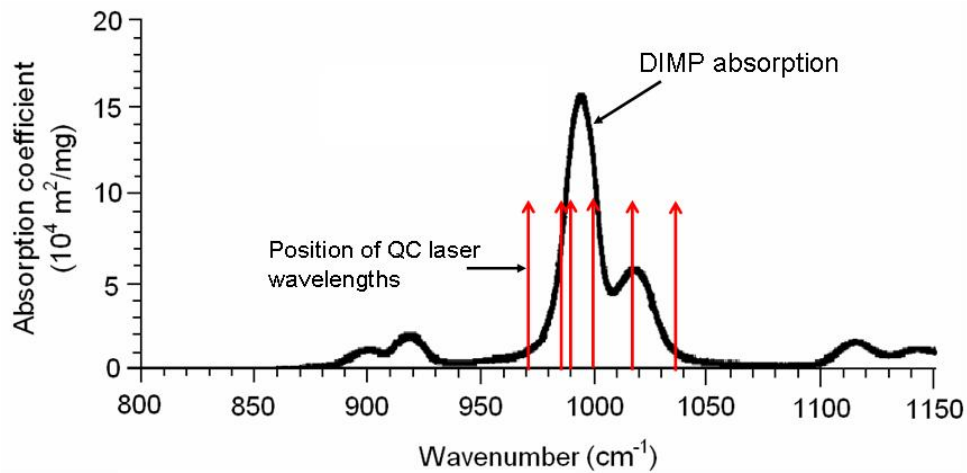


Figure 3.1 Infrared absorption spectrum of DIMP and wavelengths of QC lasers developed in this work. The DIMP absorption spectrum is from Ref. [68].

Using the same design strategies as for $\lambda \approx 8.2$ μm QC lasers, high performance “vertical transition” QC lasers were designed and fabricated at $\lambda \approx 9.6\text{-}10.3$ μm . In addition, in order to explore the advantages or disadvantages of “diagonal transition” QC laser design, which has a longer upper laser level lifetime, two “diagonal transition” lasers were designed and fabricated at $\lambda \approx 9.8$ and 10.1 μm , respectively. Table 3.1 summarizes the samples we studied in this work. We fabricated and tested QC lasers with different ridge widths from seven wafers. In the following sections 3.2-3.5, the most representative and interesting samples are discussed.

Table 3.1 QC laser samples at $\lambda \approx 9.6\text{-}10.3$ μm .

Sample label	Laser design	Wavelength (μm)	Fabrication
M474	Four well, diagonal	9.8	Ridge waveguide
M475	Four well, vertical	10.3	Ridge waveguide
			Buried heterostructure
M479	Four well, diagonal	9.5	Ridge waveguide
M490	Four well, diagonal	10.1	Ridge waveguide
M529	Four well, vertical	10.0	Ridge waveguide
M531	Four well, vertical	10.14	Ridge waveguide
M532	Four well, vertical	9.6	Ridge waveguide

3.2 $\lambda \approx 9.6 \mu\text{m}$ “Vertical Transition” Quantum Cascade Lasers

3.2.1 Laser Design

Here the $\lambda \approx 9.6 \mu\text{m}$ QC laser is designed based on similar strategies as those used in the high performance $\lambda \approx 8.2 \mu\text{m}$ QC laser in Chapter 2. The laser active region is based on a two phonon resonance design with a “vertical transition”, where the upper laser state overlaps with the lower laser state in space. The layer sequence (in Å) of one period of active region and injector is designed as **42/20/7/58/9/59/9/49/26/35/15/34/14/33/16/32/19/31/23/30/25/30**, where $\text{In}_{0.52}\text{Al}_{0.48}\text{As}$ barrier layers are in bold, $\text{In}_{0.53}\text{Ga}_{0.47}\text{As}$ well layers are in roman, and the n-doped ($1 \times 10^{17} \text{ cm}^{-3}$) layers are underlined. The electron energy band diagram is shown in Figure 3.2. The energy of the laser transition between levels 4 and 3 is designed as 135 meV, and levels 1, 2 and 3 are each separated by about one optical phonon energy, through which electrons are depopulated via consecutive two LO phonon resonant emissions and tunneling into the injector. The lifetime of the upper laser level is designed as $\tau_4=1.75 \text{ ps}$, and that of lower laser level is $\tau_3=0.25 \text{ ps}$. The optical dipole matrix element z_{43} is 2.1 nm. The energy separation between level 3 and the ground state of the next down stream injector is optimized as 137 meV to suppress the thermal backfilling effect and at the same time to avoid too high threshold voltage. The FOM of this design is 745 ps Å², higher than that of previous $\lambda \approx 8.2 \mu\text{m}$ QC laser design.

Thirty periods are used as the active core and sandwiched between two 0.5-μm-thick n-doped ($5 \times 10^{16} \text{ cm}^{-3}$) $\text{In}_{0.53}\text{Ga}_{0.47}\text{As}$ layers. The upper cladding layers consists of 3.5- μm-thick n-doped ($1 \times 10^{17} \text{ cm}^{-3}$) InP, followed by a 1.5-μm-thick n⁺-doped ($3 \times 10^{18} \text{ cm}^{-3}$) InP plasmon layer and a highly doped ($2 \times 10^{19} \text{ cm}^{-3}$) InP cap layer. The calculated intensity

profile of the fundamental mode is shown in Figure 3.3. The waveguide loss α_w is calculated as 4.9 cm^{-1} , and the confinement factor Γ is 0.57.

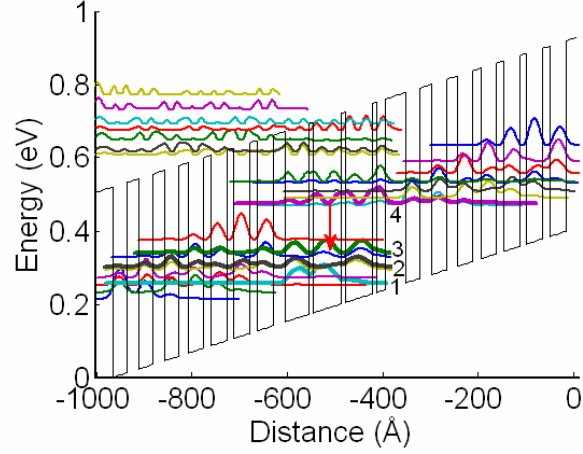


Figure 3.2 Portion of the conduction band diagram and the moduli squared of the relevant wave functions of a $9.6 \mu\text{m}$ QC laser (“vertical transition” design) with a four quantum-well active region based on a two phonon resonance. An electric field of 42 kV/cm is applied. The vertical arrow indicates the laser transition.

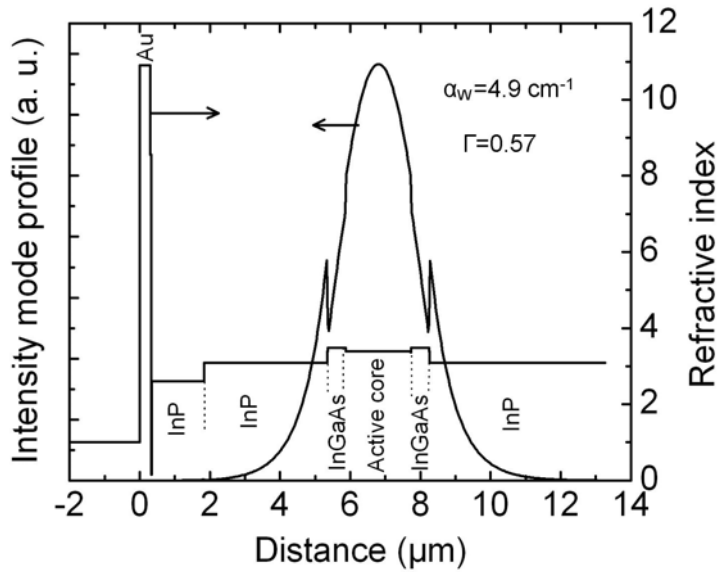


Figure 3.3 Intensity profile of the fundamental TM mode and profile of the real part of the refractive index of the dielectric waveguide calculated at $9.6 \mu\text{m}$.

3.2.2 Ridge Waveguide Laser with Thick Metal Top Contact

The wafer M532 was grown based on the above design. Its active core was grown by solid source MBE, and its top InP cladding layers were grown by MOCVD. The sample was processed into double-trench, ridge waveguide lasers with thick metal top contact using the processing steps described in section 2.3.2. A 3.5 mm long, 17 μm wide, ridge waveguide, back facet HR coated QC laser has been epitaxial-side-up mounted on copper and tested. Figure 3.4 shows the L-I-V curves in CW mode. The device lases at wavelength of 9.6 μm , and functions in CW up to 280 K with an optical power of 3.6 mW.

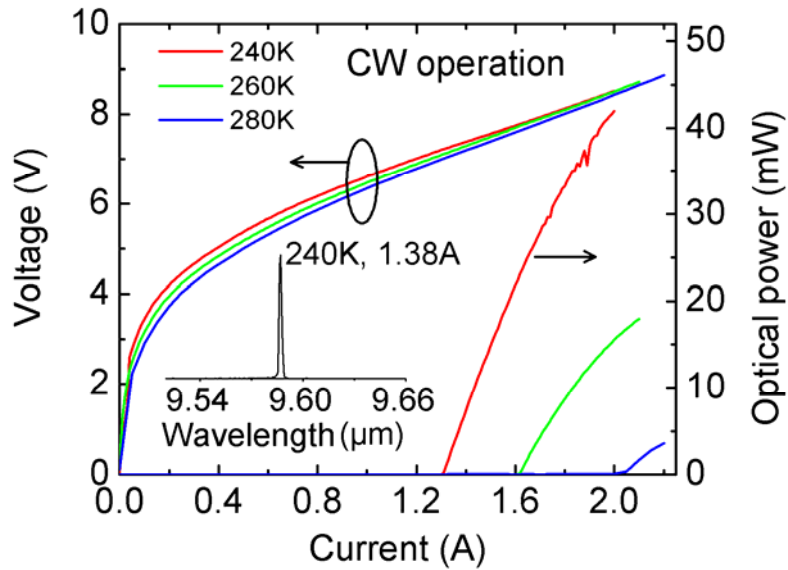


Figure 3.4 CW L-I-V curves of an HR coated, 17 μm wide, 3.5 mm long, ridge waveguide QC laser (M532) with thick metal top contact at different heat sink temperatures. The inset shows the laser spectrum at 240 K and 1.38 A.

3.3 $\lambda \approx 10.3 \mu\text{m}$ “Vertical Transition” Quantum Cascade Lasers

3.3.1 Laser Design

A longer wavelength $\lambda \approx 10.3 \mu\text{m}$ QC laser is designed based on a two phonon resonance design with a vertical transition. The layer sequence (in Å) of one period of active regions and injectors is designed as **40**/19/7/65/**9**/63/**9**/54/**24**/38/**18**/37/**17**/37/**17**/37/19/35/23/34/27/33, where $\text{In}_{0.52}\text{Al}_{0.48}\text{As}$ barrier layers are in bold, $\text{In}_{0.53}\text{Ga}_{0.47}\text{As}$ well layers are in roman, and the n-doped ($1 \times 10^{17} \text{ cm}^{-3}$) layers are underlined. The electron energy band diagram is shown in Figure 3.5. The energy of the laser transition between levels 4 and 3 is designed as 129 meV, and levels 1, 2 and 3 are each separated by about one optical phonon energy, through which electrons are depopulated via two consecutive LO phonon resonant emissions. The lifetime of the upper laser level is designed as $\tau_4=1.69 \text{ ps}$, and that of lower laser level is $\tau_3=0.21 \text{ ps}$. The optical dipole matrix element z_{43} is 2.1 nm. The energy separation between level 3 and the ground state of the next down stream injector is optimized as 147 meV to suppress the thermal backfilling effect and at the same time to avoid too high threshold voltage. The FOM of this design is $712 \text{ ps } \text{\AA}^2$.

Thirty periods are used as the active core and sandwiched between two 0.5-μm-thick n-doped ($5 \times 10^{16} \text{ cm}^{-3}$) $\text{In}_{0.53}\text{Ga}_{0.47}\text{As}$ layers. The upper cladding layers consist of a 3.5-μm-thick n-doped ($1 \times 10^{17} \text{ cm}^{-3}$) InP, followed by a 1.5-μm-thick n⁺-doped ($3 \times 10^{18} \text{ cm}^{-3}$) InP plasmon layer and a highly doped ($2 \times 10^{19} \text{ cm}^{-3}$) InP cap layer. The calculated intensity profile of the fundamental mode is shown in Figure 3.6. The waveguide loss α_w is calculated as 4.9 cm^{-1} , and the confinement factor Γ is 0.62.

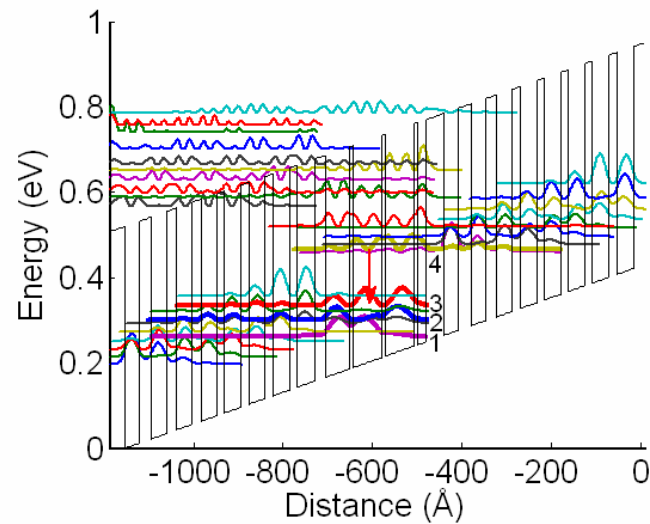


Figure 3.5 Portion of the conduction band diagram and the moduli squared of the relevant wave functions of a $10.3\text{ }\mu\text{m}$ QC laser (“vertical transition” design) with a four quantum-well active region based on a two phonon resonance. An electric field of 37 kV/cm is applied. The arrow indicates the laser transition.

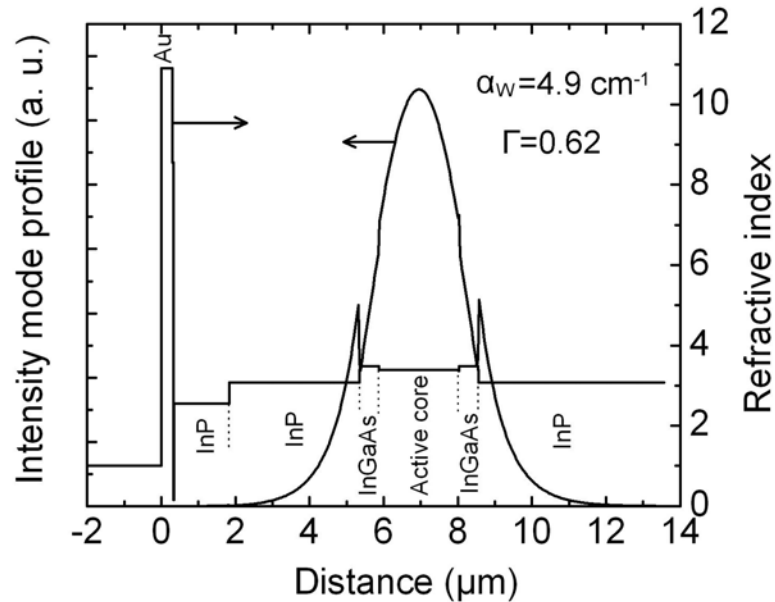


Figure 3.6 Intensity profile of the fundamental TM mode and profile of the real part of the refractive index of the dielectric waveguide calculated at $\lambda \approx 10.3\text{ }\mu\text{m}$.

3.3.2 Ridge Waveguide Laser with Thick Metal Top Contact

Sample M475 based on above design was grown by solid source MBE, and was processed into double-trench, ridge waveguide lasers with thick metal top contact. A 3.5 mm long, 17.7 μm wide, Fabry-Perot laser was epitaxial-side-up mounted on a copper mount and tested. Figure 3.7 shows the laser spectrum in pulsed mode. The lasing wavelength is 9.8 μm at 80 K, and shifts to 10.18 μm at 300 K. Its pulsed L-I-V curves are shown in Figure 3.8. It emits a peak power of 200 mW at 80 K, and 55 mW at 300 K. Figure 3.9 shows the laser spectra in CW operation. It is lasing at 9.8 μm at 80 K and red-shifts to 10.2 μm at 260 K. Figure 3.10 shows the CW L-I-V curves. It emits an optical power of 142 mW at 80 K and operates up to 268 K in CW mode. Figure 3.11 shows the threshold current densities of the device in both pulsed and CW operation. The pulsed threshold current density increases from 0.74 to 2.3 kA/cm^2 when the heat sink temperature increases from 80 to 300 K. The CW threshold current density increases from 0.77 kA/cm^2 at 80 K to 3.39 kA/cm^2 at 268 K.

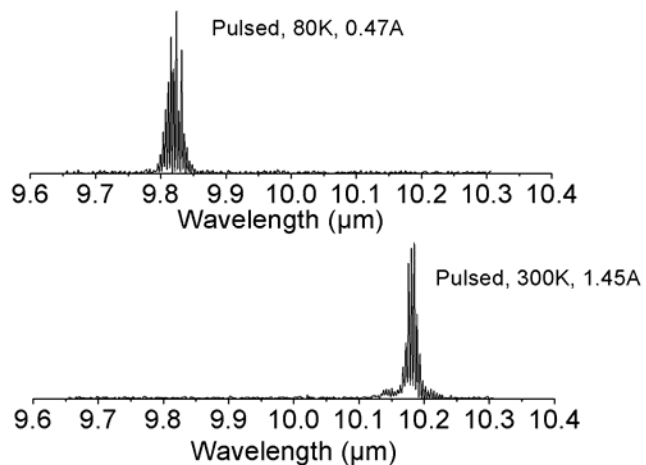


Figure 3.7 Pulsed spectra of a Fabry-Perot, 3.5 mm long, 17.7 μm wide, epitaxial-side-up mounted, ridge waveguide QC laser with thick metal top contact at $\lambda \approx 10.3 \mu\text{m}$ (M475).

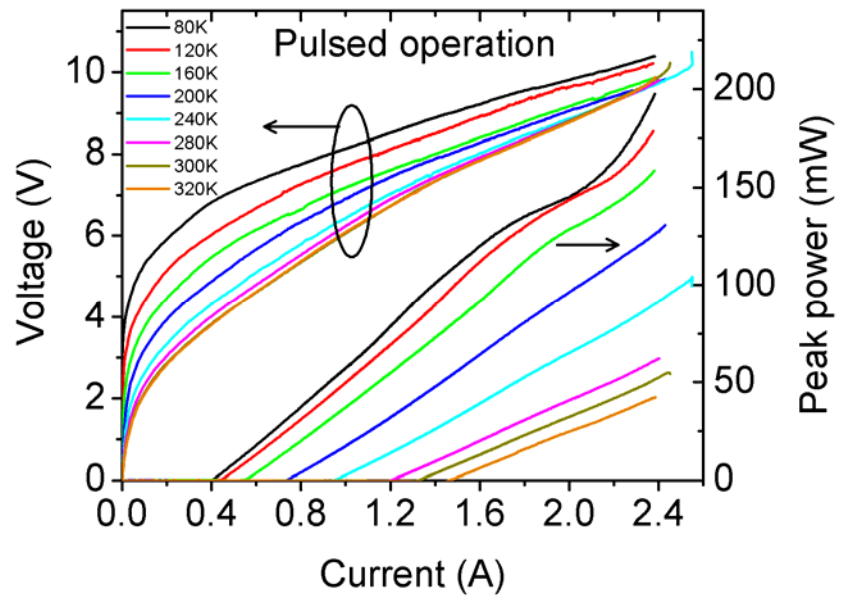


Figure 3.8 Pulsed L-I-V curves of a Fabry-Perot, 3.5 mm long, 17.7 μm wide, ridge waveguide QC laser with thick metal top contact (M475) at different heat sink temperatures.

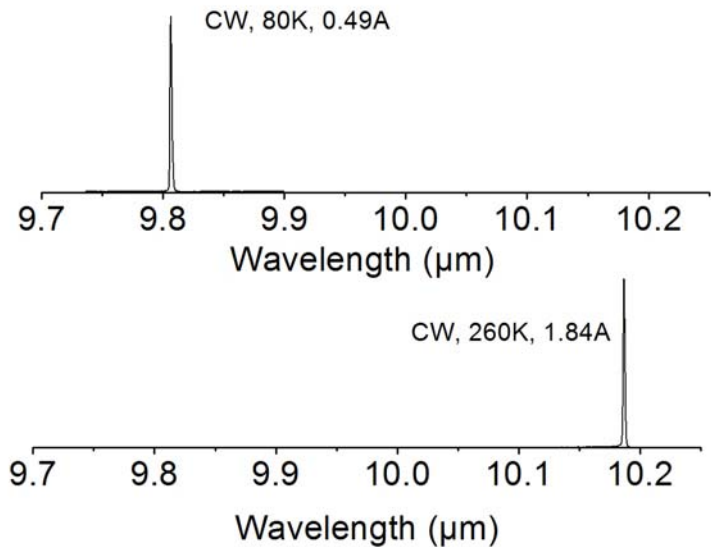


Figure 3.9 CW spectra of a Fabry-Perot, 3.5 mm long, 17.7 μm wide, epitaxial-side-up mounted, ridge waveguide QC laser with thick metal top contact at $\lambda \approx 10.3 \mu\text{m}$ (M475).

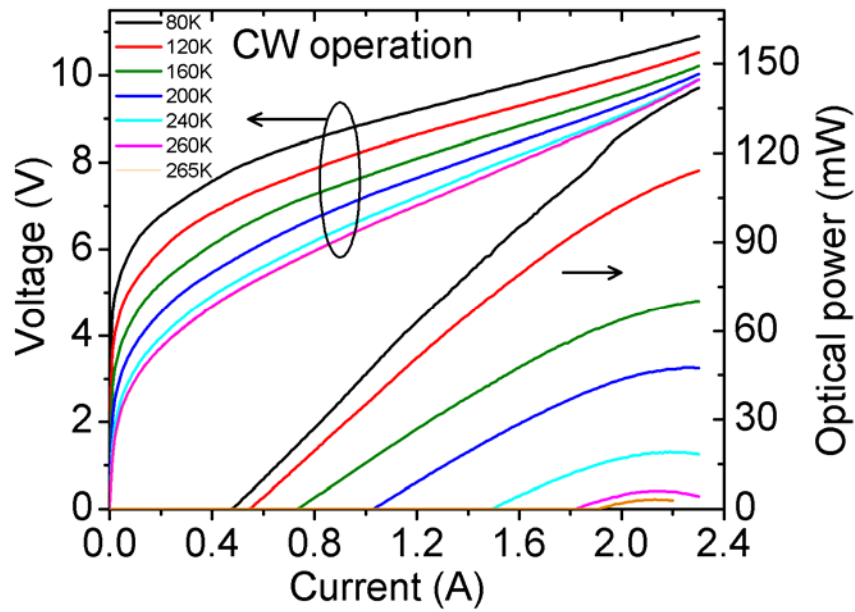


Figure 3.10 CW L-I-V curves of a Fabry-Perot, 3.5 mm long, 17.7 μm wide, ridge waveguide QC laser with thick metal top contact (M475) at different heat sink temperatures.

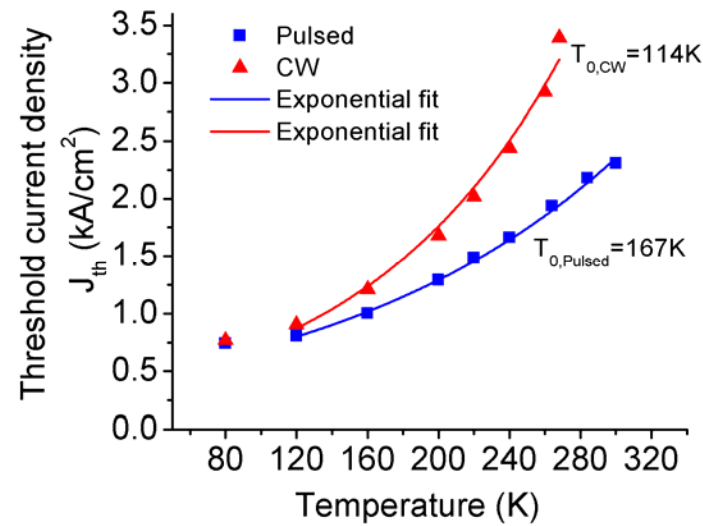


Figure 3.11 Threshold current density versus heat sink temperature for a Fabry-Perot, 3.5 mm long, 17.7 μm wide, ridge waveguide QC laser with thick metal top contact (M475) in pulsed and CW operation (data points). The solid lines are the results of exponential fits $J_{\text{th}}=J_0 \exp(T/T_0)$. From 80 K to 320 K, $T_0=167$ K for pulsed operation, and from 80 K to 268 K, $T_0=114$ K for CW operation.

A next step for increasing the maximum CW operation temperature would be decreasing the laser ridge width, since narrower laser ridge leads to less heat-generation. However, as contrary to the $\lambda \approx 6 \mu\text{m}$ QC lasers in Ref. [69], for devices at this longer wavelength, their performance gets worse when the laser ridge width decreases. Figure 3.12 shows the measured threshold current densities for three 3.5 mm long lasers with different ridge width of 18, 15.6, 12.2 μm . When the laser ridge width decreases from 18 μm to 12.2 μm , its pulsed threshold increases by 22%, and the maximum CW temperature decreases from 268 K to 243 K. This phenomenon cannot be explained by the ridge width dependent free carrier absorption. As shown in Figure 3.13, by considering only the free carrier absorption, the calculated 3 dimensional waveguide loss using commercial software BeamProp [70] doesn't obviously increase until the laser ridge width is less than 11 μm .

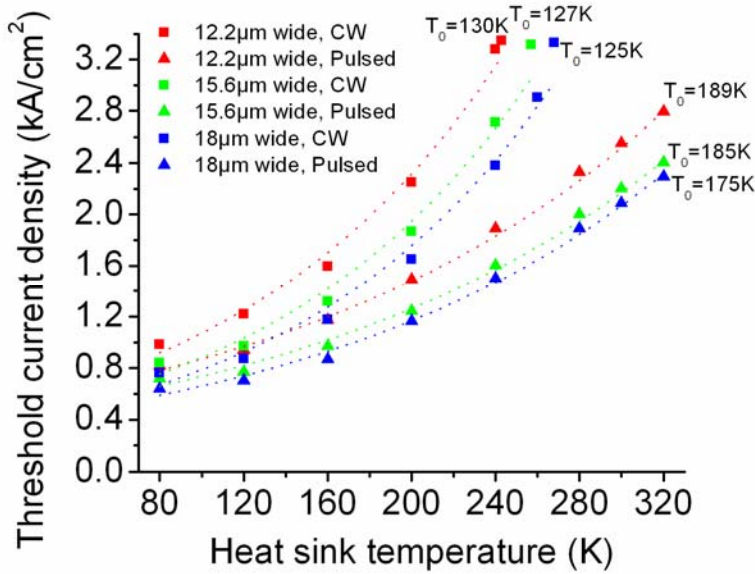


Figure 3.12 Threshold current density as a function of the heat sink temperature in pulsed and CW operation for three 3.5mm long lasers (M475) with different ridge width of 18, 15.6, 12.2 μm . The dotted lines are the results of exponential fits $J_{\text{th}}=J_0 \exp(T/T_0)$.

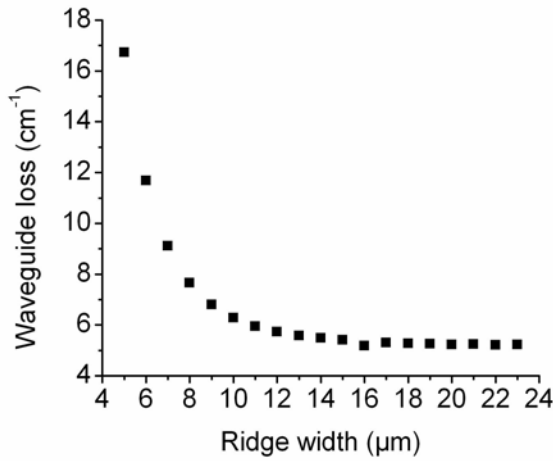


Figure 3.13 Calculated waveguide loss resulting from free carrier absorption versus laser ridge width for double-trench ridge waveguide QC lasers with thick metal top contact at $\lambda \approx 10.3 \mu\text{m}$ (M475).

3.3.3 Buried Heterostructure Laser with Thick Metal Top Contact

The next step to increase the laser performance is to use a buried heterostructure, since it has the advantages of a better thermal conductivity and a lower waveguide loss especially for narrow laser ridge.

The wafer M475 has also been processed into buried heterostructure lasers using the lateral InP regrowth technique as described in section 2.3.3. A 3.5 mm long, 15.4 μm wide, buried heterostructure QC laser was epitaxial-side-up mounted on a copper mount and tested. Its performance is shown in Figure 3.14, where the threshold of a double-trench ridge waveguide laser is also given for comparison. It is seen that the lateral InP regrowth and back facet HR coating each lowers the laser threshold. From the maximum CW threshold data, we can see that the InP lateral regrowth and HR back facet coating each gives 25 and 19 K improvement in maximum CW operation temperature, respectively, and a 3.5 mm long, 15.4 μm wide, HR back facet coated, buried

heterostructure laser functions in CW up to room temperature. Its CW L-I-V curves are shown in Figure 3.15. It emits a CW optical power of 66 mW at 240 K, and the output power drops to 1 mW at 300 K. The lasing wavelength is 10.3 μm at room temperature as shown in the inset of Figure 3.15.

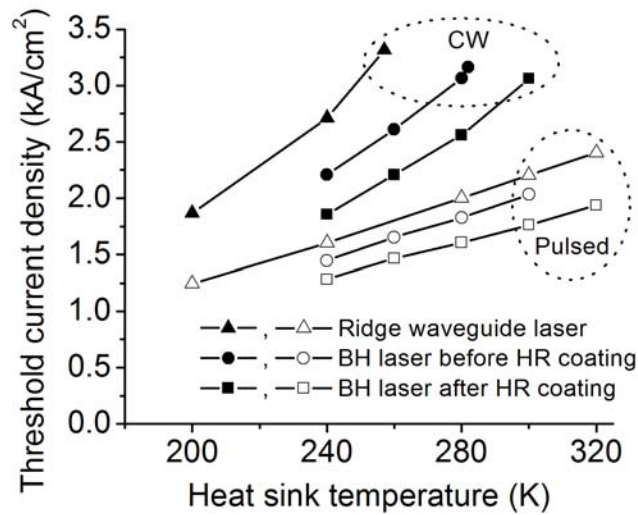


Figure 3.14 Pulsed and CW threshold current densities versus heat sink temperature of a 3.5 mm long, 15.6 μm wide, ridge waveguide QC laser with thick metal top contact at $\lambda \approx 10.3 \mu\text{m}$, and of a 3.5 mm long, 15.4 μm wide, buried heterostructure QC laser from the same wafer (M475) before and after HR coating on its back facet.

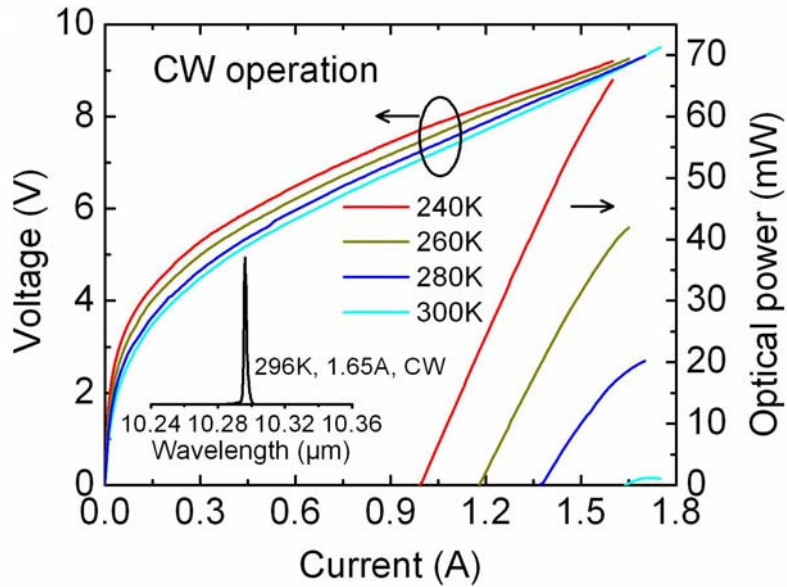


Figure 3.15 CW L-I-V curves at different heat sink temperatures for a back facet HR coated, 3.5 mm long, 15.4 μm wide, epitaxial-side-up mounted, buried heterostructure QC laser (M475). The inset shows the typical laser spectrum at room temperature.

3.4 $\lambda \approx 9.8 \mu\text{m}$ “Diagonal Transition” Quantum Cascade Lasers

The previous samples were designed as “vertical transition” QC lasers with a two phonon resonance scheme for carrier depopulation. Here a $\lambda \approx 9.8 \mu\text{m}$ laser is designed as “diagonal transition” QC laser, where the two lasing states are separated in space. In this design, there is less overlap between upper and lower lasing states, thus resulting in a smaller dipole matrix element. However, it has the advantage of a longer upper laser level lifetime, which could be potentially utilized to make a better laser.

3.4.1 Laser Design

The energy diagram of the “diagonal transition” design is shown in Figure 3.16. The layer sequence (in Å) of one period of active region and injector is designed as 44/26/15/

55/12/53/12/43/**25**/34/14/33/13/32/**15**/31/**19**/29/**23**/29, where $\text{In}_{0.52}\text{Al}_{0.48}\text{As}$ barrier layers are in bold, $\text{In}_{0.53}\text{Ga}_{0.47}\text{As}$ well layers are in roman, and the n-doped ($1 \times 10^{17} \text{ cm}^{-3}$) layers are underlined. The laser transition is between levels 4 and 3, and its energy is designed as 130.6 meV. The optical dipole matrix element is 14 Å and the upper laser lifetime is 3.62 ps, which is much larger than that for previous vertical transition lasers. A two phonon resonance scheme composed of levels 1, 2 and 3 is still kept for fast carrier depopulation. The lower laser lifetime is calculated as 0.22 ps. A large energy spacing of 139 meV is designed between the lower laser level and the ground state of the next down stream injector for suppressing thermal backfilling. The FOM of this design is 695 ps Å².

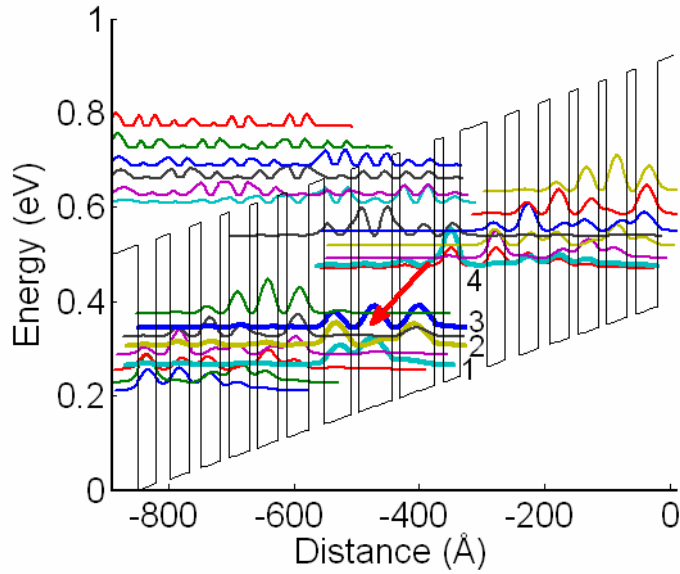


Figure 3.16 Portion of the conduction band diagram and the moduli squared of the relevant wave functions of a $\lambda \approx 9.8 \mu\text{m}$ QC laser designed with a “diagonal transition” and a two phonon resonance scheme. An electric field of 47 kV/cm is applied. The arrow indicates the laser transition.

Thirty seven periods are used as the active core and sandwiched between two 0.5-μm-thick n-doped ($5 \times 10^{16} \text{ cm}^{-3}$) $\text{In}_{0.53}\text{Ga}_{0.47}\text{As}$ layers. The upper cladding layers consist of a 3.5-μm-thick n-doped ($1 \times 10^{17} \text{ cm}^{-3}$) InP, followed by a 1.5-μm-thick n⁺-doped (3×10^{18}

cm^{-3}) InP plasmon layer and a highly doped ($2 \times 10^{19} \text{ cm}^{-3}$) InP cap layer. The calculated intensity profile of the fundamental mode is shown in Figure 3.17. The waveguide loss α_w is calculated as 5 cm^{-1} , and the confinement factor Γ is 0.6.

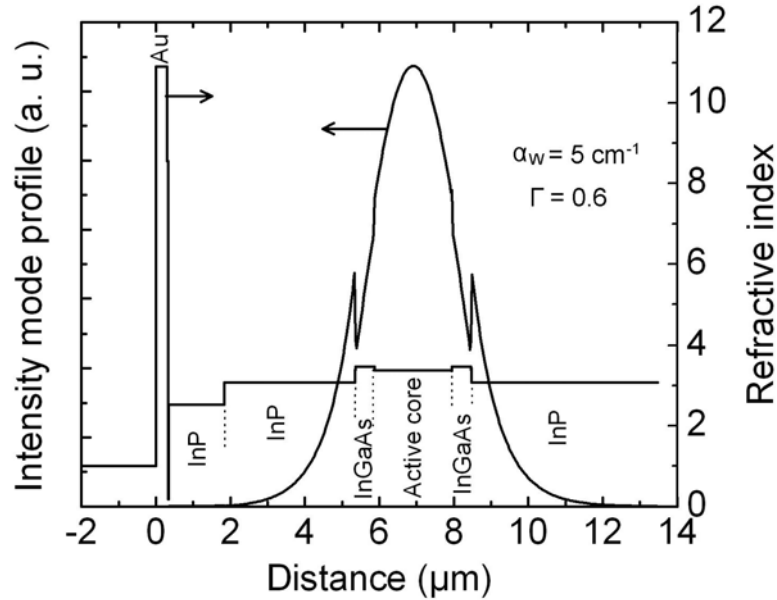


Figure 3.17 Intensity profile of the fundamental TM mode and profile of the real part of the refractive index of the dielectric waveguide calculated at $\lambda \approx 9.8 \mu\text{m}$.

3.4.2 Ridge Waveguide Laser with Thick Metal Top Contact

The sample M474 based on the above design is processed into ridge waveguide lasers with thick gold top contact. Figure 3.18 shows the testing results of a 3.5 mm long, 10 μm wide laser in CW mode. It is lasing at 9.83 μm , and functions in CW up to 200 K. This performance is worse than that of previous “vertical transition” laser M475 at similar wavelength. Figure 3.19 shows the threshold current of this device in both pulsed and CW modes. This “diagonal transition” laser has a larger T_0 (250 K vs. 189 K), but also a higher threshold current density compared to the “vertical transition” laser M475.

Figure 3.20 shows the threshold of three “diagonal transition” M474 lasers with different ridge widths. Similar to the “vertical transition” M475 lasers, the threshold increases when the ridge width decreases from 18.5 μm to 12.5 μm , resulting in a lower maximum CW operation temperature for narrower laser ridges.

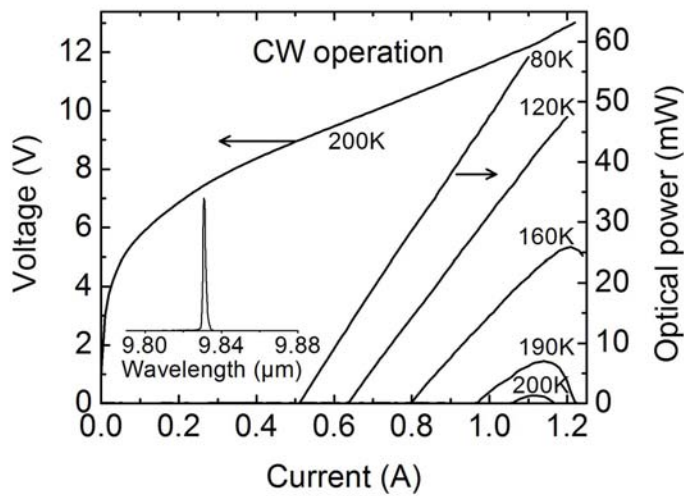


Figure 3.18 CW L-I-V curves for a 3.5 mm long, 10 μm wide, “diagonal transition” QC laser at $\lambda \approx 9.8 \mu\text{m}$ (M474). The inset shows a laser spectrum at 80 K and 0.55 A.

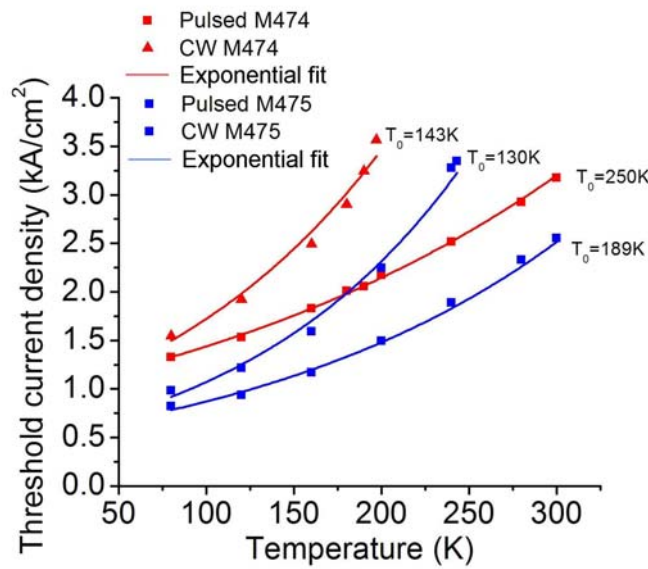


Figure 3.19 Threshold current density versus heat sink temperature of a 3.5 mm long, 12.5 μm wide, “diagonal transition” QC laser of M474 and a 3.5 mm long, 12.2 μm wide, “vertical transition” QC laser of M475 in both pulsed mode and CW.

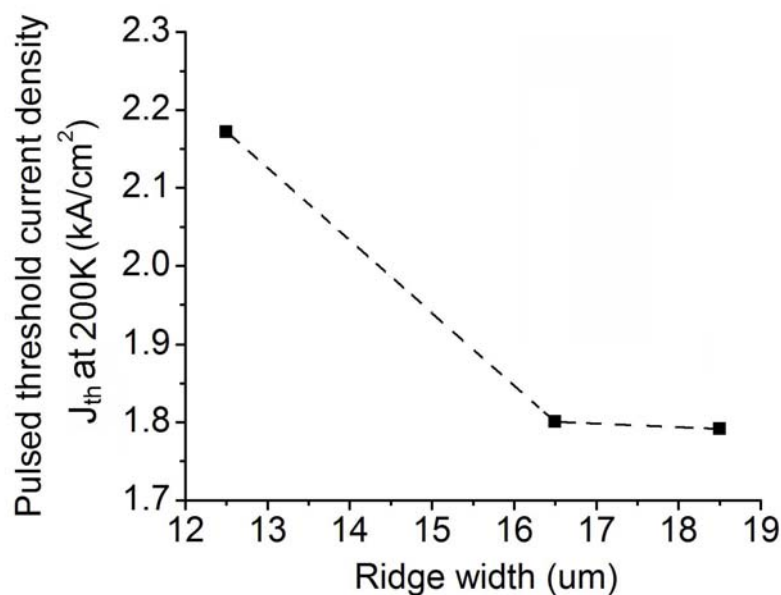


Figure 3.20 Pulsed threshold current density measured at 200 K heat sink temperature for three 3.5 mm long QC lasers of M474 with different ridge width of 18.5, 16.5, 12.5 μm . Dashed line is guide to eye.

3.5 $\lambda \approx 10.1 \mu\text{m}$ “Diagonal Transition” Quantum Cascade Lasers

3.5.1 Laser Design

Using the similar “diagonal transition” design of M474, a second longer wavelength QC laser (M490) at $\lambda \approx 10.1 \mu\text{m}$ is designed and grown. Its energy diagram is shown in Figure 3.21. The layer sequence (in Å) of one period of active region and injector is designed as **44/27/16/56/11/54/14/43/26/34/15/33/14/33/16/32/20/30/24/30**, where $\text{In}_{0.52}\text{Al}_{0.48}\text{As}$ barrier layers are in bold, $\text{In}_{0.53}\text{Ga}_{0.47}\text{As}$ well layers are in roman, and the n-doped ($1 \times 10^{17} \text{ cm}^{-3}$) layers are underlined. The laser transition is between levels 4 and 3, and its energy is designed as 123.2 meV. The dipole matrix element is 12.43 Å and the upper laser lifetime is 4.8 ps, which is much larger than that for previous vertical transition lasers. A two phonon resonance scheme is used for fast carrier depopulation. The lower laser lifetime is calculated as 0.2 ps. A large energy spacing of 126 meV is designed between the lower laser level and the ground state of the next down stream injector for suppressing thermal backfilling. The FOM of this design is 723 ps Å².

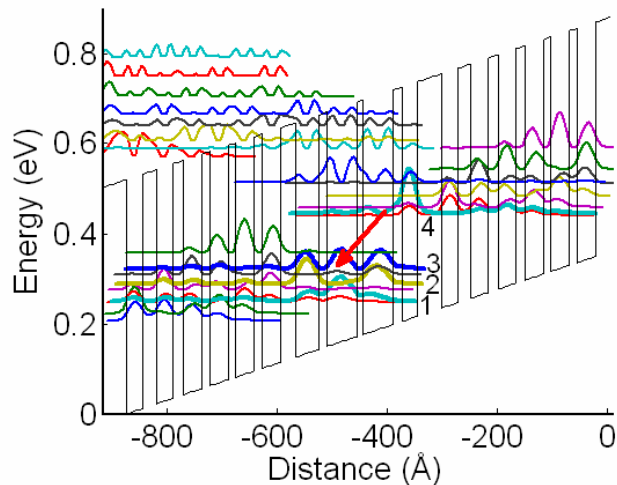


Figure 3.21 A portion of the conduction band diagram and the moduli squared of the relevant wave functions of a $\lambda \approx 10.1 \mu\text{m}$ QC laser designed as diagonal transition with a two phonon resonance scheme. An electric field of 41 kV/cm is applied. The arrow indicates the laser transition.

Thirty five periods are used as the active core and sandwiched between two 0.5- μm -thick n-doped ($5\times 10^{16} \text{ cm}^{-3}$) In_{0.53}Ga_{0.47}As layers. The upper cladding layers consists of 4.1- μm -thick n-doped ($1\times 10^{17} \text{ cm}^{-3}$) InP, followed by a 0.9- μm -thick n⁺-doped ($3\times 10^{18} \text{ cm}^{-3}$) InP plasmon layer and a highly doped ($2\times 10^{19} \text{ cm}^{-3}$) InP cap layer. The calculated intensity profile of the fundamental mode is shown in Figure 3.22. The waveguide loss α_w is calculated as 6 cm^{-1} , and the confinement factor Γ is 0.57.

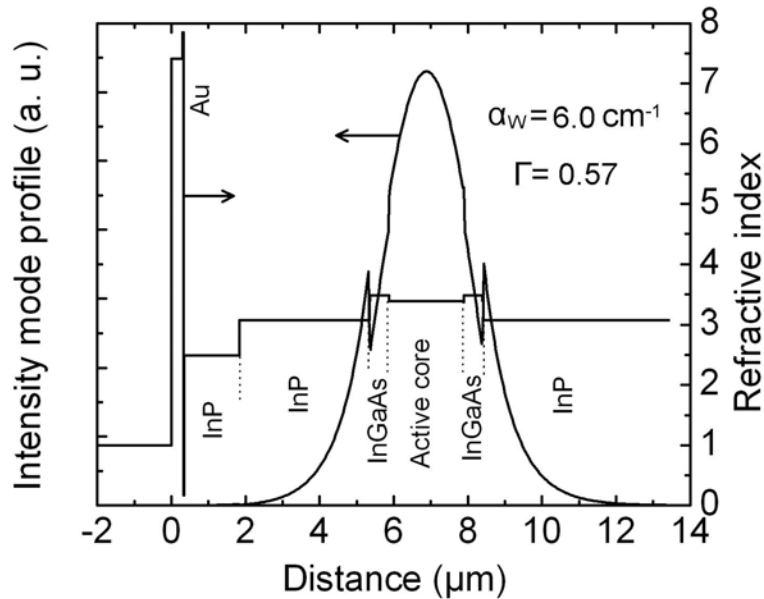


Figure 3.22 Intensity profile of the fundamental TM mode and profile of the real part of the refractive index of the dielectric waveguide calculated at $\lambda \approx 10.1 \mu\text{m}$.

3.5.2 Ridge Waveguide Laser with Thick Metal Top Contact

Figure 3.23 shows the spectrum of a 3.5 mm long, 16 μm wide laser in CW mode. The lasing wavelength is 10.1 μm at 80 K. Its CW L-I-V curves at different heat sink temperatures are given in Figure 3.24. The maximum CW operating temperature is 238 K, which is better than previous sample M474 due to a larger gain design, however, it is still

not as good as “vertical transition” lasers at similar wavelength such as M475. The threshold current density of this device in both pulsed and CW mode is shown in Figure 3.25. The pulsed threshold current density increases from 0.97 kA/cm^2 at 80 K to 2.36 kA/cm^2 at 300 K, and the CW threshold current density increases from 1.22 kA/cm^2 at 80 K to 3.3 kA/cm^2 at 238 K. The characteristic temperature T_0 is 244 and 158 K for pulsed and CW mode, respectively, which are larger than that for “vertical transition” lasers owing to a larger upper laser level lifetime.

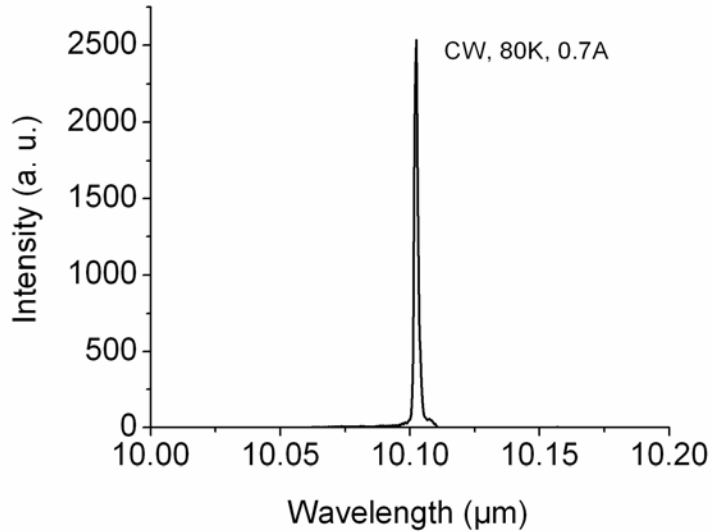


Figure 3.23 Spectrum of a 3.5 mm long, $16 \mu\text{m}$ wide, ridge waveguide QC laser with thick metal top contact (M490) in CW mode at 80K.

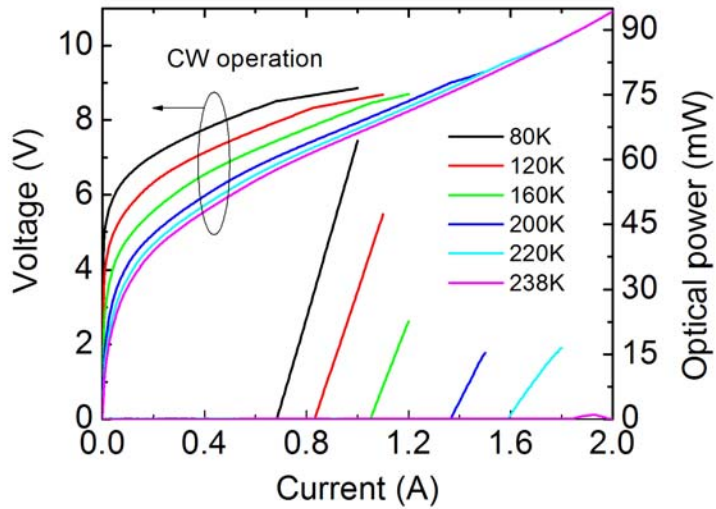


Figure 3.24 CW L-I-V curves for a 3.5 mm long, 16 μm wide, ridge waveguide QC laser with thick metal top contact at $\lambda \approx 10.1 \mu\text{m}$ (M490).

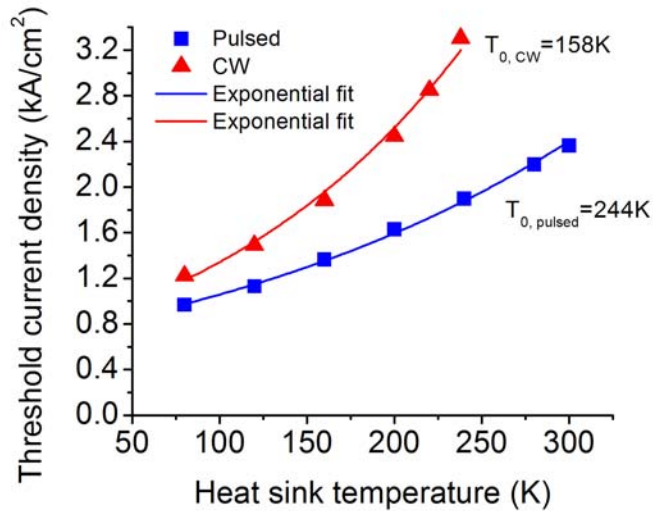


Figure 3.25 Threshold current density versus heat sink temperature of a 3.5 mm long, 16 μm wide, ridge waveguide QC laser with thick metal top contact (M490) in both pulsed and CW modes.

3.6 Conclusion and Discussion

The testing results for all samples studied in this Chapter are summarized in Table 3.2. For samples M475, M529, M531, M532, which use the similar design strategies

developed for the $\lambda \approx 8.2 \mu\text{m}$ QC lasers described in Chapter 2, room temperature (275-301 K) CW operation has been realized at wavelengths between 9.6 and 10.3 μm , which coincide with the absorption peaks of DIMP and are suitable light sources for DIMP sensor systems based on Laser Photoacoustic Spectroscopy (L-PAS) technique.

In addition, in order to explore the advantage of diagonal transition, i.e. a longer upper laser level lifetime, two “diagonal transition” lasers M474 and M490 were designed and realized for wavelengths at 9.8 and 10.1 μm . These diagonal transition lasers have a larger T_0 owing to a longer upper laser level lifetime, but also higher threshold and lower maximum CW operating temperature compared to the “vertical transition” lasers at

Table 3.2 Summary of experimental results for QC laser samples at $\lambda \approx 9.6\text{-}10.3 \mu\text{m}$.

Sample label	Laser design	Fabrication	Pulsed J_{th} @300 K (kA/cm ²)	$T_{\text{max,CW}}$ (K)	$T_{0,\text{Pulsed}}$ (K)	$T_{0,\text{CW}}$ (K)	R _{th} (K/W)
M474	Four well, diagonal	Ridge waveguide	3.18	210	250	143	7.3
M475	Four well, vertical	Ridge waveguide	2.03	268	167	114	5.6
		Buried heterostructure	1.76	301	213	120	7.7
M479	Four well, diagonal	Ridge waveguide	no lasing				
M490	Four well, diagonal	Ridge waveguide	2.36	238	244	158	7.9
M529	Four well, vertical	Ridge waveguide	1.69	288			
M531	Four well, vertical	Ridge waveguide	1.92	275			
M532	Four well, vertical	Ridge waveguide	1.76	283			

similar wavelengths. As discussed later in Chapter 4, this worse performance of “diagonal transition” lasers is attributed to their lower injection efficiency and anomalously high waveguide loss.

For both the vertical and diagonal transition, ridge waveguide QC lasers at these long wavelengths, a strong ridge-width dependence of laser threshold was observed, i.e. when the ridge-width decreases from $\sim 18 \mu\text{m}$ to $\sim 12 \mu\text{m}$, the laser threshold current density increases by $\sim 20\%$, which results in a decrease in maximum CW operating temperature. This ridge-width dependence requires a wider laser ridge-width for obtaining a low laser threshold, thus limits the CW operating temperature of ridge waveguide QC laser at these long wavelengths between 9.6 to 10.3 μm . For the best performing QC lasers discussed in this Chapter, their ridge widths are $\sim 16\text{-}18 \mu\text{m}$, while for the best performing QC laser at shorter wavelength of $\lambda \approx 8.2 \mu\text{m}$ as described in Chapter 2, the ridge-width is as narrow as 8 μm . To enable the use of a narrow ridge-width without causing obvious increase in laser threshold at these long wavelengths between 9.6 to 10.3 μm , the buried heterostructure is one solution, as the lateral regrown InP avoids the side-wall loss.

Additionally, although the performance of these long wavelength QC lasers are not higher than that for shorter wavelength at $\lambda \approx 8.2 \mu\text{m}$ studied in Chapter 2, the thermal resistance of these long wavelength QC lasers is much smaller than that for $\lambda \approx 8.2 \mu\text{m}$ lasers ($\sim 7 \text{ K/W}$ vs. 14 K/W). Therefore, the thermal resistance R_{th} shouldn't be directly related to the laser performance. The smaller thermal resistance for these long wavelength lasers results from their wider ridge width. For QC lasers with different dimensions, thermal conductance, defined as $G_{\text{th}}=1/(R_{\text{th}} \cdot S)$, is a better parameter to judge the capacity of heat dissipation. G_{th} is calculated as $\sim 220\text{-}280$ and $\sim 260\text{-}500 \text{ W}/(\text{Kcm}^2)$

for $\lambda \approx 9.6\text{-}10.3 \mu\text{m}$ QC lasers studied here and the $\lambda \approx 8.2 \mu\text{m}$ QC lasers (A887a) described in Chapter 2.

Finally, it is worthwhile to exam the difference between the designed laser thresholds and their actual measured values for these QC lasers at different wavelengths. Figure 3.26 shows the calculated and measured pulsed threshold current density at 300 K for all the QC lasers we have discussed so far. The measured laser threshold current densities are 1.6-3.2 kA/cm², which are much higher than the theoretical values of 0.65-0.83 kA/cm² based on a rate equation model and waveguide loss calculation including only free carrier absorption. This large discrepancy also exists for CW threshold current density, and motivates us to perform optical gain and loss measurement on these lasers, which is described in the next Chapter.

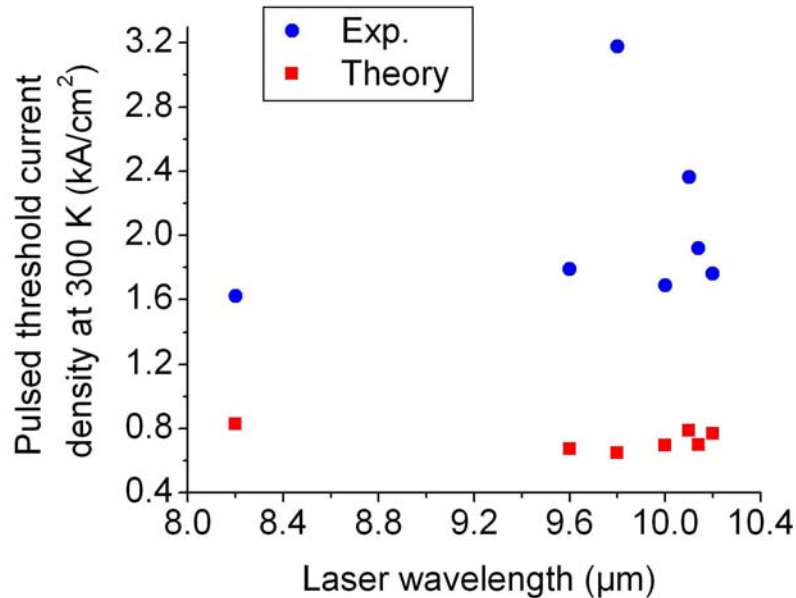


Figure 3.26 Measured and calculated threshold current density at 300 K for the best QC lasers at wavelengths of 8.2, 9.6-10.3 μm , which were presented in Chapters 2 and 3.

Chapter 4

Optical Gain and Loss Measurement in Quantum Cascade Lasers

4.1 Introduction

As discussed in Chapter 3, the measured threshold of QC lasers is usually larger than the designed value. In this case, we need the optical gain and waveguide loss information to understand the discrepancy. Additionally, the optical gain and loss parameters sometimes can help to find ways to improve the laser designs for achieving even better performance. Unfortunately, high-quality data regarding these two parameters are very limited in the current literature for high performance QC lasers, with the waveguide loss being reported only at room temperature in some cases [12, 45-48]. In this chapter, by using Hakki-Paoli method [71], a systematic study of the optical gain and waveguide loss versus temperature has been performed for room temperature CW QC lasers designed with vertical or diagonal transitions at various wavelengths between 8.2 and 10.3 μm [72]. A quantitative comparison between measured gain and loss and the theoretical values are presented.

The samples studied in this work are listed in Table 4.1. A887a, M532, M475 are 8.2, 9.6, and 10.3 μm “vertical-transition” QC lasers, respectively. They are based on a two phonon resonance design [27] which is widely employed in current high performance QC lasers. M474 and M490 are diagonal transition lasers at $\lambda \approx 9.8$ and 10.1 μm , respectively.

Their laser transitions were designed as diagonal transitions with a two phonon resonance scheme for carrier depopulation.

Table 4.1 QC laser samples studied in the optical gain and loss measurement.

Sample label	Laser design	Wavelength (μm)	Fabrication
A887a	Vertical transition	8.2	Ridge waveguide
M532	Vertical transition	9.6	Ridge waveguide
M475	Vertical transition	10.3	Ridge waveguide; Buried heterostructure
M474	Diagonal transition	9.8	Ridge waveguide
M490	Diagonal transition	10.1	Ridge waveguide

4.2 Methods

Besides the gain and loss measurements based on transmission technique, threshold comparison of un-coated and HR-coated devices, two other straightforward methods for measuring the optical gain and waveguide loss in QC lasers are the so-called “1/L” method [73] and the “Hakki-Paoli” method [74]. The “1/L” method relies on measuring threshold of several reliable devices of different cavity lengths. The second method, the Hakki-Paoli method, utilizes the subthreshold amplified spontaneous emission spectra of a single device. We used both methods in our initial experiments testing a 10.3 μm “vertical transition” QC laser (M475). The results from both methods agree well at room temperature, but do not agree at cryogenic temperatures. The reason is that for the “1/L” method, the gain coefficient and waveguide loss are very sensitive to the accuracy of

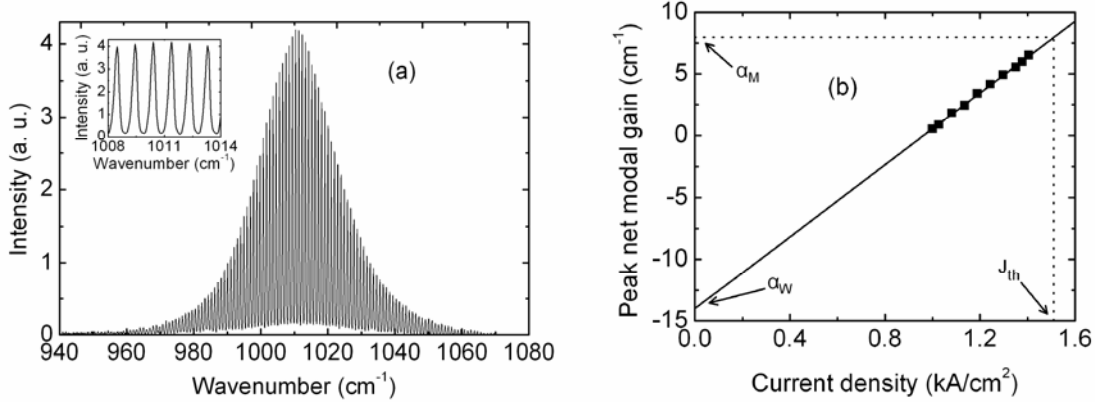


Figure 4.1 (a) Representative subthreshold amplified spontaneous emission spectrum of a 1.5 mm long, 16 μm wide, epitaxial-side-up mounted, ridge waveguide QC laser with thick metal top contact at $\lambda \approx 10.3 \mu\text{m}$ (M475). The laser is operated in CW mode at 0.33 A current and 120 K heat sink temperature. The inset shows the central Fabry-Perot modes in greater detail. (b) Peak net modal gain as a function of the injection current density, where the linear least squares fit (solid line) gives the gain coefficient and waveguide loss from its slope and y-axis intercept, respectively.

the threshold current measurement. At low temperature, because the laser thresholds are small values, the uncertainties in threshold due to performance variation from device to device result in a large variation in waveguide loss and gain coefficient. Conversely, the Hakki-Paoli method relies on measurements of a single device, which circumvents the difficulty of inter-device fluctuations and thus has been employed in the following temperature-dependent gain and loss measurements.

In the measurements based on Hakki-Paoli method, the subthreshold amplified spontaneous emission spectrum is recorded with a Magna 860 Fourier Transform Infrared Spectrometer (FTIR) and cooled MCT detector averaging 200 scans at 0.125 cm^{-1} resolution. The spectra of each sample are measured at different heat sink temperatures up to the maximum CW operating temperature. A typical spectrum for the 10.3 μm

vertical transition QC laser (M475) is shown in Figure 4.1 (a). The inset shows the Fabry-Perot modes at the central part of the spectrum in greater detail. The spectrum oscillates periodically without any additional maxima and minima, indicating single lateral mode emission as required by the Hakki-Paoli method.

The peak modal net gain can be calculated from the Fabry-Perot fringe contrast using

$$g_M J - \alpha_w = -\frac{1}{L} \left[\ln \left(\frac{\sqrt{P_{\max}/P_{\min}} + 1}{\sqrt{P_{\max}/P_{\min}} - 1} \right) - \ln \left(\frac{1}{R} \right) \right] \quad (4.1)$$

where g_M is the modal gain coefficient, J is the injection current density, L is the cavity length, R is the facet reflectivity. P_{\max} and P_{\min} are the neighboring maxima and minima of the spectral intensity. By calculating the net modal gain from the spectra at different injection currents (Figure 4.1 (b)), the linear fit gives the information of gain coefficient and waveguide loss from its slope and y-axis intercept, respectively. As an example, Figure 4.1 (b) shows the peak net modal gain as a function of current density at heat sink temperature of 120 K for a CW operated, 1.5 mm long, 16 μm wide, ridge waveguide QC laser (M475) with thick metal top contact, and its linear least squares fit results in a gain coefficient of 14.6 cm/kA and waveguide loss of 14.0 cm^{-1} .

During the above procedure, if a considerable transparency current or leakage current exists in the laser, then the net gain needs to be extrapolated to a positive current offset to give the right waveguide loss. However, since the transparency current or leakage current is negligible for QC lasers studied here, we extrapolated the net gain to zero current to get the waveguide loss. This negligible transparency current or leakage current is supported by the energy band diagram and current-voltage curves shown in Figure 4.2. At a voltage of 4 V where current starts flowing for the 120 K data, the energy band diagram in Figure

4.2 (a) shows no pathways of carrier leakage as the ground state of one injector is already well separated from the lower states of the following active region. For voltage higher than 4 V, the injector aligns fully with the upper laser level, and the current is carried by electron tunneling from the injector ground state into the upper laser level. Therefore, we consider it valid to extrapolate the net gain to zero current to extract the gain coefficient and waveguide loss.

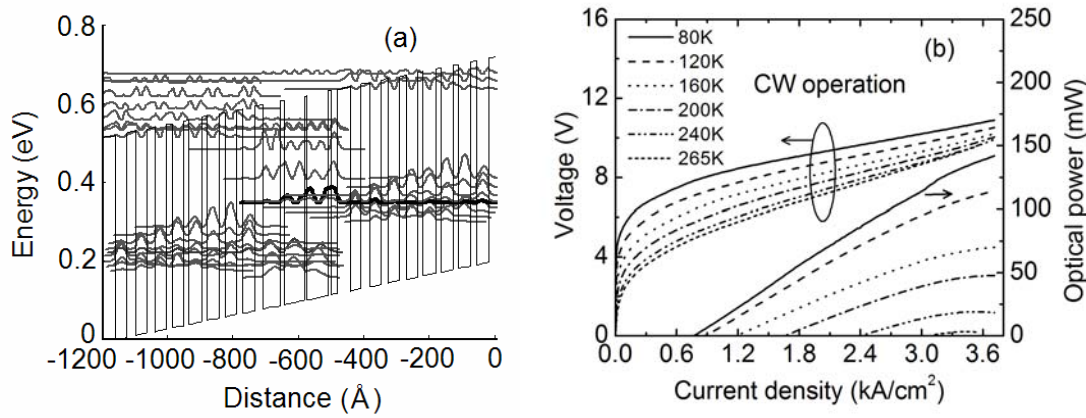


Figure 4.2 (a) Conduction band diagram of a portion of the active regions and injectors and the moduli squared of the relevant wave functions of sample M475 under a bias of 4 V, i.e. an electrical field of 18.6 kV/cm. The bold curve represents the upper laser level; (b) CW L-I-V curves of a 3.5 mm long, 17.7 μm wide QC laser at $\lambda \approx 10.3 \mu\text{m}$ (M475) at different heat sink temperatures.

4.3 Optical Gain and Loss in “Vertical Transition” $\lambda \approx 8.2 \mu\text{m}$ QC Lasers

The measured gain coefficient and waveguide loss for “vertical transition” $\lambda \approx 8.2 \mu\text{m}$ QC laser sample A887a are shown in Figure 4.3. The device is fabricated into ridge waveguide laser and operated in CW mode. The bottom x-axis of Figure 4.3 refers to the laser active core temperature, which is obtained by evaluating the temperature difference between laser core and heat sink from the pulsed and CW threshold current densities of the device.

As seen in Figure 4.3, the gain coefficient decreases as temperature increases, and agrees well with the theoretical values, which are calculated as (see also Equations 1.8 and 1.15 in sections 1.2.1 and 1.3, respectively)

$$g_M = \tau_3 \left(1 - \frac{\tau_2}{\tau_{32}}\right) \frac{4\pi e z_{32}^2 \Gamma}{\lambda_0 \epsilon_0 n L_p (2\gamma_{32})} \quad (4.2a)$$

$$\tau_i(T) = \tau_{i0} \frac{1}{1 + \frac{2}{\exp\left(\frac{E_{LO}}{kT}\right) - 1}} \quad (4.2b)$$

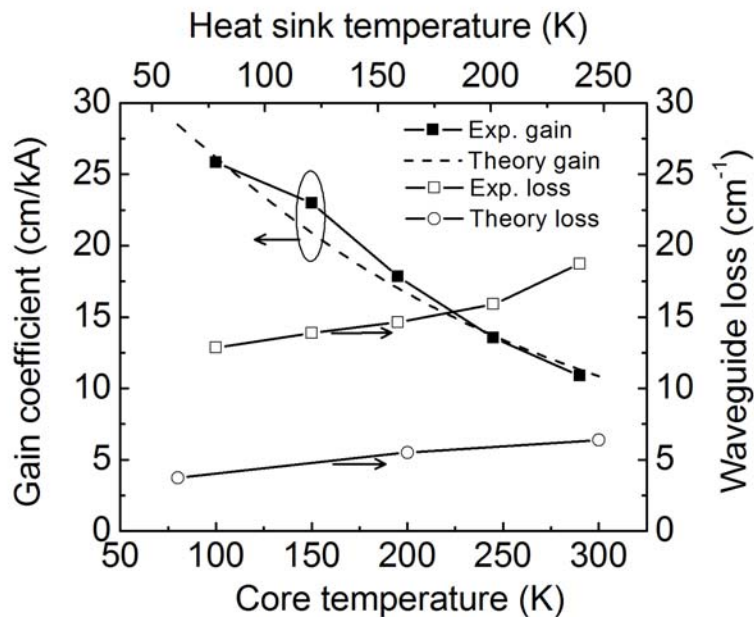


Figure 4.3 Measured gain coefficient (solid squares) and waveguide loss (open squares) versus core temperature for a 1.5 mm long, 9 μm wide ridge waveguide QC laser at $\lambda \approx 8.2 \mu\text{m}$ (A887a). The dashed line is the theoretical gain coefficient, and the circles are the calculated waveguide loss from free carrier absorption. Lines through data points are guides to the eye without fit parameters.

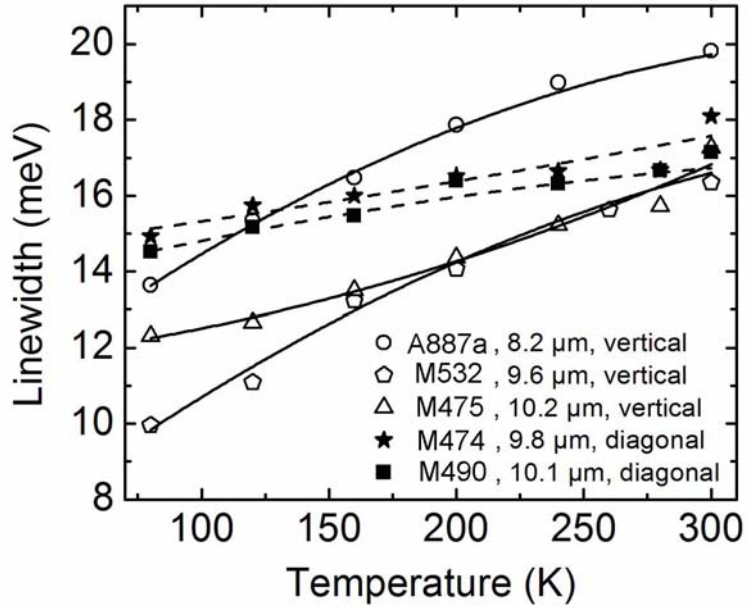


Figure 4.4 Full width half maximum (FWHM) linewidth of the electroluminescence of the laser transition at different heat sink temperatures for representative samples studied in this section. Solid and dashed lines are second order polynomial fit to the data points. Data are obtained from semi-circle mesas in pulsed mode under injection currents close to the laser threshold.

The waveguide loss of device A887a increases from 13 cm^{-1} to 18 cm^{-1} as the temperature increases from 100 to 300 K, and is more than ~ 3 times the calculated free carrier absorption. Here the free carrier absorption is calculated based on the Drude model [30], and an increase in the free carrier absorption with temperature is due to the decrease in electron mobility [75,76]. The electron scattering lifetime for InP cladding layer is taken as 0.37, 0.18, and 0.15 ps at 80, 200 and 300 K, respectively, which are obtained from the electron mobility data in Ref. [76]. For the active core region, the electron scattering lifetime is 0.1, 0.074, and 0.066 ps at 80, 200, 300 K, respectively, which are extracted from the measured electroluminescence linewidth in Figure 4.4 by assuming a

homogeneous broadening due to interface scattering. The designed doping levels of 1×10^{17} and $8\times10^{18} \text{ cm}^{-3}$ are used for the InP cladding layer and plasmon layer, and the designed average doping level $3.25\times10^{16} \text{ cm}^{-3}$ is used for the active core in the calculation. These carrier concentrations are assumed to be independent of temperature as indicated in Ref. [75]. The same procedure is applied for the free carrier calculation for the following other four samples (M532, M475, M474 and M490) except that the actual measured carrier concentrations are used for samples M475 and M490, which as confirmed in these samples are two times higher than their designed doping levels.

4.4 Optical Gain and Loss in “Vertical Transition” $\lambda \approx 9.6 \mu\text{m}$ QC Lasers

Next, we discuss a second vertical transition sample M532, which is designed as a two phonon resonance at $\lambda \approx 9.6 \mu\text{m}$, and is fabricated into ridge waveguide lasers. The gain coefficient and waveguide loss measured from a 1.5 mm long, 16 μm wide, ridge waveguide laser is given in Figure 4.5. Again, the gain coefficient agrees well with the design. The waveguide loss is more than two times that of the calculated free carrier absorption, and is almost a constant with temperature around 12 cm^{-1} .

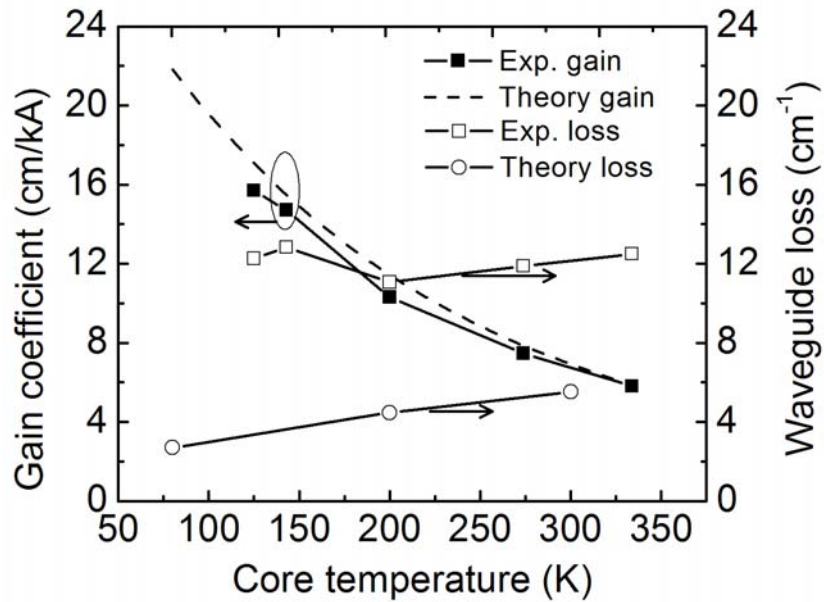


Figure 4.5 Measured gain coefficient (solid squares) and waveguide loss (open squares) versus core temperature for a 1.5 mm long, 16 μm wide ridge waveguide QC laser at $\lambda \approx 9.6 \mu\text{m}$ (M532). The dashed line is the theoretical gain coefficient, and the circles are the waveguide loss calculated from free carrier absorption. Lines through data points are guides to the eye.

4.5 Optical Gain and Loss in “Vertical Transition” $\lambda \approx 10.3 \mu\text{m}$ QC Lasers

We further measured a third sample, M475, which is a 10.3 μm QC laser based on a two phonon resonance with a vertical optical transition. This sample is processed into both ridge waveguide and buried heterostructure lasers. The gain coefficients and waveguide losses for 1.5 mm long, 16 μm wide ridge waveguide and buried heterostructure lasers are given in Figure 4.6. It can be seen that the gain coefficients for both lasers are close, and agree well with the designed values. For the waveguide loss, it is again much higher than the calculated free carrier absorption.

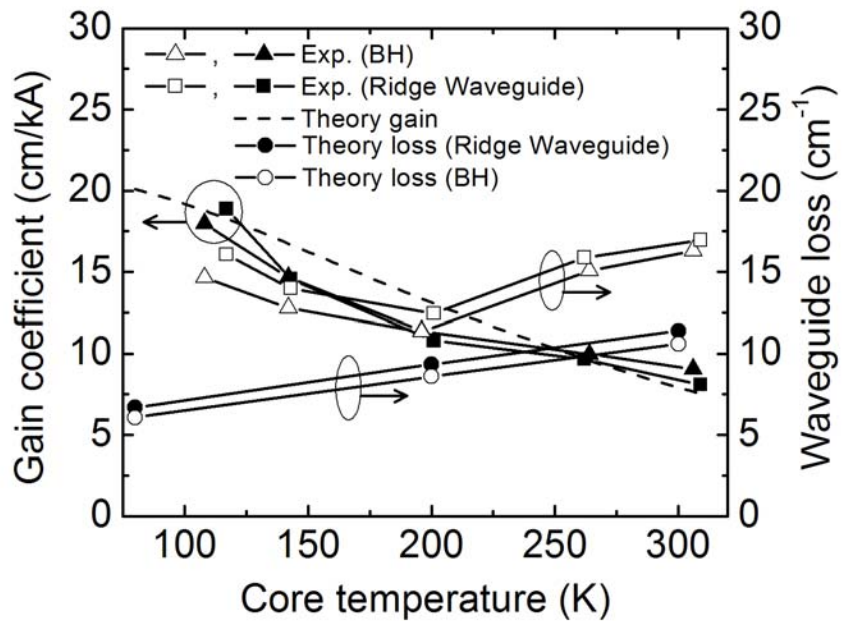


Figure 4.6 Measured gain coefficient and waveguide loss versus core temperature for a 1.5 mm long, 16 μm wide, ridge waveguide QC laser (squares) and a buried heterostructure QC laser (triangles) at $\lambda \approx 10.3 \mu\text{m}$ (M475). The dashed line is the theoretical gain coefficient, and the solid and open circles are calculated waveguide loss from free carrier absorption for the ridge waveguide and buried heterostructure lasers, respectively. Lines through data points are guides to the eye.

Also, the buried heterostructure laser has a slightly lower waveguide loss by $\sim 1 \text{ cm}^{-1}$ than the ridge waveguide laser, which suggests that the side wall $\text{Si}_x\text{N}_y/\text{Ti}/\text{Au}$ is not a major source of loss for the ridge waveguide structure at these ridge widths. In the calculation of the free carrier absorption for this sample, we used the actual measured doping level from Secondary Ion Mass Spectrometry (SIMS) and Capacitance-Voltage measurements as shown in Figure 4.7 and Figure 4.8, respectively. These measured doping levels are two time higher than the designed values. However, free carrier

absorption calculated from these higher doping level still cannot fully account the measured waveguide loss, which suggests other loss origins.

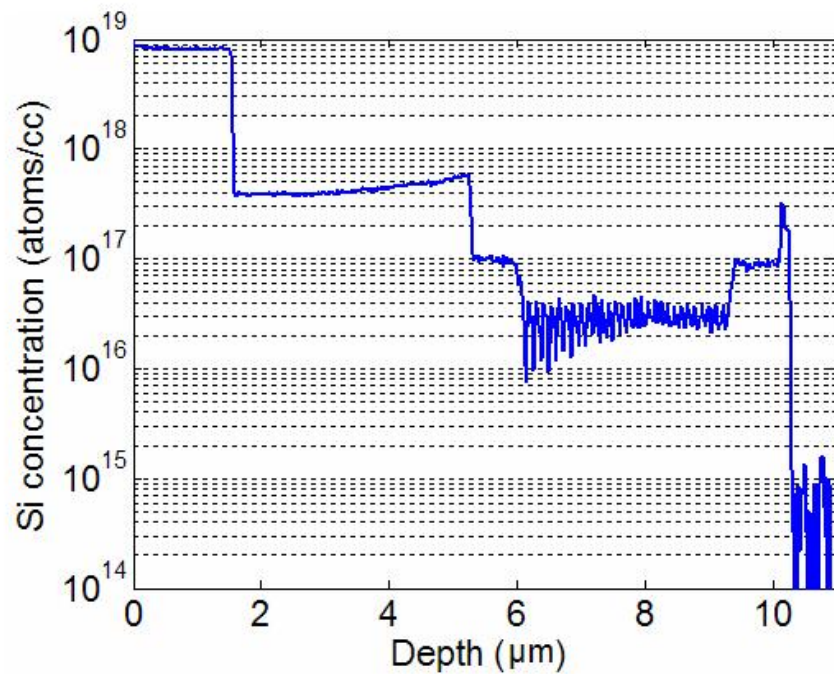


Figure 4.7 Silicon concentration in M475 from Secondary Ion Mass Spectrometry (SIMS) measurement.
[Data by Evans Analytical Group]

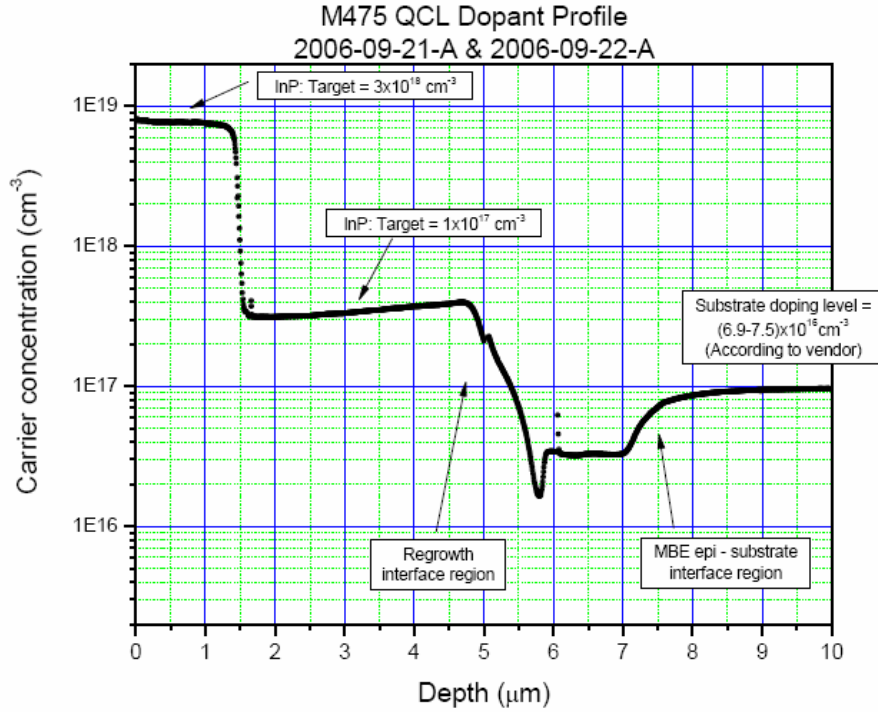


Figure 4.8 Carrier concentration in sample M475 from Capacitance-Voltage measurement. [Data by Maxion Technologies]

A prime candidate for the higher waveguide loss than estimated from free carrier absorption is intersubband resonant absorption, which was found in the energy band diagram (solid arrow) shown in Figure 4.9 (a). The resonant absorption coefficient can be calculated by using [77]

$$\alpha = n_i g_{i,j} \quad (4.3)$$

where n_i is the carrier concentration on the lower state i , and $g_{i,j}$ is the absorption cross section

$$g_{i,j} = \frac{4\pi e^2 z_{ij}^2 \Gamma}{\epsilon_0 n L_p \lambda_{ij} (2\gamma_{ij})} \left[\frac{\gamma_{ij}^2}{(\hbar\omega - E_{i,j})^2 + \gamma_{ij}^2} \right] \quad (4.4)$$

where $\hbar\omega$ is the laser photon energy, E_{ij} is the energy separation between resonant states i and j , λ_{ij} is the corresponding wavelength, and $2\gamma_{ij}$ is the full width at half maximum

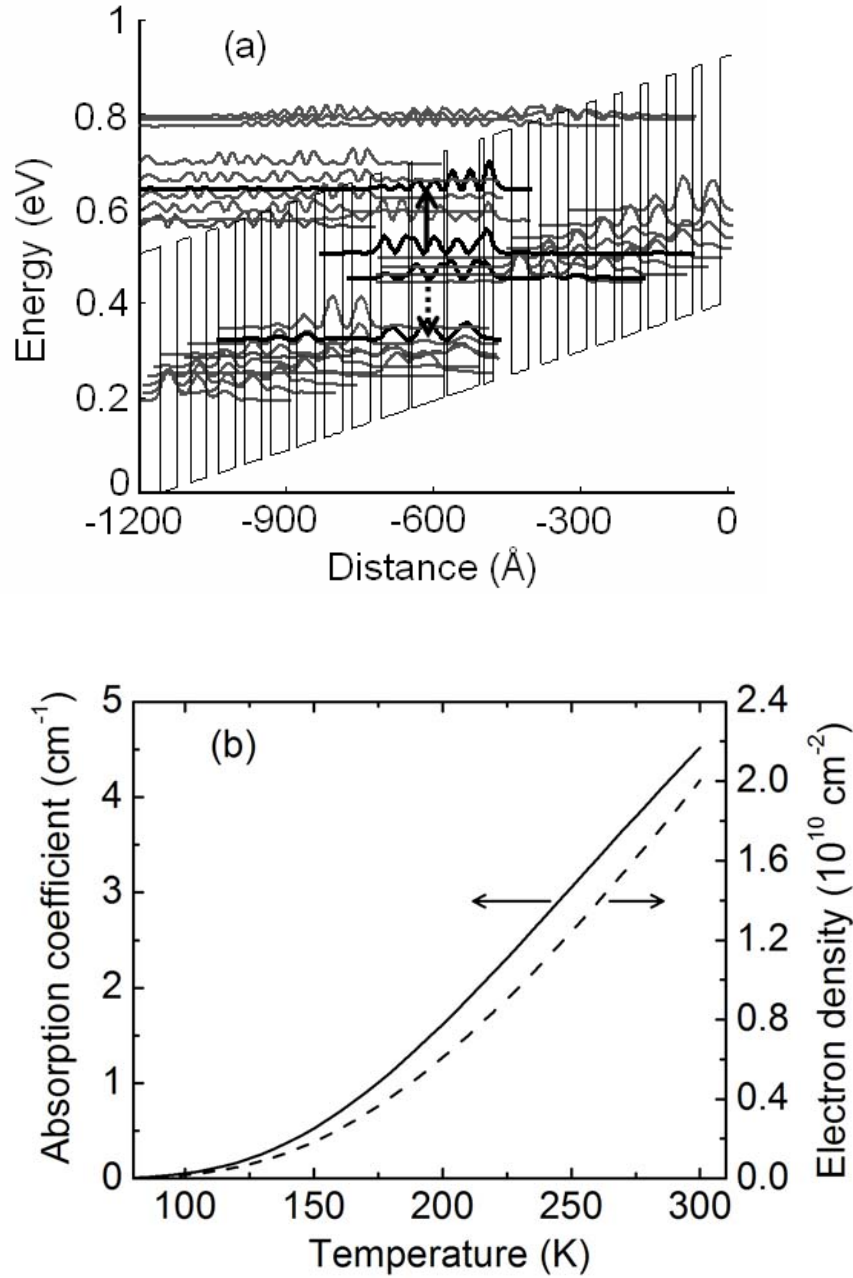


Figure 4.9 (a) Conduction band diagram of a portion of the active regions and injectors and the moduli squared of the relevant wave functions of a $\lambda \approx 10.3 \mu\text{m}$ QC laser (M475) with a 4 quantum well active region. An electric field of 39 kV/cm is applied. The dotted arrow indicates the laser transition. The solid arrow represents a pathway of resonant absorption. (b) Calculated absorption coefficient of the intersubband resonant transition indicated by the solid arrow in (a) and the thermally excited electron density on the state above the upper laser level.

(FWHM) emission linewidth for the transition between them. For the resonant absorption in Figure 4.9 (a), the thermally populated carrier concentration on the resonant absorption state i takes the form of

$$n_i = n_g \exp\left(-\frac{\Delta E}{kT}\right) \quad (4.5)$$

where the n_g is the doping sheet density, and ΔE is the energy separation between the resonant level i and the injector ground state. The transition linewidth $2\gamma_{ij}$ between these higher lying levels is unknown, and here we used the measured linewidth of the lower lying laser transition as shown in Figure 4.4 as a lower bound. The increasing linewidth with temperature is likely due to thermally enhanced interface roughness scattering and/or non-parabolicity effects. The corresponding absorption is calculated in Figure 4.9 (b). As the temperature increases, the electrons start to populate the state above the upper laser level, and resonant absorption occurs into resonant states above. Its absorption coefficient increases to 4.5 cm^{-1} at 300 K. This accounts for the difference between the measured waveguide loss and calculated free carrier absorption at room temperature. However, there is still a large difference at low temperatures, which needs further study.

4.6 Optical Gain and Loss in “Diagonal Transition” $\lambda \approx 9.8 \mu\text{m}$ QC Lasers

Besides the above vertical transition QC lasers, we also measured a diagonal transition QC lasers (M474) at $\lambda \approx 9.8 \mu\text{m}$. The sample was processed into ridge waveguide lasers. Its gain coefficients and waveguide losses measured from a 1.5 mm long, 12 μm wide QC laser are shown in Figure 4.10. It is seen that the waveguide loss decreases with temperature and is again much higher than the estimated from free carrier absorption. Resonant absorption is a possible factor resulting in this decreasing waveguide loss with

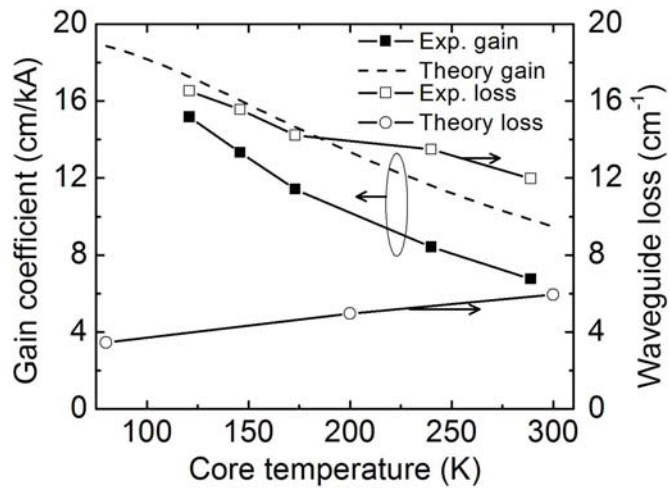


Figure 4.10 Measured gain coefficient (solid squares) and waveguide loss (open squares) versus core temperature for a 1.5 mm long, 12 μm wide ridge waveguide diagonal transition QC laser at $\lambda \approx 9.8 \mu\text{m}$ (M474). The dashed line is the theoretical gain coefficient, and the circles are the waveguide loss calculated from free carrier absorption. Lines through data points are guides to the eye.

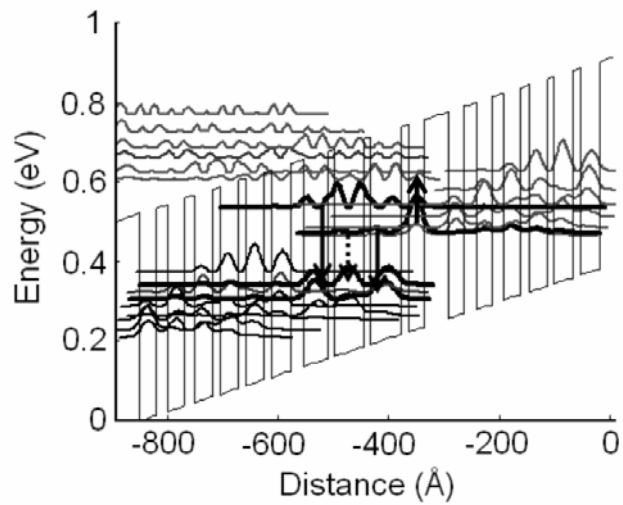


Figure 4.11 Conduction band diagram of a portion of the active regions and injectors and the moduli squared of the relevant wave functions of a $\lambda \approx 9.8 \mu\text{m}$ diagonal transition QC lasers (M474). An electric field of 45 kV/cm is applied. The dotted arrow indicates the laser transition. The downwards pointing solid arrows represent parasitic optical transitions, and the upwards pointing solid arrow indicates a pathway of resonant absorption.

temperature. We find a resonant absorption from injector ground state and a higher excited state as shown by the upwards pointing solid arrow in Figure 4.11. By assuming that the carrier concentration on the injector ground level to be the doping level, the calculated resonant absorption coefficient is shown in Figure 4.12. It decreases from 2.9 to 2.5 cm^{-1} as the temperature increases because of a decreasing absorption cross section (see Equation 4.4) resulting from the transition linewidth broadening. The gain coefficients follow the trend of the calculated values, but are smaller than what was calculated. One factor we attribute in part the smaller gain coefficients to is carrier leakage to other transitions, which can be seen from the room temperature electroluminescence signals shown in Figure 4.13 (b). There are two strong parasitic optical transitions, which are indicated by the downwards pointing solid arrows in Figure 4.11. The peak at $\sim 1195 \text{ cm}^{-1}$ is from the transition between upper laser level and a level beneath the lower laser level, which doesn't affect the gain coefficient. However, The second peak at $\sim 1511 \text{ cm}^{-1}$, which is present only at high temperatures ($> 160 \text{ K}$), results from the transition between a higher state above the upper laser level and the lower laser level indicating a temperature-induced electron leakage path. This second peak at $\sim 1511 \text{ cm}^{-1}$ doesn't exist at low temperatures as indicated by the electroluminescence at 80 K in the Figure 4.13 (a).

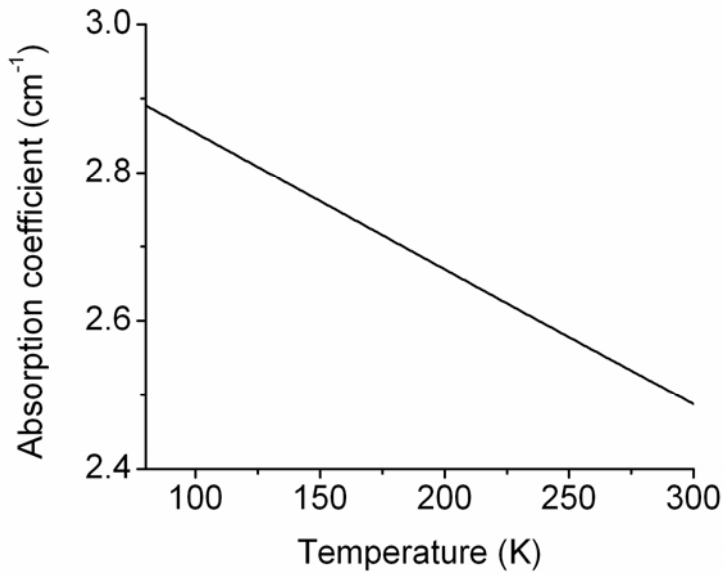


Figure 4.12 Calculated absorption coefficient of an intersubband resonant transition from the injector ground state to a higher lying level for sample M474.

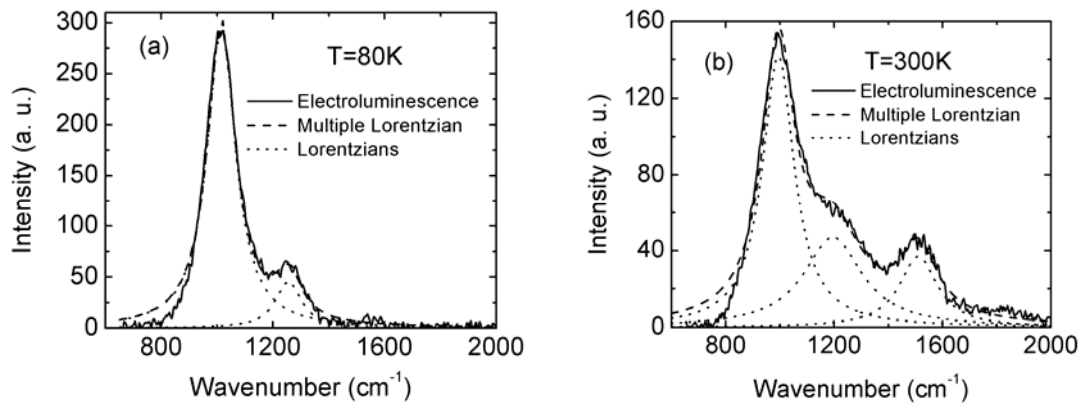


Figure 4.13 Measured electroluminescence of a 200 μm diameter, semi-circle mesa from $\lambda \approx 9.8 \mu\text{m}$ diagonal transition QC laser sample (M474) under pulsed operation at a current close to the laser threshold.

4.7 Optical Gain and Loss in “Diagonal Transition” $\lambda \approx 10.1 \mu\text{m}$ QC Lasers

The measured gain coefficient and waveguide loss for a second diagonal transition QC laser sample with $\lambda \approx 10.1 \mu\text{m}$ (M490) is shown in Figure 4.14. Like previous $\lambda \approx 9.8 \mu\text{m}$

diagonal transition laser (M474), its waveguide loss slightly decreases with temperature, and is more than 2 times of the waveguide loss calculated from free carrier absorption using the actual doping level measured from SIMS technique. A resonant absorption from the injector ground state and a higher excited state is found from its energy band diagram, which is similar to that in M474 shown in Figure 4.11. The calculated resonant absorption coefficient is shown in Figure 4.15, which decreases from 5.0 to 3.6 cm⁻¹ when temperature increases from 80 to 300 K.

For the gain coefficient, it decreases with temperature, but it is smaller than the designed values. Like the previous $\lambda \approx 9.8$ μm sample M474, carrier leakage is part of the reason. Figure 4.16 (b) shows its electroluminescence at room temperature. There are two parasitic optical transitions, and the peak at ~ 1484 cm⁻¹ indicates a carrier leakage path, resulting in a smaller gain coefficient. As a comparison with the vertical transition lasers, similar parasitic transitions also exist for the vertical transition QC lasers, but their intensities are much weaker with less effect on the optical gain. As an example, the electroluminescence spectrum of sample M532 is given in Figure 4.16 (a). These electroluminescence signals indicate some carrier populations on the upper laser level and higher lying levels for In_{0.53}Ga_{0.47}As/Al_{0.48}In_{0.52}As QC lasers. The electron distribution in In_{0.53}Ga_{0.47}As/AlAs_{0.56}Sb_{0.44} QC lasers was studied by Vitiello et al. using interband photoluminescence technique [78]. They found that electrons are mainly populated on the injector ground state or the first level in the active region, and the population at upper laser level is negligible. Here the small amounts of electrons on the higher levels in the active region are resolvable from intersubband electroluminescence. From the electroluminescence intensity shown in Figure 4.16, the ratio of electrons on the

upper laser level to those on the level above the upper laser level is $\sim 30:1$ for both typical vertical transition laser M532 and diagonal transition laser M490. From this electron distribution and using a rate equation model including electron injection into both the upper laser level and the level right above, an injection efficiency into upper laser level is deduced as 90% and 82% for M532 and M490 at room temperature, respectively.

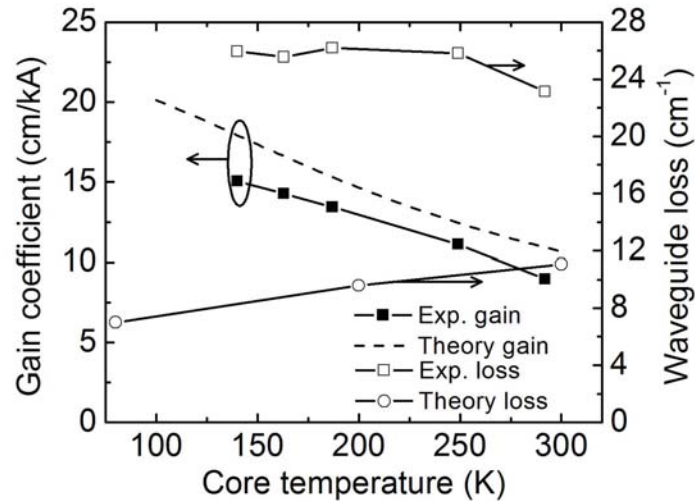


Figure 4.14 Measured gain coefficient (solid squares) and waveguide loss (open squares) versus core temperature for a 1.5 mm long, 15 μm wide ridge waveguide diagonal transition QC laser at $\lambda \approx 10.1 \mu\text{m}$ (M490). The dashed line is the theoretical gain coefficient. The circles show the calculated waveguide losses from free carrier absorption using the measured doping levels. Lines through data points are guides to the eye.

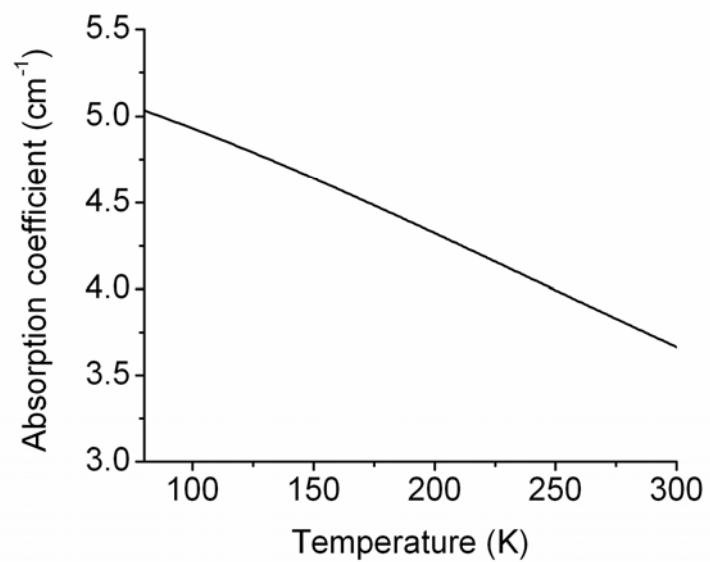


Figure 4.15 Calculated absorption coefficient of an intersubband resonant transition from the injector ground state to a higher lying level for sample M490, which is similar to the resonant absorption indicated by the upwards pointing solid arrow in Figure 4. 11.

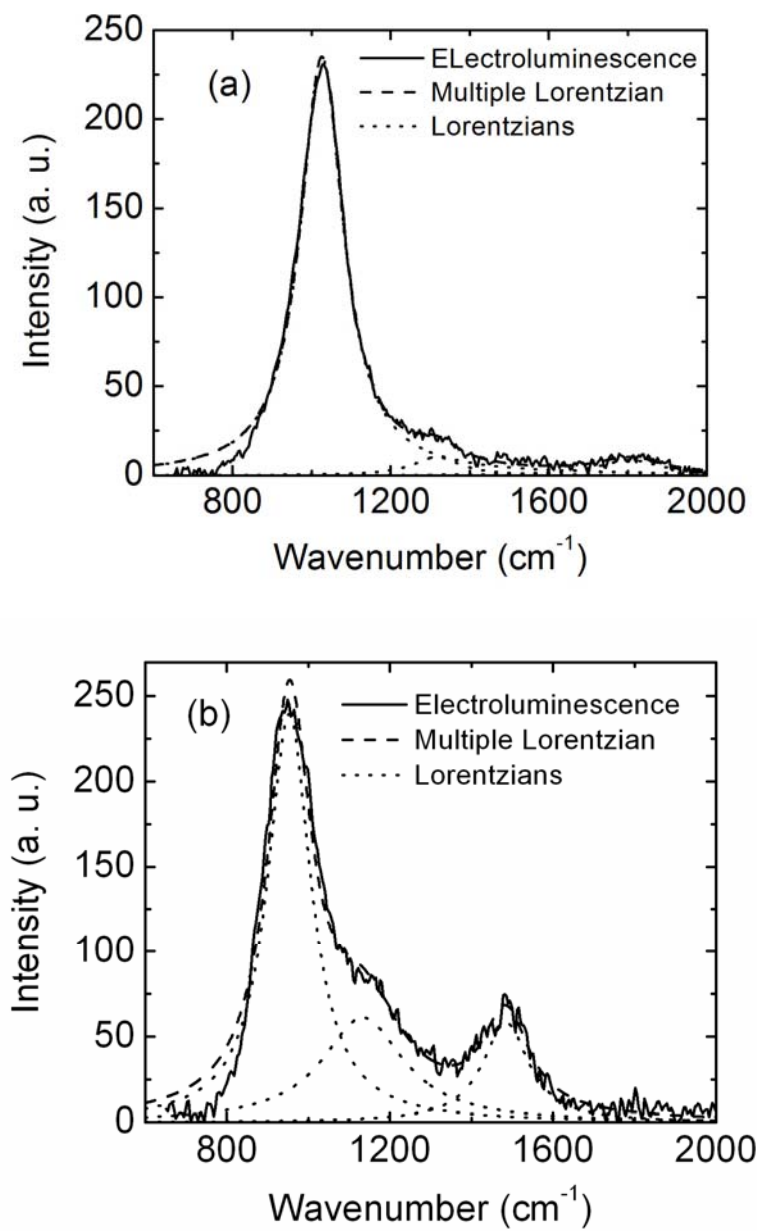


Figure 4.16 Measured room temperature electroluminescence of a $200 \mu\text{m}$ diameter, semi-circle mesa in pulsed mode at a current close to the laser threshold for (a) $\lambda \approx 9.6 \mu\text{m}$ vertical transition QC laser sample (M532) and (b) $\lambda \approx 10.1 \mu\text{m}$ diagonal transition QC laser sample (M490).

4.8 Conclusion and Discussion

From the measured gain coefficient and waveguide loss for the various vertical transition or diagonal transition QC lasers in this work, we can see that the gain coefficient decreases with increasing temperature as expected. It is close to the designed value for vertical transition lasers (A887a, M532 and M475), but smaller than the design for diagonal transition lasers (M474 and M490) partially because of some carrier leakages.

The measured waveguide loss ($12\text{-}25 \text{ cm}^{-1}$) is more than 2 times higher than that calculated from free carrier absorption ($3\text{-}12 \text{ cm}^{-1}$). Also different temperature dependences of the waveguide loss were observed, especially for the three samples M532, M475 and M474, which have the exact same waveguide design, but different active regions. In particular, the waveguide loss remains nearly constant for the $9.6 \mu\text{m}$ vertical transition laser M532 (Figure 4.5), decreases first and then increases for the $10.3 \mu\text{m}$ vertical transition laser M475 (Figure 4.6), and decreases monotonously with temperature for the $9.8 \mu\text{m}$ diagonal transition laser M474 (Figure 4.10). These high waveguide losses and their complex temperature dependences, which are different from that calculated from free carrier absorption, suggest other loss mechanisms inside the laser active cores. Resonant absorption is a likely factor resulting in this complex temperature-dependence of the waveguide loss. As temperature increases, those absorption levels are shifted either closer to or farther away from resonance. Meanwhile, the transition linewidth broadens. These two effects cause the absorption cross section (Equation 4.4) to either decrease or increase with temperature. This complex behavior

together with carrier population through thermal excitation, tunneling and scattering processes can result in both as increasing or decreasing waveguide loss with temperature.

We estimated the resonant absorption in our different samples from band structure calculations without considering their changes with temperature. We found a resonant absorption between two higher excited states in the active region for the $\lambda \approx 10.3$ μm vertical transition laser M475, which increases with temperature to up 4.5 cm^{-1} as shown in Figure 4.9 (b) because of an increasing thermally-excited population on the absorption ground state. We also found a resonant absorption in two diagonal transition lasers M474 and M490, which is from the injector ground state to a higher excited state. The estimated absorption, as shown in Figs. 4.12 and 4.15, decreases with temperature because of a decreasing absorption cross section resulting from the linewidth broadening. For samples A887a and M532, we did not find any noticeable resonant absorption from their band structures. Due to uncertainties of parameters such as transition linewidth, electron energy levels shifts due to temperature or layer thickness deviation from design, our estimated resonant absorption model can not fully explain the high waveguide loss and different temperature-dependence of all samples. Therefore there might be other resonant absorptions which do not show up in our band structure calculation or some additional loss origins such as roughness scattering, defects states etc., which require further investigation as discussed in Chapter 6.

Chapter 5

High Performance Quantum Cascade Lasers at $\lambda \approx 5.3 \mu\text{m}$

5.1 Introduction

Aside from the previously described high performance QC lasers between 8.2 and 10.3 μm using lattice matched InGaAs/AlInAs material, shorter wavelength $\lambda \approx 5.3 \mu\text{m}$ QC lasers based on strain-compensated InGaAs/AlInAs are presented in this chapter. QC lasers at this particular wavelength are especially useful for Nitric Oxide (NO) sensing for environmental and automotive applications. This work was conducted in collaboration with Corning Inc. and constitutes their entry into the QC laser and sensor field, enabled in the past also throughout this thesis work.

The QC lasers are designed as two phonon resonance, vertical transition active region lasers. As this was the first growth of QC laser at Corning Inc., three modified designs with different doping levels in the injectors and waveguide claddings are used to overcome the uncertainty in background doping. High performance with maximum CW operation temperature of 360 K is achieved for a conventional 3.5 mm long cavity laser with the lowest doping levels. In addition, by using a shorter 0.5 mm long cavity and HR coating on both laser facets, room temperature CW operation with very small heat dissipation of 1.2-1.7 W over the lasing range is realized to facilitate more compact laser package with less overall heat load cooling needs.

5.2 Laser Design

To design a high performing QC laser at $\lambda \approx 5.3 \mu\text{m}$, the band offset of 0.52 eV of the lattice-matched InGaAs/AlInAs material is not enough to accommodate all necessary bound electron states and at the same time to prevent carrier leakage to the conduction band continuum. In this case, the strain-compensated InGaAs/AlInAs material is a choice, as it has a larger band offset taking advantage of the strain [79]. Figure 5.1 shows the calculated conduction band offset versus alloy composition for an $\text{In}_x\text{Ga}_{1-x}\text{As}/\text{In}_y\text{Al}_{1-y}\text{As}$ strain-compensated bilayer using the model-solid theory [80]. The dashed line represents the composition we used here for $\lambda \approx 5.3 \mu\text{m}$ QC laser design. It is $\text{In}_{0.354}\text{Al}_{0.646}\text{As}/\text{In}_{0.661}\text{Ga}_{0.339}\text{As}$ with a band offset of 0.786 eV.

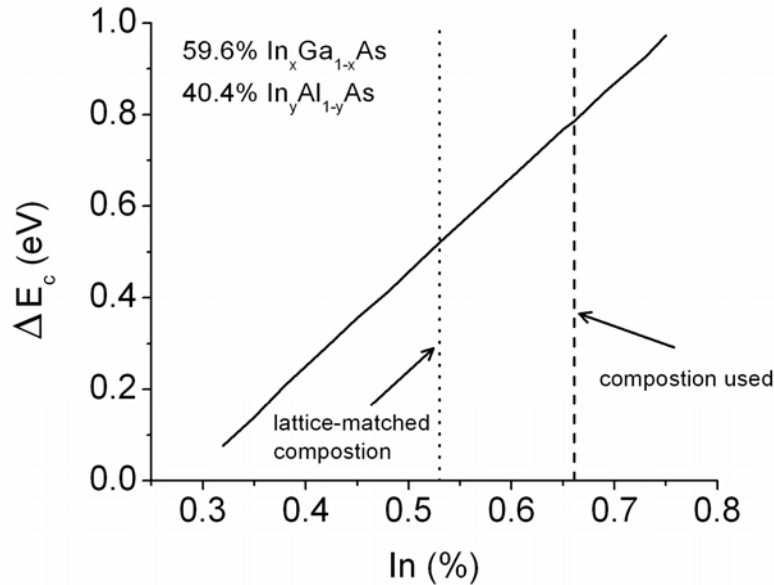


Figure 5.1 Calculated conduction band offset as a function of InAs mole fraction of the $\text{In}_x\text{Ga}_{1-x}\text{As}$ layer for an $\text{In}_x\text{Ga}_{1-x}\text{As}/\text{In}_y\text{Al}_{1-y}\text{As}$ strain-compensated bilayer grown on an InP substrate. The dotted line represents the lattice-matched composition, and the dashed line indicates the composition used in $\lambda \approx 5.3 \mu\text{m}$ QC laser design.

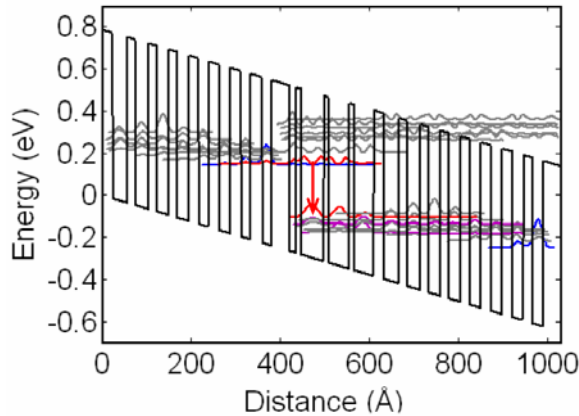


Figure 5.2 Conduction band diagram of a portion of the active regions and injectors and moduli squared of the relevant wave functions of a $\lambda \approx 5.3 \mu\text{m}$ QC laser with a 4 quantum well active region. An electric field of 63 kV/cm is applied. The red arrow indicates the laser transition.

The $\lambda \approx 5.3 \mu\text{m}$ QC laser sample E107253-1 was designed as a “two phonon resonance” QC laser with a vertical transition. Its electron energy band diagram is shown in Figure 5.2. The layer sequence (in Å) of one period of active region and injector is **40/15/11/49/12/46/13/41/24/34/18/30/19/26/19/26/20/25/23/25/23/23/24/23**, where In_{0.354}Al_{0.646}As barrier layers are in bold, In_{0.661}Ga_{0.339}As well layers are in roman, and the n-doped ($1.8 \times 10^{17} \text{ cm}^{-3}$) layers are underlined. In order to meet the requirement of compensated strain, the lattice mismatch of one period is minimized as 0.0054% in this design by adjusting both the layer thicknesses and composition. The laser transition, with energy 250 meV, is indicated by the red arrow in Figure 5.2. The lifetimes of the upper and lower laser levels are designed as 1.75 and 0.22 ps, respectively. The optical dipole matrix element is 1.73 nm. A large energy separation of 147 meV between the lower laser level and the ground state of the next down stream injector is chosen to suppress thermal backfilling. Additionally, the energy separation between the upper laser level and the conduction band continuum is designed as large as 408 meV to avoid thermionic

emission as the target operating range is room temperature operation in CW mode. The FOM of this design is 505 ps \AA^2 , smaller than that of previous QC lasers at longer wavelengths from 8.2 to 10.3 μm due to a smaller dipole matrix element.

Twenty-six periods of injector and active region are sandwiched between 0.2 μm thick low doped ($5 \times 10^{16} \text{ cm}^{-3}$) $\text{In}_{0.53}\text{Ga}_{0.47}\text{As}$ layers. The top waveguide cladding consists of a 2.5 μm thick low doped ($1 \times 10^{17} \text{ cm}^{-3}$) InP, followed by a 1.2 μm thick highly doped ($8 \times 10^{18} \text{ cm}^{-3}$) InP plasmon layer and a heavily doped 10 nm InP contact layer. The calculated intensity profile of the fundamental mode is shown in Figure 5.3. The waveguide loss α_w is calculated as 1.67 cm^{-1} , and the confinement factor Γ is 0.67.

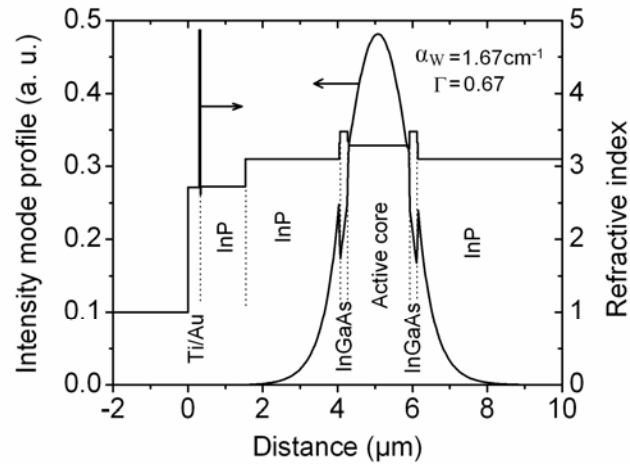


Figure 5.3 Intensity profile of the fundamental TM mode and profile of the real part of the refractive index of the dielectric waveguide calculated at $\lambda \approx 5.3 \mu\text{m}$.

In order to study the effect of the doping level on the laser performance, two additional samples E107268B and E107276F with reduced doping levels were designed. For sample E107268B, the doping levels in the InP top and bottom waveguide claddings are reduced by half from the original 1×10^{17} to $0.5 \times 10^{17} \text{ cm}^{-3}$. For sample E107276F, the doping

levels in both InP waveguide cladding layers and the active core are reduced by half, i.e., the doping levels in upper and lower InP waveguide claddings are decreased from 1×10^{17} to $0.5 \times 10^{17} \text{ cm}^{-3}$, and the doping level in the active core is reduced from 1.8×10^{17} to $0.9 \times 10^{17} \text{ cm}^{-3}$. The waveguide loss is calculated as 1.35 and 1.0 cm^{-1} for E107268B and E107276F, respectively.

The above three samples with different doping levels were grown by MOCVD by Catherine G. Caneau at Corning Inc., and the wafers were processed into deep-etched, ridge waveguide with $7 \mu\text{m}$ thick electroplated gold on top. The samples were cleaved into different cavity lengths, and epitaxial-side-up mounted on copper mounts for testing.

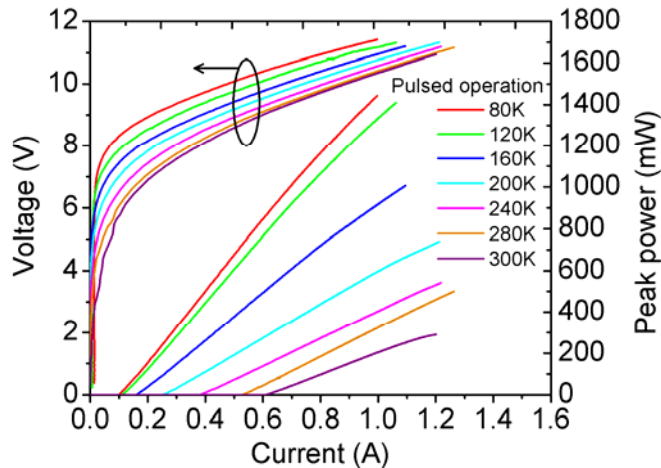


Figure 5.4 Pulsed L-I-V curves of a back facet HR coated, 3.5 mm long, $9.7 \mu\text{m}$ wide, ridge waveguide QC laser (E107253-1) with thick metal top contact at various heat sink temperatures.

5.3 Ridge Waveguide Laser with Thick Metal Top Contact

Figure 5.4 shows the pulsed L-I-V curves of a back facet HR coated, 3.5 mm long, $9.7 \mu\text{m}$ wide QC laser from the first wafer E107253-1. Its peak power exceeds 1.4 W at 80 K ,

and 300 mW at room temperature, and the slope efficiency reaches 1.74 W/A and 530 mW/A at 80 K and 300 K, respectively.

The CW L-I-V curves and spectrum of the laser are shown in Figure 5.5. It emits a CW power of ~ 600 mW at least at 80 K and functions up to 290 K. The lasing wavelength is ~ 5.33 μm , close to the designed value, as shown in Figure 5.5 (b). Its threshold current density as a function of heat sink temperature is shown in Figure 5.6. When temperature increases from 80 to 300 K, the pulsed laser threshold current density increases from 0.30 to 1.84 kA/cm². For CW operation, the threshold current density increases from 0.33 kA/cm² at 80 K to 4.27 kA/cm² at 290 K. The characteristic temperature T_0 is 114 and 79 K in pulsed and CW mode, respectively. The optical gain and waveguide loss at room temperature are extracted through the “1/L” approach as shown in Figure 5.7. The gain coefficient and waveguide loss are extracted as 7.08 cm/kA and 9.14 cm⁻¹, respectively. This waveguide loss is again much higher than the calculated value 1.67 cm⁻¹.

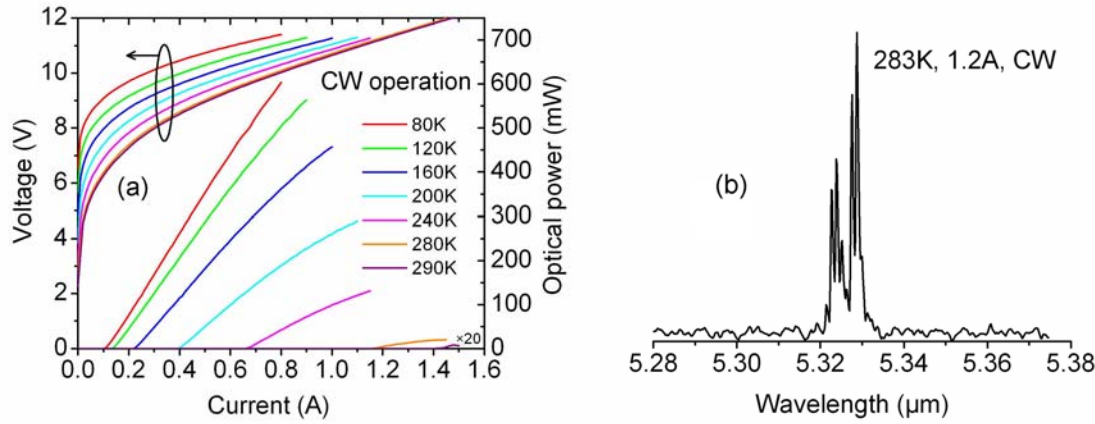


Figure 5.5 (a) CW L-I-V curves of a back facet HR coated, 3.5 mm long, 9.7 μm wide, ridge waveguide QC laser (E107253-1) with thick metal top contact at various heat sink temperatures. (b) A typical Fabry-Perot laser spectrum at 1.2 A and 283 K heat sink temperature.

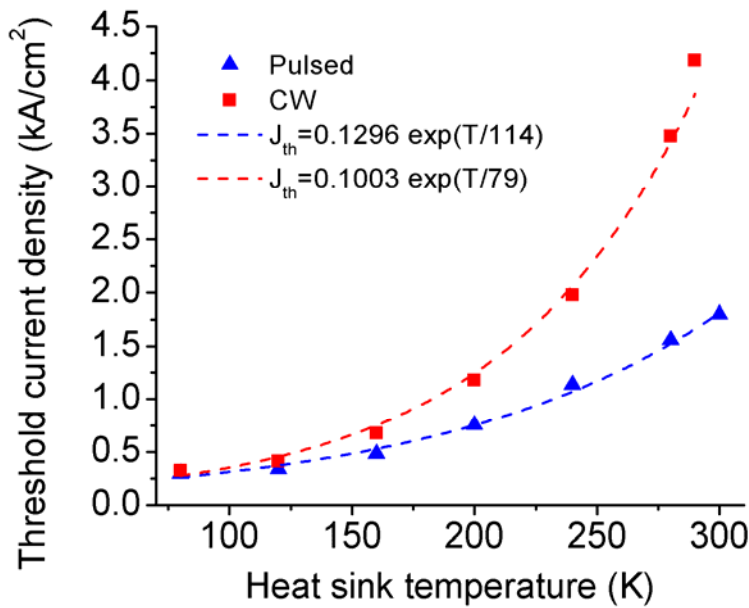


Figure 5.6 Threshold current density of a back facet HR coated, 3.5 mm long, 9.7 μm wide, ridge waveguide QC laser (E107253-1) with thick metal top contact in both pulsed and CW operations. The characteristic temperatures are 114 and 79 K for pulsed mode and CW, respectively.

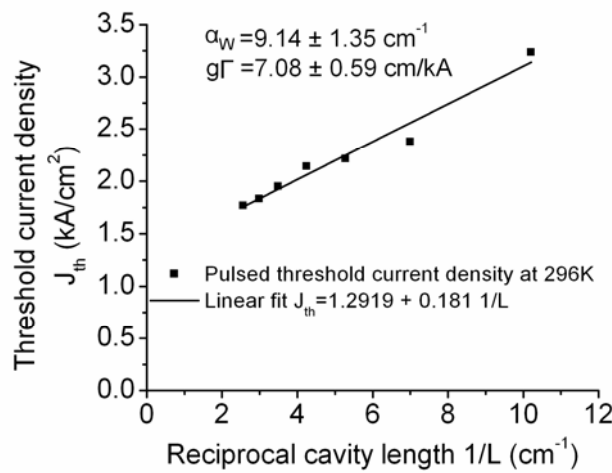


Figure 5.7 Pulsed threshold current density at 296 K versus reciprocal cavity length for QC lasers from wafer E107253-1. A waveguide loss of 9.14 cm^{-1} and gain coefficient of 7.08 cm/kA are extracted from this measurement.

The performance of the second wafer E107268B with reduced doping level in the InP bottom and top waveguide cladding layers is shown in Figure 5.8. A back facet HR coated, 3.5 mm long, 8.4 μm wide QC laser emits a CW power of 27.6 mW at 300 K, and functions up to 316 K, which is a 26 K improvement as compared with the first, higher doped sample E107253-1. A typical CW spectrum is shown in Figure 5.8 (b). The laser wavelength is 5.35 μm , which is close to the designed value. Any wavelength difference with respect to the first wafer is not significant. The laser threshold current density as a function of the heat sink temperature is shown in Figure 5.9. The pulsed threshold increases from 0.49 kA/cm² at 160 K to 1.89 kA/cm² at 316 K, and the CW threshold increases from 0.58 kA/cm² at 160 K to 3.98 kA/cm² at 316 K. These threshold current densities are lower than those for sample E107253-1 with higher doping in the waveguide cladding layers. The extracted characteristic temperature T_0 is 114 and 82 K in pulsed mode and CW, respectively, which are close to the values for sample E107253-1. This is expected as no change was made to the doping level in active regions and injectors for

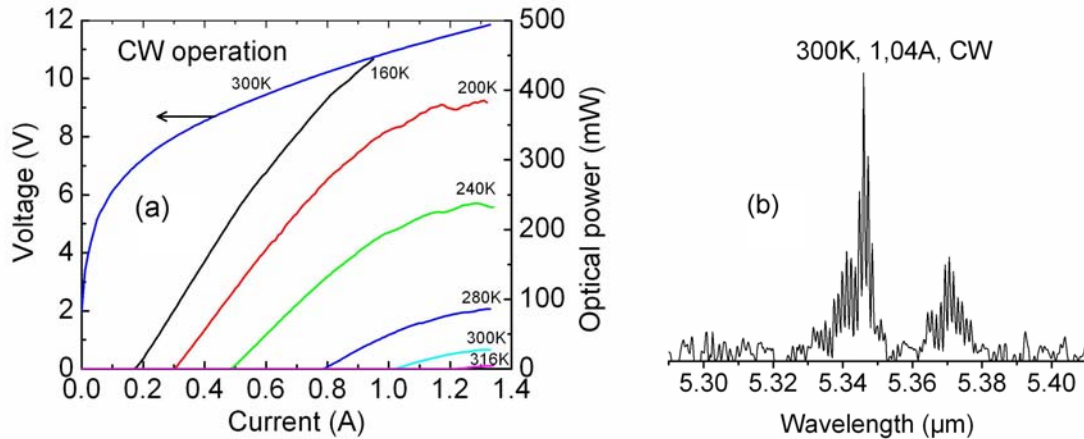


Figure 5.8 (a) CW L-I-V curves of a back facet HR coated, 3.5 mm long, 8.4 μm wide ridge waveguide QC laser (E107268B) with thick metal top contact at various heat sink temperatures. (b) A typical laser spectrum at 1.04 A and 300 K heat sink temperature.

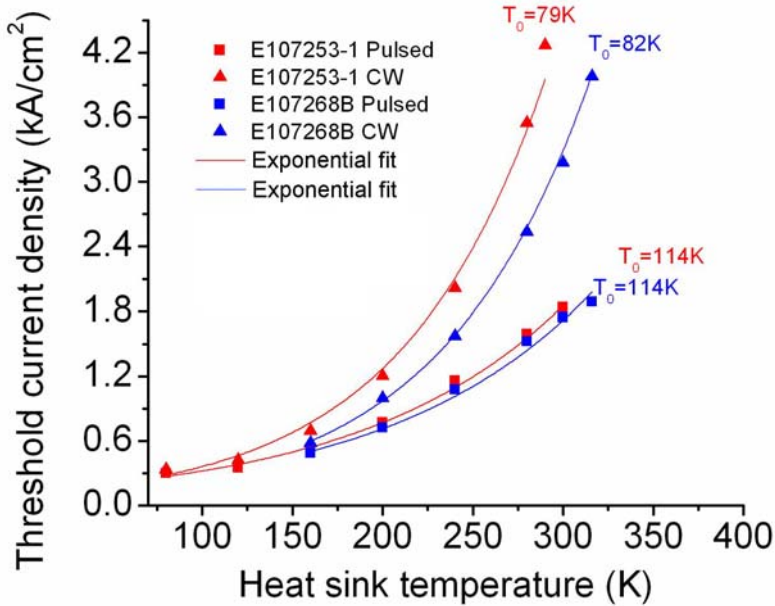


Figure 5.9 Threshold current density versus heat sink temperature of a back facet HR coated, 3.5 mm long, 8.4 μm wide ridge waveguide QC laser (E107268B) with thick metal top contact in both pulsed and CW operations. The data of first wafer E107253-1 (see Figure 5.6) are also given for comparison. The lower doped wafer(E107268B) has ~5% lower threshold in pulsed mode at 300 K.

these two wafers.

With further reduction of the doping levels in the active core for sample E107276F, there is a further increase of the laser performance as shown in Figure 5.10. A back facet HR coated, 3.5 mm long, 7.6 μm wide QC laser emits a CW power of ~100 mW at 300 K, and operates up to 360 K, which is another 44 K improvement compared to the second wafer E107268B. A typical CW spectrum is shown in Figure 5.10 (b). The laser wavelength is 5.36 μm , which is similar as that for the previous two samples. The laser threshold current density versus temperature is shown in Figure 5.11. The pulsed threshold increases from 0.26 kA/cm² at 80 K to 2.27 kA/cm² at 390 K, and the CW

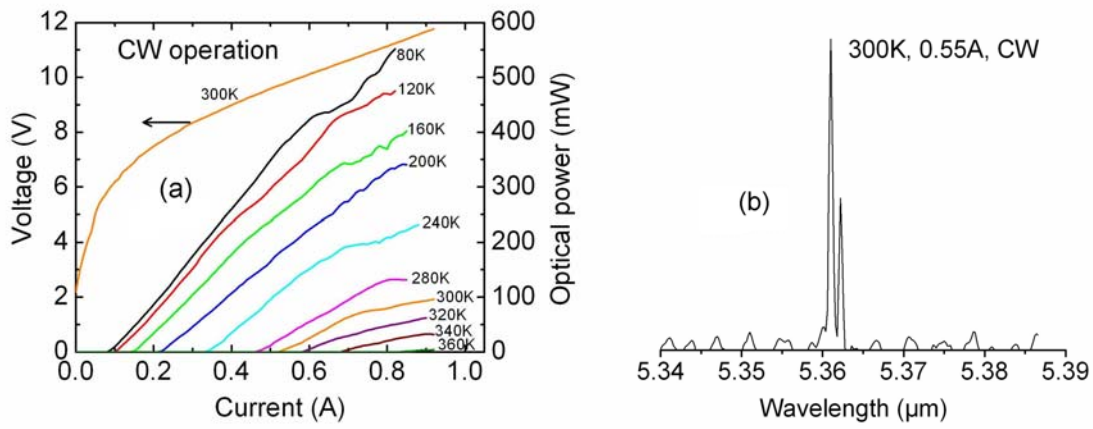


Figure 5.10 (a) CW L-I-V curves of a back facet HR coated, 3.5 mm long, 7.6 μm wide, ridge waveguide QC laser (E107276F) with thick metal top contact at various heat sink temperatures. (b) A typical laser spectrum at 0.55A and 300 K heat sink temperature.

threshold increases from 0.34 kA/cm² at 80 K to 3.16 kA/cm² at 360K. These threshold current densities are lower than those higher doped wafers E107253-1 and E107268B. The extracted characteristic temperature T_0 is 139 and 120K in pulsed mode and CW, respectively, which are larger than the values for samples E107253-1 and E107268B.

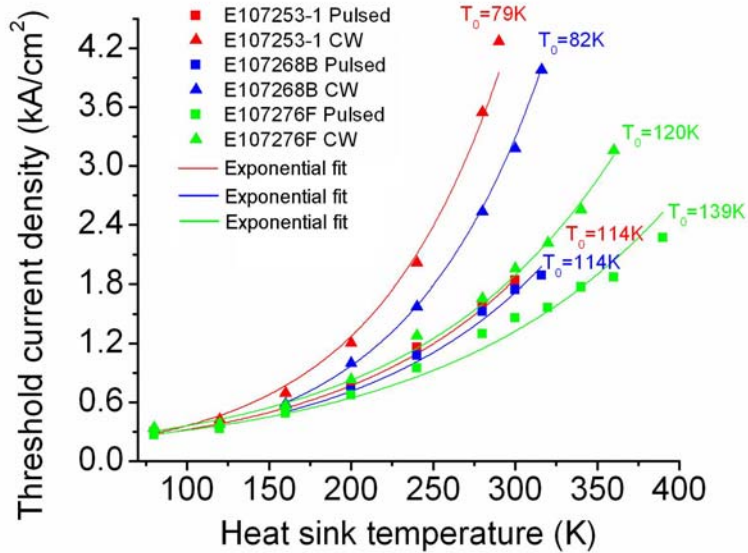


Figure 5.11 Threshold current density versus temperature of a back facet HR coated, 3.5 mm long, 7.6 μm wide ridge waveguide QC laser (E107276F) with thick metal top contact in both pulsed and CW operations. The data for wafers E107253-1 and E107268B are also given for comparison. The lowest doped wafer E107276F has 16% and 20% lower threshold in pulsed mode at 300 K, compared to higher doped wafers E107268B and E107253-1, respectively.

Using “1/L” method shown in Figure 5.12, the optical gain and waveguide loss for wafer E107276F are extracted. The gain coefficient at room temperature is 8.27 cm/kA, which is close to that for sample E105253-1 (with higher doping levels in both the cladding and active region). The waveguide loss is 6.48 cm^{-1} , which is 2.6 cm^{-1} lower than that for sample E107253-1 due to the reduced doping levels. This lower waveguide loss leads to the significant improvement of the laser performance as described above.

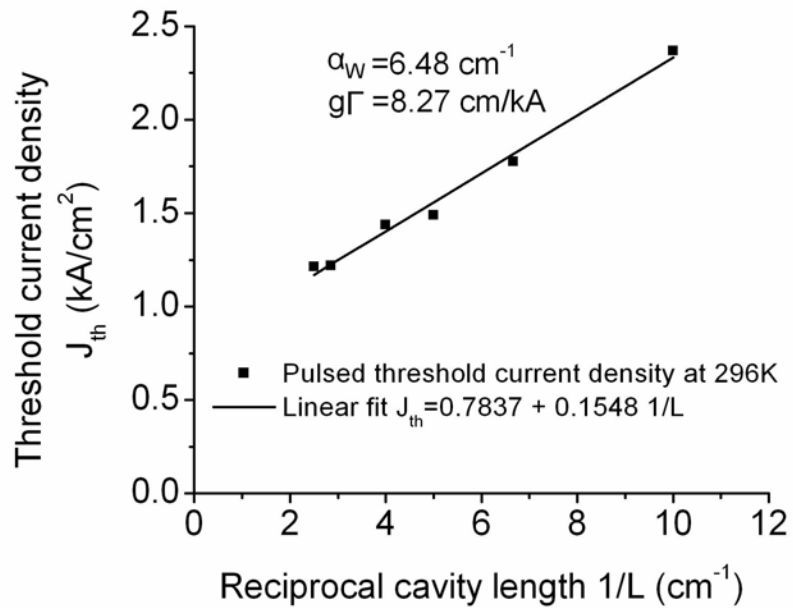


Figure 5.12 Pulsed threshold current density at 296 K versus reciprocal cavity length for QC lasers from wafer E107276F.

At this point, it is interesting to compare these three samples in order to examine the effects of doping level on QC laser performance. Table 5.1 lists the doping level and the measured laser performance of these three $\lambda \approx 5.3 \mu\text{m}$ QC laser samples. First by comparing samples E107253-1 and E107268B, we can examine the role of doping in the waveguide claddings. When the doping level in waveguide cladding layers is reduced from $1 \times 10^{17} \text{ cm}^{-3}$ (E107253-1) to $0.5 \times 10^{17} \text{ cm}^{-3}$ (E107268B), there is $\sim 5\%$ decrease in laser threshold current density, and 26 K increase in maximum CW operating temperature. This improvement is attributed to a lower free carrier absorption in the waveguide claddings resulting from the lower doping level. In addition, as the doping level in active regions and injectors for these two wafers are identical, the characteristic temperature T_0 remains the same as expected. Second, by comparing samples E107268B

and E107276F, we can examine the role of doping in the injectors of laser active core. When the doping level in the injectors of the laser active core is reduced from $1.8 \times 10^{17} \text{ cm}^{-3}$ (E107268B) to $0.9 \times 10^{17} \text{ cm}^{-3}$ (E107276F), there is $\sim 16\%$ decrease in laser threshold current density, 44 K increase in maximum CW operating temperature, and 25 K increase in characteristic temperature T_0 . This improvement is attributed to not only the reduced free carrier absorption in the active core, but also suppressed thermal backfilling and some other doping-dependent factors such as intersubband resonant absorption etc.. Third, from the measured waveguide loss α_W for samples E107253-1 and E107276F, we can see that the measured waveguide loss, i.e. $6.48\text{-}9.14 \text{ cm}^{-1}$, is again much higher than the calculated value from free carrier absorption, i.e. $1\text{-}1.67 \text{ cm}^{-1}$. Finally, since these reductions in doping level leads to continuing improvement in laser performance without noticing the depletion of electrons, a further optimization in the lower doping range ($< 9 \times 10^{16} \text{ cm}^{-3}$ in the injectors, and $< 5 \times 10^{16} \text{ cm}^{-3}$ in the InP cladding layers) is worthwhile.

Table 5.1 Summary of $\lambda \approx 5.3 \mu\text{m}$ QC lasers, relevant design parameters and experimental results.

Sample label	Doping in active core (10^{17} cm^{-3})	Doping in waveguide cladding (10^{17} cm^{-3})	$J_{th} @ 300\text{K}$ (kA/cm^2)	T_0, Pulsed (K)	$T_{max, \text{CW}}$ (K)	α_W (cm^{-1})
E107253-1	1.8	1	1.84	114	290	9.14
E107268B	1.8	0.5	1.74	114	316	
E107276F	0.9	0.5	1.46	139	360	6.48

5.4 Very Small Heat Dissipation, Room Temperature, CW QC Laser

One issue associated with the above high performance room temperature CW QC lasers is their large heat dissipation, which is usually larger than 4 W. Thus, reducing the thermal load is imperative in order to make portable compact QC laser systems for real-world applications. Very recently, using a low threshold material, a narrow ridge and a relatively short, 1.5 mm long cavity with back facet high reflectivity (HR) coated, Blaser et al. reported a room temperature, CW QC laser with heat dissipation less than 2 W [53]. Here, we use an even shorter 0.5 mm long cavity and HR coating on both laser facets to realize room temperature, CW operation at $\lambda \approx 5.3 \mu\text{m}$ with heat dissipation in the range of 1.2 - 1.7 W.

A 0.5 mm long QC laser from wafer E107276F is HR coated with $\text{SiO}_2/\text{Ti}/\text{Au}/\text{SiO}_2$ of thicknesses 350/15/150/100 and 350/15/11/100 nm, for its back and front facets, respectively. An optical image of this short cavity QC laser is shown in Figure 5.13. We estimated a reflectivity for this front facet as $\sim 75\%$ based on the threshold reduction before and after the coating. Figure 5.14 (a) shows the pulsed L-I-V curves for the 0.5 mm long laser with one facet and both facets HR coated at room temperature. The as-cleaved 0.5 mm long laser does not lase due to the large mirror loss. After adding the HR coating on its back facet, it lases with a threshold current density of 2.24 kA/cm^2 . After adding the second HR coating on its front facet, the pulsed laser threshold decreases to 1.16 kA/cm^2 . Figure 5.14 (b) shows the light-current curves of the laser with both facets HR coated in CW mode. It emits a maximum power of $\sim 1 \text{ mW}$ at 295 K with a CW threshold of 2.35 kA/cm^2 . Its heat dissipation is reduced to 1.13-1.64 W, which is ~ 5 times smaller than that of the conventional long cavity laser shown in Figure 5.10 (a).

With further improvements to lower the laser threshold, better laser packaging such as buried heterostructure fabrication with a narrower laser ridge, and epitaxial-side-down mounting, further reduction in heat dissipation in these lasers is expected, hence paving the way for the first essentially uncooled, room temperature, CW QC laser systems.

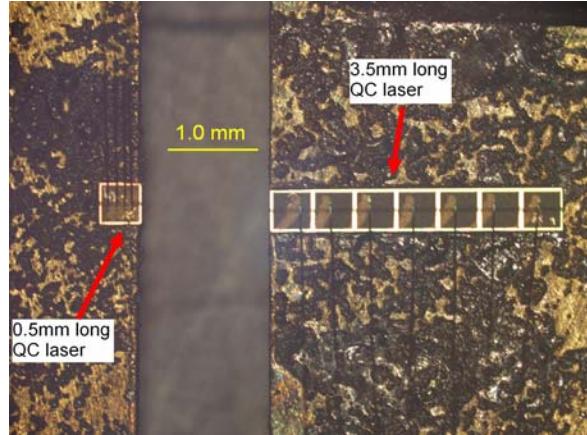


Figure 5.13 Optical images for a 0.5 mm long, epitaxial-side-up mounted QC laser (E107276F) with both facets HR coated. For comparison, a conventional 3.5 mm long, epitaxial-side-up mounted QC laser with back facet HR coated is also given.

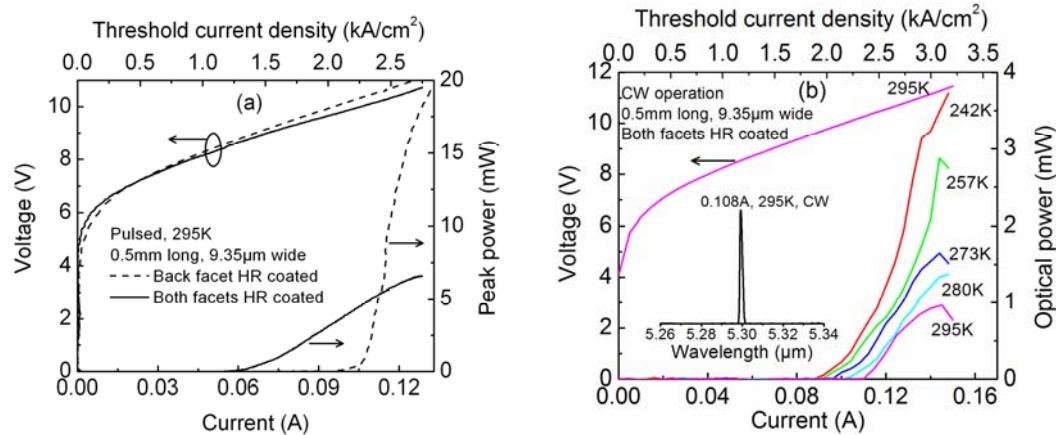


Figure 5.14 (a) Pulsed L-I-V curves for a 0.5 mm long, $9.35\text{ }\mu\text{m}$ wide QC laser (E107276F) with the back facet (dashed line) and both facets (solid line) HR coated at 295 K. (b) CW light-current curves of the laser with both facets HR coated at various heat sink temperatures. The voltage-current curve at 295 K is also given. The inset shows the laser spectrum at 295 K and 0.108 A.

5.5 Conclusion and Discussion

By using a strain-compensated active region design and reduced doping levels, high performance QC lasers were realized at $\lambda \approx 5.3 \text{ } \mu\text{m}$. A 3.5 mm long, back facet HR coated laser emits $\sim 100 \text{ mW}$ at room temperature, and its maximum CW operation temperature is $\sim 360 \text{ K}$. The gain coefficient was measured to be 7 - 8.3 cm/kA at room temperature, and the waveguide loss is reduced from 9.1 to 6.5 cm⁻¹ by reducing the doping levels.

In addition, by using a shorter 0.5 mm long cavity and HR coating on both laser facets, room temperature CW QC lasers were realized with a very low heat dissipation of 1.2-1.7 W, which is five times smaller than that of the conventional long cavity lasers and represents an effective approach to facilitate less complex laser cooling and the development of portable, essentially uncooled, mid-infrared sensor systems. With further optimization of the doping levels, and more advanced packaging of buried heterostructure and epitaxial-side-down mounting, further increase in laser performance can be achieved for these devices.

This collaboration with Corning Inc. also established their entry into QC laser field.

Chapter 6

Summary and Outlook

6.1 Summary of Current Work

At the start of this thesis work, the best performance of QC lasers in this research group was limited to CW operation up to ~ 160 K heat sink temperature at $\lambda \approx 8$ μm . The goal of this thesis was to reach room temperature, CW operation, access a wide spectral range through improved design, device processing and packaging of QC lasers. This thesis successfully realized room temperature, CW operation of QC lasers at wavelengths of 5.3 and 8.2-10.3 μm . In particular, the following sub-projects were accomplished.

Using an optimized active region design of a two phonon resonance extractor with a vertical transition, improved device packaging of ridge waveguide laser with thick metal top contact and buried heterostructure laser with thick metal top contact, high performance room temperature CW QC lasers at $\lambda \approx 8.2$ μm were realized, which includes the first MOCVD-grown room temperature, CW QC laser without the lateral wafer regrowth [49].

Using similar design strategies of a two phonon resonance with a vertical transition, room temperature CW operation was extended to the longer wavelengths between 9.6 and 10.3 μm within the second atmospheric window. In addition, QC lasers based on a new design of a two phonon resonance with a diagonal transition was developed at $\lambda \approx 9.8$ and 10.1 μm , which have a larger T_0 , but also a higher threshold as compared to the vertical transition lasers. A strong performance dependence on the laser ridge width was observed for these lasers, which is not yet fully understood. These QC lasers with

wavelengths from 8.2 to 10.3 μm were delivered to Pacific Northwestern National Laboratory (PNNL) for a DIMP sensor system based on Laser Photoacoustic Spectroscopy (L-PAS) technique.

A systematic study on the temperature-dependent optical gain and loss measurement was performed on the QC lasers between $\lambda \approx 8.2\text{-}10.3 \mu\text{m}$ by using Hakki-Paoli method [72]. Besides confirming the expected temperature-dependence and magnitude of the gain coefficient, the results indicate a 2-3 times higher waveguide loss than the calculated from free carrier absorption based on the Drude model. Different types of temperature-dependence of the waveguide loss were observed, which suggests another dominant loss origin such as intersubband resonant absorption inside the laser active core. We calculated that indeed a large portion of the loss can be explained in this way. By comparing the loss dependence on side-wall composition and ridge width, we excluded the side-wall (of relatively wide ridge) as sources of the additional loss.

Using a two phonon resonance with a vertical transition, reduced doping levels, high power, room temperature, CW QC lasers were realized at $\lambda \approx 5.3 \mu\text{m}$ based on strain-compensated InGaAs/AlInAs material. By reducing the doping levels by half in both the active core and waveguide claddings, the maximum CW operation temperature is increased from 290 to 360 K for 3.5 mm long, ridge waveguide lasers with thick metal top contact. A CW power of $\sim 100 \text{ mW}$ at room temperature was measured for a best device. Gain and loss measurement indicates a high gain coefficient of 7-8.3 cm/kA at room temperature, and a waveguide loss of 9.1 and 6.5 cm^{-1} for the high and low doped samples respectively. These lasers were developed for automotive and environmental sensors. Additionally, by using a shorter 0.5 mm long cavity with both facets HR coated

with $\sim 95\%$ and 75% reflectivities, respectively, very low heat dissipation of $1.2 - 1.7$ W, room temperature, CW QC lasers were realized, which represents an effective approach to fabricate portable essentially uncooled QC laser systems [54].

6.2 Future Work

QC laser technology is evolving with a rapid pace since the laser invention in 1994, and high power, room temperature, CW operation has been realized in a short history of less than 10 years. With further innovations and optimizations in laser design, material growth, and device packaging, we expect even better laser performance, which enables high power, uncooled, portable QC laser sources suitable for many real-world applications in the environment, health, security, process control and others. Learning from what has been done in this thesis, the following are possible research projects, and should be undertaken to further increase QC laser performance.

1. Optimization of the QC laser active regions

For the active region design based on a two phonon resonance extractor as those used in high performance QC lasers discussed here, there are parasitic higher lying energy levels in the active region, which can potentially induce electron leakage paths and result in extra loss through intersubband absorption. Therefore eliminating those parasitic levels in the active region design will help to improve the electron injection efficiency and lower the waveguide loss. To better identify these detrimental continuum states, more refined semiconductor band structure models are needed, as well as a better knowledge of material parameters. In addition, other novel design scheme with higher gain coefficient

will also help to increase the QC laser performance, such as the excited-state QC lasers, which have a larger dipole matrix element [81].

2. Doping level optimization

As seen from the $\lambda \approx 5.3 \mu\text{m}$ QC laser samples, reducing the doping levels leads to a lower waveguide loss and consequently a significant increase in the laser performance. Further performance improvement can be expected for further reduced doping levels. However, as the maximum injection current is proportional to the doping level, a certain doping level must be maintained before the electrons are depleted [82, 83]. Therefore further doping optimization is needed, as well as understanding of how the optimum doping level depends on the design.

3. Further understanding and control of the waveguide loss

For all the QC lasers discussed in this thesis from $\lambda \approx 5.3 - 10.3 \mu\text{m}$, their waveguide loss is systematically higher than the one calculated from plain free carrier absorption. This is even independent of growth method and source, as our laser materials were provided from four different growers. Therefore further studies to identify other loss origins including intersubband resonant absorption, roughness scattering, defect state absorption, etc. are needed to better understand the waveguide loss and in turn find ways to reduce the waveguide loss.

4. Better device packaging

The high performance QC lasers discussed in this work were practically all epitaxial-side-up mounted. Epitaxial-side-down mounting will lead to more efficient heat

dissipation, and thus a further increase in the laser performance. The epitaxial-side-down mounting has been realized by several groups [12, 51, 62, 84, 85]. However, to enable simple, reliable mounting, further technical improvements need to be made.

Also, for the QC lasers discussed in this work, the wet-etched laser ridge shows some variation in ridge width in the cross-plane direction (typical width on the bottom of the active core is larger than that on the top by $\sim 30\%$), which results in an uneven gain distribution across the laser gain region. An improvement to fabricate an ideal vertical laser ridge will give some improvement in the laser performance.

Finally, the thermoelectric materials provide an active way of device cooling based on Peltier effect [86]. The integration of thermoelectric materials into QC lasers may provide a more efficient laser packaging and cooling as it can slow the otherwise all positive thermal feedback loops and thermal runaway.

Bibliography

- [1] R. F. Kazarinov, and R. A. Suris, *Fiz. Tekh. Poluprovodn.*, **5**, 797 (1971)
- [2] F. Capasso, Band-gap engineering via graded gap, superlattice, and periodic doping structures: applications to novel photodetectors and other devices, *J. Vac. Sci. Technol. B*, **1**, 457 (1982)
- [3] A. Y. Cho, Advances in molecular beam epitaxy (MBE), *J. Crystal Growth*, **111**, 1 (1991)
- [4] J. Faist, F. Capasso, D. L. Sivco, C. Sirtori, A. L. Hutchinson, and A. Y. Cho, Quantum Cascade laser, *Science*, **264**, 553 (1994)
- [5] J. Faist, C. Gmachl, F. Capasso, C. Sirtori, D. L. Sivco, J. N. Baillargeon and A. Y. Cho, Distributed feedback quantum cascade lasers, *Appl. Phys. Lett.*, **70**, 2670 (1997)
- [6] C. Gmachl, F. Capasso, E. E. Narimanov, J. U. Nockel, A.D. Stone, J. Faist, D. L. Sivco and A. Y. Cho, High-power directional emission from microlasers with chaotic resonators, *Science*, **280**, 1556 (1998)
- [7] C. Gmachl, D. L. Sivco, R. Colombelli, F. Capasso and A. Y. Cho, Ultra-broadband semiconductor laser, *Nature*, **415**, 883 (2002)
- [8] R. Kohler, A. Tredicucci, F. Beltram, H. E. Beere, E. H. Linfield, A. G. Davies, D. A. Ritchie, R. C. Iotti , and F. Rossi, Terahertz semiconductor-heterostructure laser, *Nature*, **417**, 156 (2002)
- [9] B. S. Williams, H. Callebaut, S. Kumar, and Q. Hu, 3.4-THz quantum cascade laser based on longitudinal-optical-phonon scattering for depopulation, *Appl. Phys. Lett.*, **82**, 1015 (2003)

- [10] N. Owschimikow, C. Gmachl, A. Belyanin, V. Kocharovsky, D. L. Sivco, R. Colombelli, F. Capasso, A. Y. Cho, Resonant second-order nonlinear optical processes in quantum cascade lasers, *Phys. Rev. Lett.*, **90**, 043902-1 (2003)
- [11] C. Gmachl, A. Belyanin, D. L. Sivco, M. L. Peabody, N. Owschimikow, A. M. Sergent, F. Capasso, A. Y. Cho, Optimized second-harmonic generation in quantum cascade lasers, *IEEE J. Quantum Electron.*, **39**, 1345 (2003)
- [12] M. Beck, D. Hofstetter, T. Aellen, J. Faist, U. Oesterle, M. Ilegems, E. Gini, and H. Melchior, Continuous wave operation of a midinfrared semiconductor laser at room temperature, *Science*, **295**, 301 (2002)
- [13] J. S. Yu, S. Slivken, A. Evans, L. Doris, and M. Razeghi, High-Power Continuous-Wave Operation of a 6 μm Quantum-Cascade Laser at Room Temperature, *Appl. Phys. Lett.*, **83**, 2503 (2003)
- [14] J. S. Roberts, R. P. Green, L. R. Wilson, E. A. Zibik, D. G. Revin, J. W. Cockburn, and R. J. Airey, Quantum cascade lasers grown by metalorganic vapor phase epitaxy, *Appl. Phys. Lett.*, **82**, 4221 (2003)
- [15] C. Sirtori, P. Kruck, S. Barbieri, P. Collot, J. Nagle, M. Beck, J. Faist, U. Oesterle, GaAs/Al_XGa_{1-X}As quantum cascade lasers, *Appl. Phys. Lett.*, **73**, 3486 (1998)
- [16] J. Devenson, R. Teissier, O. Cathabard, and A. N. Baranov, InAs/AlSb quantum cascade lasers emitting below 3 μm , *Appl. Phys. Lett.*, **90**, 111118-1 (2007)
- [17] R. Martini, C. Gmachl, J. Falciglia, F.G. Curti, C.G. Bethea, F. Capasso, E.A. Whittaker, R. Paiella, A. Tredicucci, A.L. Hutchinson, D.L. Sivco and A.Y. Cho, High-speed modulation and free-space optical audio/video transmission using quantum cascade lasers, *Electron. Lett.*, **37**, 191 (2001)

- [18] A. A. Kosterev, and F. K. Tittel, Chemical Sensors Based on Quantum Cascade Lasers, *IEEE J. Quantum Electron.*, **38**, 582 (2002)
- [19] R. Jiménez, M. Taslakov, V. Simeonov, B. Calpini, F. Jeanneret, D. Hofstetter, M. Beck, J. Faist, H. Van Den Bergh, Ozone detection by differential absorption spectroscopy at ambient pressure with a 9.6 μm pulsed quantum-cascade laser, *Appl. Phys. B*, **78**, 249 (2004)
- [20] M. Pushkarsky, A. Tsekoun, I. G. Dunayevskiy, R. Go, and C. K. N. Patel, Sub-parts-per-billion level detection of NO₂ using room-temperature quantum cascade lasers, *Proc. Natl. Acad. Sci. USA*, **103**, 10846 (2006)
- [21] M. B. Filho, M. G. da Silva, M. S. Sthel, D. U. Schramm, H. Vargas, A. Miklós, and P. Hess, Ammonia detection by using quantum-cascade laser photoacoustic spectroscopy, *Appl. Opt.*, **45**, 4966 (2006)
- [22] J. Faist, F. Capasso, C. Sirtori, D. L. Sivco, and A. Y. Cho, Quantum cascade lasers, in Intersubband Transitions in Quantum Wells: Physics and Device Applications II, Edited by H. C. Liu and F. Capasso (Academic, San Diego, 2000), pp. 1-83
- [23] R. Ferreira and G. Bastard, Evaluation of some scattering times for electrons in unbiased and biased single- and multiple-quantum-well structures, *Phys. Rev. B*, **40**, 1074 (1989)
- [24] J. Faist, F. Capasso, C. Sirtori, D. L. Sivco, J. N. Baillargeon, A. L. Hutchinson, S. N. G. Chu, and Al. Y. Cho, High power mid-infrared ($\lambda \sim 5\mu\text{m}$) quantum cascade lasers operating above room temperature, *Appl. Phys. Lett.*, **68**, 3680 (1996)

- [25] G. Scamarcio, F. Capasso, C. Sirtori, J. Faist, A. L. Hutchinson , D. L. Sivco, A. Y. Cho, High-power infrared (8-micrometer wavelength) superlattice lasers, *Science*, **276**, 773 (1997)
- [26] J. Faist, M. Beck, T. Aellen, and E. Gini, Quantum-cascade lasers based on a bound-to-continuum transition, *Appl. Phys. Lett.*, **78**, 147 (2001)
- [27] D. Hofstetter, M. Beck, T. Aellen, J. Faist, U. Oesterle, M. Illegems, E. Gini, and H. Melchior, Continuous wave operation of a 9.3 μm quantum cascade laser on a Peltier cooler, *Appl. Phys. Lett.*, **78**, 1964 (2001)
- [28] J. Faist, F. Capasso, C. Sirtori, D. L. Sivco, A. L. Hutchinson, and A. Y. Cho, Laser Action by Tuning the Oscillator Strength, *Nature*, **386**, 777 (1997)
- [29] C. Gmachl, F. Capasso, D. L. Sivco, and A. Y. Cho, Recent progress in quantum cascade lasers and applications, *Rep. Prog. Phys.*, **64**, 1533 (2001)
- [30] M. A. Ordal, L. L. Long, R. J. Bell, S. E. Bell, R. W. Jr. Alexander, and C. A. Ward, Optical properties of the metals Al, Co, Cu, Au, Fe, Pb, Ni, Pd, Pt, Ag, Ti, and W in the infrared and far infrared, *Appl. Opt.*, **22**, 1099 (1983)
- [31] J. Chilwell, and I. Hodgkinson, Thin-films field-transfer matrix theory of planar multilayer waveguides and reflection from prism-loaded waveguides, *J. Opt. Soc. Am. A*, **1**, 742 (1984)
- [32] C. Sirtori, J. Faist, F. Capasso, D. L. Sivco, A. L. Hutchinson, and A. Y. Cho, Quantum cascade laser with plasmon-enhanced waveguide operating at 8.4 μm wavelength, *Appl. Phys. Lett.*, **66**, 3242 (1995)

- [33] R. Colombelli, F. Capasso, C. Gmachl, A. L. Hutchinson, D. L. Sivco, A. Tredicucci, M. C. Wanke, A. M. Sergent, and A. Y. Cho, Far-infrared surface-plasmon quantum-cascade lasers at $21.5 \mu\text{m}$ and $24 \mu\text{m}$ wavelengths, *Appl. Phys. Lett.*, **78**, 2620 (2001)
- [34] J. Faist, C. Sirtori, F. Capasso, D. L. Sivco, J. N. Baillargeon, A. L. Hutchinson, and A. Y. Cho, High-power long-wavelength ($\lambda \sim 11.5 \mu\text{m}$) quantum cascade lasers operating above room temperature, *IEEE Photon. Technol. Lett.*, **10**, 1100 (1998)
- [35] S. S. Howard, Z. Liu, D. Wasserman, A. J. Hoffman, T. S. Ko, and C. F. Gmachl, High-performance Quantum Cascade lasers: optimized design through waveguide and thermal modeling, *IEEE J. Sel. Topics Quantum Electron.*, **13**, 1054 (2007)
- [36] J. Faist, A. Tredicucci, F. Capasso, C. Sirtori, D. L. Sivco, J. N. Baillargeon, A. L. Hutchinson, and A. Y. Cho, High-power continuous-wave quantum cascade lasers, *IEEE J. Quantum Electron.*, **34**, 336 (1998)
- [37] J.S. Yu, A. Evans, S. Slivken, S.R. Darvish and M. Razeghi, Temperature dependent characteristics of $\lambda \sim 3.8 \mu\text{m}$ room-temperature continuous-wave quantum-cascade lasers, *Appl. Phys. Lett.*, **88**, 251118-1 (2006)
- [38] J.S. Yu, S.R. Darvish, A. Evans, J. Nguyen, S. Slivken, and M. Razeghi, Room-temperature continuous-wave operation of quantum-cascade lasers at $\lambda \sim 4 \mu\text{m}$, *Appl. Phys. Lett.* **88**, 041111-1 (2006)
- [39] J.S. Yu, A. Evans, S. Slivken, S.R. Darvish, and M. Razeghi, Short wavelength ($\lambda \sim 4.3 \mu\text{m}$) high-performance continuous-wave quantum-cascade lasers, *IEEE Photon. Technol. Lett.*, **17**, 1154 (2005)

- [40] J.S. Yu, S. Slivken, S.R. Darvish, A. Evans, B. Gokden and M. Razeghi, High-power, room-temperature and continuous-wave operation of distributed-feedback quantum-cascade lasers at $\lambda = 4.8 \mu\text{m}$, *Appl. Phys. Lett.*, **87**, 041104-1 (2005)
- [41] A. Evans, J. Nguyen, S. Slivken, J.S. Yu, S.R. Darvish, and M. Razeghi, Quantum-cascade lasers operating in continuous-wave mode above 90°C at $\lambda \sim 5.25 \mu\text{m}$, *Appl. Phys. Lett.*, **88**, 051105-1 (2006)
- [42] S.R. Darvish, W. Zhang, A. Evans, J.S. Yu, S. Slivken, and M. Razeghi, High-power continuous-wave operation of distributed-feedback quantum-cascade lasers at $\lambda \sim 7.8 \mu\text{m}$, *Appl. Phys. Lett.*, **89**, 251119-1 (2006)
- [43] J.S. Yu, S. Slivken, A. Evans, S.R. Darvish, J. Nguyen, and M. Razeghi, High-power $\lambda \sim 9.5 \mu\text{m}$ quantum-cascade lasers operating above room temperature in continuous-wave mode, *Appl. Phys. Lett.*, **88**, 091113-1 (2006)
- [44] S. Slivken, A. Evans, W. Zhang and M. Razeghi, High-power, continuous-operation intersubband laser for wavelengths greater than 10 micron, *Appl. Phys. Lett.*, **90**, 151115-1 (2007)
- [45] M. Troccoli, S. Corzine, D. Bour, J. Zhu, O. Assayag, L. Diehl, B. G. Lee, G. Hofler, and F. Capasso, Room temperature continuous-wave operation of quantum-cascade lasers grown by metal organic vapor phase epitaxy, *Electron. Lett.*, **41**, 1059 (2005)
- [46] L. Diehl, D. Bour, S. Corzine, J. Zhu, G. Hofler, M. Loncar, M. Troccoli, and F. Capasso, High-temperature continuous wave operation of strain-balanced quantum cascade lasers grown by metal organic vapor-phase epitaxy *Appl. Phys. Lett.*, **89**, 081101-1 (2006)

- [47] L. Diehl, D. Bour, S. Corzine, J. Zhu, G. Hofler, M. Loncar, M. Troccoli, and F. Capasso, High-power quantum cascade lasers grown by low-pressure metalorganic vapor-phase epitaxy operating in continuous wave above 400 K, *Appl. Phys. Lett.*, **88**, 201115-1 (2006)
- [48] C. Pflugl, L. Diehl, A. Tsekoun, R. Go, C. K. N. Patel, X. Wang, J. Fan, T. Tanbun-Ek and F. Capasso, Room-temperature continuous-wave operation of long wavelength ($\lambda = 9.5 \text{ um}$) MOVPE-grown quantum cascade lasers, *Electron. Lett.*, **43**, 2162 (2007)
- [49] Z. Liu, D. Wasserman, S. S. Howard, A. J. Hoffman, C. F. Gmachl, X. Wang, T. Tanbun-Ek, L. Cheng, and F.-S. Choa, Room-temperature continuous-wave quantum cascade lasers grown by MOCVD without lateral regrowth, *IEEE Photon. Technol. Lett.*, **18**, 1347 (2006)
- [50] O. Malis, D. L. Sivco, J. Chen, L. Zhang, A. M. Sergent, Z. Liu, and C. Gmachl, Optimization of InP-based waveguides for high-performance mid-infrared quantum cascade lasers, *28th International Conference on the Physics of Semiconductors*, **893**, 1453 (2007)
- [51] X. Wang, J. Y. Fan, T. Tanbun-Ek, and F.-S. Choa, Low threshold quantum-cascade lasers of room temperature continuous-wave operation grown by metal-organic chemical-vapor deposition, *Appl. Phys. Lett.*, **90**, 211103-1 (2007)
- [52] K. Fujita, S. Furuta, A. Sugiyama, T. Ochiai, T. Edamura, N. Akikusa, M. Yamanishi, and H. Kan, Room temperature, continuous-wave operation of quantum cascade lasers with single phonon resonance-continuum depopulation structures grown by metal organic vapor-phase epitaxy, *Appl. Phys. Lett.*, **91**, 141121-1 (2007)

- [53] S. Blaser, A. Bachle, S. Jochum, L. Hvozdara, G. Vandeputte, S. Brunner, S. Hansmann, A. Muller, and J. Faist, Low-consumption (below 2 W) continuous-wave singlemode quantum-cascade lasers grown by metal-organic vapour-phase epitaxy, *Electron. Lett.*, **43**, 1201 (2007)
- [54] Z. Liu, C. F. Gmachl, C. G. Caneau, and C. Zah, Very small (\leq 1.2-1.7 W) heat dissipation, room temperature, continuous-wave quantum cascade lasers at $\lambda \sim$ 5.3 μm , *Conference on Lasers and Electro-Optics (CLEO)* (2008)
- [55] A. Wittmann, T. Gresch, E. Gini, L. Hvozdara, N. Hoyler, M. Giovannini, J. Faist, High-performance bound-to-continuum quantum-cascade lasers for broad-gain applications, *IEEE J. Quantum Electron.*, **44**, 36 (2008)
- [56] “COMSOL Multiphysics”, COMSOL, Inc. www.comsol.com
- [57] Landolt-Börnstein Tables, edited by O. Madelung, M. Schultz, and H. Weiss ~Springer, Berlin, Group III, Vol. 17a, (1982)
- [58] S. Huxtable, A. Shakouri, P. Abraham, Y.-J. Chiu, X. Fan, J. E. Bowers, and A. Majumdar, Thermal Conductivity of Indium Phosphide Based Superlattices, 18th International Conference on Thermoelectrics, 594 (1999)
- [59] A. Lops, V. Spagnolo, and G. Scamarcio, Thermal modeling of GaInAs/AlInAs quantum cascade lasers, *J. Appl. Phys.*, **100**, 043109 (2006)
- [60] V. Spagnolo, M. Troccoli, and G. Scamarcio, C. Gmachl, F. Capasso, A. Tredicucci, A. M. Sergent, A. L. Hutchinson, D. L. Sivco, and A. Y. Cho, Temperature profile of GaInAs/AlInAs/InP quantum cascade-laser facets measured by microprobe photoluminescence, *Appl. Phys. Lett.*, **78**, 2095 (2001)

- [61] A. Lops, V. Spagnolo, and G. Scamarcio, Thermal modeling of GaInAs/AlInAs quantum cascade lasers, *J. Appl. Phys.*, **100**, 043109-1 (2006)
- [62] C. Gmachl, A. M. Sergent, A. Tredicucci, F. Capasso, A. L. Hutchinson, D. L. Sivco, J. N. Baillargeon, S. N. G. Chu, and A. Y. Cho, Improved CW operation of quantum cascade lasers with epitaxial-side heat-sinking, *IEEE Photon. Technol. Lett.*, **11**, 1369 (1999)
- [63] M. Beck, J. Faist U. Oesterle, M. Ilegems, E. Gini, and H. Melchior, Buried Heterostructure Quantum Cascade Lasers with a Large Optical Cavity Waveguide, *IEEE Photon. Technol. Lett.*, **12**, 1450 (2000)
- [64] F. Capasso, C. Gmachl, D. L. Sivco, and A. Y. Cho, Quantum cascade lasers, *Physics World*, **12**, pp. 27 (1999)
- [65] F.-S. Choa., L. Cheng, X. Ji, Z. Liu, D. Wasserman, S. S. Howard, C. F. Gmachl, X. Wang, J. Fan, and J. Khurgin, MOCVD growth and regrowth of quantum cascade lasers, *Proc. SPIE*, **6485**, 64850 (2007)
- [66] A. A. Kosterev, Yu. A. Bakhirkin, R. F. Curl, and F. K. Tittel, Quartz-enhanced photoacoustic spectroscopy, *Opt. Lett.*, **27**, 1902 (2002)
- [67] R. Lewicki, G. Wysocki, A. A. Kosterev, and F. K. Tittel, QEPAS based detection of broadband absorbing molecules using a widely tunable, cw quantum cascade laser at 8.4 μm . *Opt. Express.*, **15**, 7357 (2007)
- [68] G. Laufer, and A. Ben-David, Optimized differential absorption radiometer for remote sensing of chemical effluents, *Appl. Opt.*, **41**, 2263 (2002)

- [69] S. Slivken, J. S. Yu, A. Evans, J. David, L. Doris, and M. Razeghi, Ridge-Width Dependence on High-Temperature Continuous-Wave Quantum-Cascade Laser Operation, *IEEE Photon. Technol. Lett.*, **16**, 744 (2004)
- [70] “BeamPROP,” Rsoft Design Group, Inc. www.rsoftdesign.com
- [71] B. W. Hakki, and T. L. Paoli, Gain spectra in GaAs double-heterostructure injection lasers, *J. Appl. Phys.*, **46**, 1299 (1975)
- [72] Z. Liu, C. F. Gmachl, L. Cheng, F.-S. Choa, F. J. Towner, X. Wang, and J. Fan, Temperature dependence of optical gain and loss in $\lambda \approx 8.2\text{-}10.2 \mu\text{m}$ quantum cascade lasers, *IEEE J. Quantum Electron.* (in print)
- [73] T. Gresch, M. Giovannini, N. Hoyler, and J. Faist, Quantum cascade lasers with large optical waveguides, *IEEE Photon. Technol. Lett.*, **18**, 544 (2006)
- [74] C. Gmachl, H. Y. Hwang, R. Paiella, D. L. Sivco, J. N. Baillargeon, F. Capasso, and A. Y. Cho, Quantum Cascade Lasers with Low-Loss Chalcogenide Lateral Waveguides, *IEEE Photon. Technol. Lett.*, **13**, 182 (2001)
- [75] T. Matsuoka, E. Kobayashi, K. Taniguchi, C. Hamaguchi, and S. Sasa, Temperature dependence of electron mobility in InGaAs/InAlAs heterostructures, *Jpn. J. Appl. Phys.*, **29**, 2017 (1990)
- [76] W. Walukiewicz, J. Lagowski, L. Jastrzebski, P. Rava, M. Lichtensteiger, C. H. Gatos, and H. C. Gatos, Electron mobility and free-carrier absorption in InP; determination of the compensation ratio, *J. Appl. Phys.*, **51**, 2659 (1980)
- [77] H. C. Liu, and F. Capasso, Intersubband Transitions in Quantum Wells, Physics and Device Application I, Semiconductor and Semimetals, (Academic Press, San Diego), **62**, 11 (2000)

- [78] M. S. Vitiello, G. Scamarcio, V. Spagnolo, D. G. Revin, J. Cockburn, M. J. Steer, and R. J. Airey, Electronic spatial distribution of $\text{In}_{0.53}\text{Ga}_{0.47}\text{As}/\text{AlAs}_{0.56}\text{Sb}_{0.44}$ quantum-cascade lasers, *J. Appl. Phys.*, **98**, 086106-1 (2005)
- [79] J. Faist, F. Capasso, D. L. Sivco, A. L. Hutchinson, S. N. G. Chu, and A. Y. Cho, Short wavelength $\lambda \sim 3.4\mu\text{m}$ quantum cascade laser based on strained compensated InGaAs/AlInAs, *Appl. Phys. Lett.*, **72**, 680 (1998)
- [80] C. G. Van de Walle, Band lineups and deformation potentials in the model-solid theory, *Phys. Rev. B*, **39**, 1871 (1989)
- [81] K. J. Franz, D. Wasserman, A. J. Hoffman, D. C. Jangraw, K.-T. Shiu, S. R. Forrest, and C. Gmachl, Evidence of cascaded emission in a dual-wavelength quantum cascade laser, *Appl. Phys. Lett.*, **90**, 091104-1 (2007)
- [82] M. Giehler, R. Hey, H. Kostial, S. Cronenberg, T. Ohtsuka, L. Schrottke, and H. T. Grahn, Lasing properties of GaAs/(Al,Ga)As quantum-cascade lasers as a function of injector doping density, *Appl. Phys. Lett.*, **82**, 671 (2003)
- [83] T. Aellen, M. Beck, N. Hoyler, M. Giovannini, and J. Faist, Doping in quantum cascade lasers. I. InAlAs–InGaAs/InP midinfrared devices, *J. Appl. Phys.*, **100**, 043101-1 (2006)
- [84] A. Tsekoun, R. Go, M. Pushkarsky, M. Razeghi, and C. K. N. Patel, Improved performance of quantum cascade lasers through a scalable, manufacturable epitaxial-side-down mounting process, *Proc. Natl. Acad. Sci. USA*, **103**, 4831 (2006)
- [85] A. Evans, S.R. Darvish, S. Slivken, J. Nguyen, Y. Bai and M. Razeghi, Buried heterostructure quantum cascade lasers with high continuous-wave wall plug efficiency, *Appl. Phys. Lett.*, **91**, 071101-1 (2007)

- [86] R. A. Taylor, G. L. Solbrekken, Optimization of thermoelectric cooling for microelectronics, *10th Intersociety Conference on Thermal and Thermomechanical Phenomena and Emerging Technologies in Electronic Systems*, 483 (2006)

List of Publications

Journal publications

1. **Zhijun Liu**, Claire F. Gmachl, Catherine G. Caneau, and Chung-en Zah, Very small heat dissipation, room temperature, continuous-wave quantum cascade lasers at $\lambda \sim 5.3$ μm (in preparation)
2. **Zhijun Liu**, Claire F. Gmachl, Liwei Cheng, Fow-Sen Choa, Fred J. Towner, Xiaojun Wang, and Jenyu Fan, Temperature Dependence of Optical Gain and Loss in $\lambda \approx 8.2$ - 10.2 μm Quantum Cascade Lasers, *IEEE Journal of Quantum Electronics*, 2008 (in print)
3. Scott S. Howard, **Zhijun Liu**, and Claire F. Gmachl, Thermal and Stark-effect Roll-over of Quantum Cascade Lasers, *IEEE Journal of Quantum Electronics*, vol. 44, no.4, p 319-323, 2008
4. Scott S. Howard, **Zhijun Liu**, Daniel Wasserman, Anthony Hoffman, Tiffany Ko, and Claire F. Gmachl, High-Performance Quantum Cascade Lasers: Optimized Design through Waveguide and Thermal Modeling. *IEEE Journal of Selected Topics in Quantum Electronics*, vol. 13, no. 5, p 1054-1064, 2007
5. Afusat O. Dirisu, Grace Silva, **Zhijun Liu**, Claire F. Gmachl, Fred J. Towner, John Bruno, and Deborah L. Sivco, Reduction of Facet Reflectivity of Quantum Cascade Lasers with Subwavelength Gratings, *IEEE Photonics Technology Letters*, vol. 19, no. 4, p 221-223, 2007
6. Shanshan Song, Scott S. Howard, **Zhijun Liu**, Afusat O. Dirisu, Claire F. Gmachl, and Craig B. Arnold, Mode Tuning of Quantum Cascade Lasers through Optical

Processing of Chalcogenide Glass Claddings, *Applied Physics Letters*, vol. 89, Issue 4, p 041115-1-041115-3, 2006

7. **Zhijun Liu**, Daniel Wasserman, Scott S. Howard, Anthony J. Hoffman, Claire F. Gmachl, Xiaojun Wang, Tawee Tanbun-Ek, Liwei Cheng, and Fow-Sen Choa, Room Temperature Continuous-wave Quantum Cascade Lasers Grown by MOCVD Without Lateral Regrowth, *IEEE Photonics Technology Letters*, vol. 18, no. 12, p 1347-1349, 2006
8. Jian Z. Chen, **Zhijun Liu**, Yisa S. Rumala, Deborah L. Sivco, and Claire F. Gmachl, Direct liquid cooling of room-temperature operated quantum cascade lasers, *Electronics Letters*, vol 42, no 9, p 534- 535, 2006
9. Jian Z. Chen, **Zhijun Liu**, Claire F. Gmachl, and Deborah L. Sivco, Silver halide fiber-based evanescent-wave liquid droplet sensing with room temperature mid-infrared quantum cascade lasers, *Optics Express*, vol. 13, no. 16, p 5953-5960, 2005

Conference publications

1. **Zhijun Liu**, Claire F Gmachl, Catherine G Caneau, and Chung-en Zah, Very Small (\leq 1.2 – 1.7 W) Heat Dissipation, Room Temperature, Continuous-Wave Quantum Cascade Lasers at $\lambda \sim 5.3 \mu\text{m}$, *Conference on Lasers and Electro-Optics (CLEO), San Jose, CA*, May 4-9, 2008
2. **Zhijun Liu**, Claire Gmachl, Liwei Cheng, Fow-Sen Choa, Fred J. Towner, Xiaojun Wang, and Jenyu Fan, Temperature-dependent Gain and Loss in Room-temperature Continuous-wave Quantum Cascade Lasers between 8.2-10.3 μm , *The Ninth*

International Conference on Intersubband Transitions in Quantum Wells (ITQW),

September 9-14 2007, Ambleside, Cumbria, UK

3. Fow-Sen Choa, Liwei Cheng, Xiaoming Ji, **Zhijun Liu**, Daniel Wasserman, Scott S. Howard, Claire F. Gmachl, Xiaojun Wang, Jenu Fan, and Jacob Khurgin, MOCVD growth and regrowth of quantum cascade lasers, *Proceedings of SPIE*, Volume: 6485, Editor(s): Carmen Mermelstein, David P. Bour, Feb. 2007
4. **Zhijun Liu**, Grace Silva, Jayson Paulose, Claire Gmachl, Liwei Cheng, Fow-Sen Choa, Rich Leavitt, Fred J. Towner, Xiaojun Wang, and Jenu Fan, Temperature-dependent Gain and Loss in High Performance Quantum Cascade Lasers at 8.2 and 10.3 μ m, *Conference on Lasers and Electro-Optics (CLEO), Baltimore, MD*, May 8-10, 2007
5. Scott S. Howard, **Zhijun Liu**, and Claire F. Gmachl, Analysis of the Thermal Roll-Over of Quantum Cascade Lasers, *Conference on Lasers and Electro-Optics (CLEO), Baltimore, MD*, May 8-10, 2007
6. Tiffany Ko, **Zhijun Liu**, and Claire Gmachl, Pulsed High Duty Cycle Operation of $\lambda \sim$ 8 μ m Quantum Cascade Lasers, *Conference on Lasers and Electro-Optics (CLEO), Baltimore, MD*, May 8-10, 2007
7. **Zhijun Liu**, Daniel Wasserman, Scott S Howard, Anthony J Hoffman, Claire F Gmachl, Xiaojun Wang, Tawee Tanbun-Ek, Liwei Cheng, and Fow-Sen Choa, High Performance Quantum Cascade Lasers Grown by MOCVD with/without Lateral Regrowth, *28th International Conference on the Physics of Semiconductors (ICPS)*, Vienna, Austria, July 24-28, 2006
8. Oana Malis, Deborah L. Sivco, Jianxin Chen, Liming Zhang, A. Michael Sergent, **Zhijun Liu**, and Claire F. Gmachl, Optimization of InP-based waveguides for high-

performance mid-infrared quantum cascade lasers, *28th International Conference on the Physics of Semiconductors (ICPS)*, Vienna, Austria, July 24-28, 2006

9. **Zhijun Liu**, Daniel Wasserman, Scott S. Howard, Claire F. Gmachl, Xiaojun Wang, Tawee Tanbun-Ek, Liwei Cheng, and Fow-Sen Choa, MOCVD-grown Room Temperature Continuous-wave Quantum Cascade Lasers without Lateral Regrowth, *Conference on Lasers and Electro-Optics (CLEO)*, Long Beach, CA, May 21-27, 2006
10. Oana Malis, Deborah. L. Sivco, Jianxin Chen, Liming Zhang, A. Michael Sergent, **Zhijun Liu** and Claire F. Gmachl, Materials Design and Integration for Quantum Cascade Lasers, *Indium Phosphide & Related Materials (IPRM)*, Princeton University, May 7-11, 2006
11. **Zhijun Liu**, Daniel L. Recht, Scott S. Howard, Craig B. Arnold, and Claire F. Gmachl, Quantum cascade lasers tuned by amorphous As₂S₃ claddings, *The First Conference on Advances in Optical Materials (AIOM)*, Tucson, Arizona, USA, Oct. 12-15, 2005
12. Jian Z. Chen, **Zhijun Liu**, Claire F. Gmachl, and Deborah L. Sivco, Silver halide fiber-based evanescent-wave liquid droplet sensing with thermoelectrically cooled room temperature mid-infrared quantum cascade lasers, *Proceedings of SPIE*, Vol. 6010, p. 62-69, Infrared to Terahertz Technologies for Health and the Environment; Alexey A. Belyanin, Rebekah A. Drezek, Claire F. Gmachl; Eds., Nov 2005
13. Daniel L. Recht, **Zhijun Liu**, Khandaker R. Rahman, Claire F. Gmachl, and Craig B. Arnold, Quantum Cascade Lasers Tuned by Amorphous As₂S₃ Claddings, *Photon Processing in Microelectronics and Photonics IV*, eds. J. Fieret, P. R. Herman, T. Okada, and C. B. Arnold, *Proceedings of SPIE* Vol. 5713, 293- 299, 2005

14. Jian Z. Chen, **Zhijun Liu**, Daniel Wasserman, Claire F. Gmachl, Deborah L. Sivco, and Alfred Y. Cho, Approaches to compact quantum cascade laser modules with integrated coolers, *Conference on Lasers and Electro-Optics (CLEO)*, Baltimore, MD, USA, May 22-27, 2005